NOVEL CHEMICALLY SELECTIVE RAPID MAGNETIC RESONANCE IMAGING

TECHNIQUES AND THE CLINICAL APPLICATIONS

APPROVED BY SUPERVISORY COMMITTEE

Roderick McColl, PhD
_____

Peter Antich, PhD
_____

Richard Briggs, PhD
_____

Hanli Liu, PhD
_____

Paul Weatherall, MD
_____

_____

ACKNOWLEDGEMENTS

NOVEL CHEMICALLY SELECTIVE RAPID MAGNETIC RESONANCE IMAGING

TECHNIQUES AND THE CLINICAL APPLICATIONS

by

QI PENG

DISSERTATION

Presented to the Faculty of the Graduate School of Biomedical Sciences

The University of Texas Southwestern Medical Center at Dallas

In Partial Fulfillment of the Requirements

For the Degree of

DOCTOR OF PHILOSOPHY

The University of Texas Southwestern Medical Center at Dallas

Dallas, Texas

September, 2005

iv

NOVEL CHEMICALLY SELECTIVE RAPID MAGNETIC RESONANCE IMAGING

TECHNIQUES AND THE CLINICAL APPLICATIONS

Publication No. _____

Qi Peng, PhD

The University of Texas Southwestern Medical Center at Dallas, 2005

Supervising Professor: Roderick McColl, PhD

Magnetic Resonance Imaging (MRI) has become as powerful, non-invasive imaging modality for both diagnostic and research purposes. Nevertheless, the efficacy and efficiency of MRI can still be improved by the development of novel imaging methods (pulse sequences), as well as by exploring the everyday clinical and research applications of these new methods. This dissertation focuses on two novel chemically selective imaging methods for the generation of high quality fat-only or water-only images in short scan durations.

High quality fat imaging is mainly used for human fat distribution measurements. The study of fat distribution is important for both clinical diagnosis and basic research. The abnormal distribution of fat can be a predictor of many diseases such as type 2 diabetes. A rapid fat imaging technique based on water saturated balanced steady-state free precession (WS b-SSFP) pulse sequences is proposed and theoretically and experimentally compared with traditional methods such as a water-suppressed T1-weighted turbo spin-echo (TSE) sequence. WS b-SSFP is shown to offer significantly improved image quality (higher signal-to-noise ratio, contrast-to-noise ratio, fewer artifacts and less blurring/distortion) in reduced

scan duration. The high contrast between fat and water enables the use of a novel fat quantification method based on the image histogram, which includes the contribution of both full- and partial-volume fat pixels for fast and accurate fat quantification.

Rapid fat suppression is critical in many applications of clinical MRI. Traditional fat suppression methods are generally time-consuming and/or not effective in generating high quality images, particularly in fast short-TR sequences. A novel rapid fat suppression strategy is introduced, which employs both a strong fat presaturation and a sustained water excitation in a short TR, turbo field echo (TFE) sequence with long echo train length. The sequence is validated to offer comparable fat suppression in much shorter scan duration than traditional presaturation-only fast field echo (FFE), or water-excitation only FFE approaches.

TABLE OF CONTENTS

PRIOR PUBLICATIONS

Q. Peng, R. McColl, J. Wang, P. Weatherall, "Novel Rapid Fat Suppression Strategy with Spectrally Selective Pulses", Magn Reson Med. 2005 (in press).

Q. Peng, R. McColl, J. Wang, J. Chia, P. Weatherall, "Water-Saturated 3D Balanced Steady-State Free Precession for Fast Abdominal Fat Quantification", J Magn Reson Imaging. 2005; 21(3):263-71.

J. Wang, K. Compton, and **Q. Peng**, "Proposal of a quality-index or metric for soft copy display systems: contrast sensitivity study". J Digit Imaging, 2003. 16(2): p. 185-202.

J. Wang, **Q. Peng**, "An Interactive Method of Assessing the Characteristics of Softcopy Display Using Observer Performance Tests", J Digit Imaging, 15 suppl 1: 216-8, 2002

LIST OF FIGURES

xv

LIST OF TABLES

LIST OF ABBREVIATIONS

2D – Two-Dimensional

3D – Three-Dimensional

AP – Anterior-Posterior

B-SSFP – Balanced Steady-State Free Precession

BMI – Body Mass Index

CNR – Contrast-to-Noise Ratio

CT – Computed Tomography

ETL – Echo Train Length

DIR – Double Inversion Recovery

FFE – Fast Field Echo

FID – Free Induction Decay

FOV – Field of View

IAF – Intra-abdominal Fat

IR – Inversion Recovery

MRI – Magnetic Resonance Imaging

NMR – Nuclear Magnetic Resonance

PPM – Parts per Million

REPP – Research Prepulse

RF – Radio-frequency

rFOV – Rectangular Field of View

LR – Left-Right

ROI – Region of Interest

SAF – Subcutaneous Abdominal Fat

SAR – Specific Absorption Rate

SENSE – Sensitivity Encoding

SNR – Signal-to-Noise Ratio

SPIR – Spectral Partial Inversion Recovery

T1W – T1-Weighted

T2W – T2-Weighted

TAF – Total Abdominal Fat

TSE – Turbo Spin Echo

TFE – Turbo Field Echo

WS – Water-Suppressed, or Water Saturated

Chapter 1 Overview

1.1 Introduction

With the development of both advanced hardware and imaging techniques (pulse sequences) of modern MR scanners, MRI is playing an increasingly important role for both diagnostic and research purposes. Research to improve the effectiveness of MRI mainly includes efforts to improve image quality (high SNR and CNR, reduced artifacts and distortion) and to minimize scan duration. My dissertation will focus on rapid techniques for chemically selective MR imaging to obtain either fat-only or water-only images. Correspondingly, two novel rapid imaging techniques will be discussed in detail. The first is a rapid fat-only imaging technique, which employs water-saturated balanced steady-state free precession. The second is a rapid fat suppression strategy and its pulse sequence implementation. Both phantom and human experiments will be performed to investigate image quality and acquisition duration (or scan efficiency) of these novel rapid chemically selective imaging techniques compared with currently available methods.

1.2 Outline

Some basic MR physics, imaging principles, and traditional chemically selective imaging methods are briefly discussed in Chapter 2. The main contribution of this dissertation is divided into three parts. First, a rapid MR fat imaging technique is proposed and validated in phantom and human studies, which is covered from Chapter 3 to Chapter 4. Second, a rapid automated abdominal fat distribution model and fat quantification method is discussed in Chapter 5. Third, a novel rapid fat suppression imaging strategy is proposed, and compared with other methods. This is discussed in Chapter 6 and Chapter 7.

This dissertation is organized as follows:

Chapter 2: Introduction

Some of the basic concepts of MRI physics, including magnetization, RF excitation, relaxation, and image formation are explained. To provide a foundation for the following chapters, a brief discussion of traditional chemically selective imaging methods and principles is also presented.

Chapter 3: Rapid Body Fat Imaging: Pulse Sequence

The clinical challenges of body fat imaging using MRI are outlined, with an overview of some traditional MRI sequences for fat imaging. Water saturated balance steady-state free precession (WS b-SSFP) is introduced as a new fat imaging method. Signal levels for fat and contrast between fat and some other lean-tissues (such as muscle) are compared theoretically. An optimized pulse sequence on a clinical scanner is also explained and tested on human.

Chapter 4: Abdominal Fat Imaging: Method Validation

A novel fat imaging method is employed and quantitatively compared with traditional methods for abdominal fat imaging. In phantom studies, WS b-SSFP offers comparable oil volume measurement accuracy with CT, and significantly more accurate estimation compared with traditional T1W TSE sequences. In human studies, SNR/CNR of WS b-SSFP is first compared with T1W TSE, WS T1W TSE. To validate the fat quantification accuracy of WS b-SSFP in humans, fat volume measurements using both WS b-SSFP and WS T1W TSE are performed and compared. Finally, feasibility of free-breath abdominal fat imaging using WS b-SSFP is also investigated.

Chapter 5: Abdominal Fat Quantification

A simple and robust fat distribution model is introduced in this chapter. Both full- and partial-volume fat pixels from the acquired image are considered in the fat quantification method. The accuracy of this model is validated in a phantom study, and the improvement on fat quantification for human abdomen images is also demonstrated using a traditional method as a reference.

Chapter 6: Rapid Fat Suppressed Imaging

The need for time-efficient fat suppressed MR imaging in clinical applications is briefly discussed. A framework of fat suppression strategies is established, and a novel rapid fat suppression strategy is proposed in short TR pulse sequences. A pulse sequence implementation of this fat suppression concept is tested, and compared with traditional fat suppression methods in both phantom and human studies.

Chapter 7: Rapid Fat Suppression Applications

In this chapter, the impact on clinical MR imaging of the novel fat suppression strategy is demonstrated in breast imaging and musculoskeletal imaging. For breast imaging, fat suppressed bilateral breast imaging is tested and the possibilities of enhancing imaging speed are also explored. Articular cartilage imaging using the novel fat suppression technique is also presented to demonstrate fast T_1-weighted and T_2-weighted imaging in musculoskeletal imaging applications.

Chapter 8: Summary and Future Directions

The work presented in the previous chapters is summarized with recommendations for future directions in each area.

Chapter 2 Introduction

The phenomenon of nuclear magnetic resonance (NMR) was first observed independently by Felix Bloch and Edward Purcell in 1946. Developments in NMR led to widespread application of NMR spectroscopy. In 1973, Paul Lauterbur used gradient magnetic fields to form the first magnetic resonance images (1). Since then, the field of magnetic resonance imaging (MRI) has developed significantly. This chapter gives an overall understanding of basic MR physics and MR imaging principles. The concept of chemically selective MRI and current available techniques are also briefly discussed.

2.1 MR Physics

2.1.1 Production of Net Magnetization

Atomic nuclei with an odd number of protons have an intrinsic characteristic known as spin-angular momentum. The hydrogen atom (^{1}H, or proton) is the target nucleus of most clinical MRI scans because the two major components of the human body are water and fat, both of which contain hydrogen. Normally, the nuclear "spins" of protons are randomly aligned, and there is no net magnetization. When the protons are placed in an external magnetic field B_0, the individual protons begin to rotate perpendicular to, or precess about, the magnetic field. The protons might be tilted slightly away from B_0, but the axis of rotation is parallel to B_0. This precession is at a constant rate and occurs because of the interaction of the magnetic field with the spinning positive charge of the nucleus. The rate or frequency of precession is proportional to the strength of the magnetic field and is expressed as the Larmor equation:

$$\omega_0 = \gamma B_0 \tag{2.1}$$

where ω_0 is the Larmor frequency in megahertz (MHz), B_0 is the magnetic field strength in Tesla that the proton experiences, and γ is a constant for each nucleus in $s^{-1}T^{-1}$, known as the *gyromagnetic ratio*.
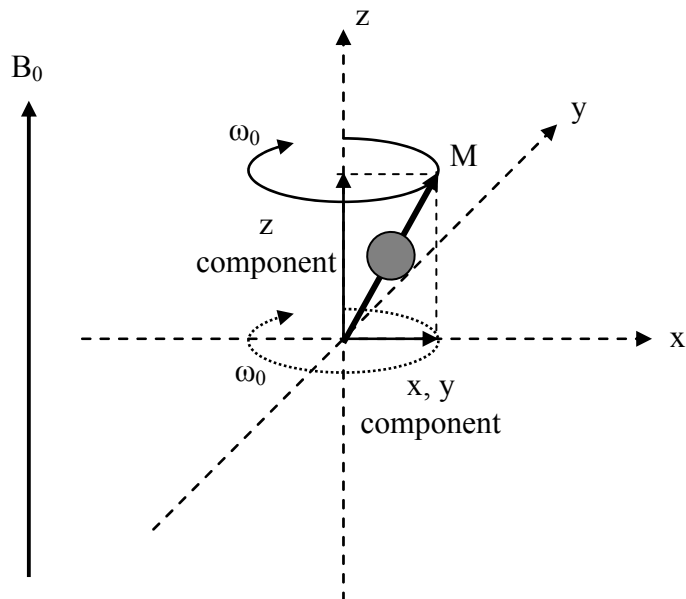
Figure 2.1 Proton precssion inside an external magnetic field. The spin vector of the individual spin is shown as M, and the precessional axis is parallel to B_0. The z component of the spin vector has a constant magnitude and direction and is therefore the component of interest. The x and y components vary with time at Larmor frequency ω_0, generating zero net magnetization.

Proton precession of an individual proton in a magnetic field B_0 is shown in Figure 2.1. It has also been found that, since protons aligned along B_0 have lower energy compared with those against B_0, more protons precess along B_0 direction according to Boltzmann distribution, compared with those which precess opposite to B_0 direction. Therefore, a vector addition of the magnetization of all spins will generate a net component along B_0 direction as shown in Figure 2.2. The net magnetization is the basis of the signal in NMR or MRI.
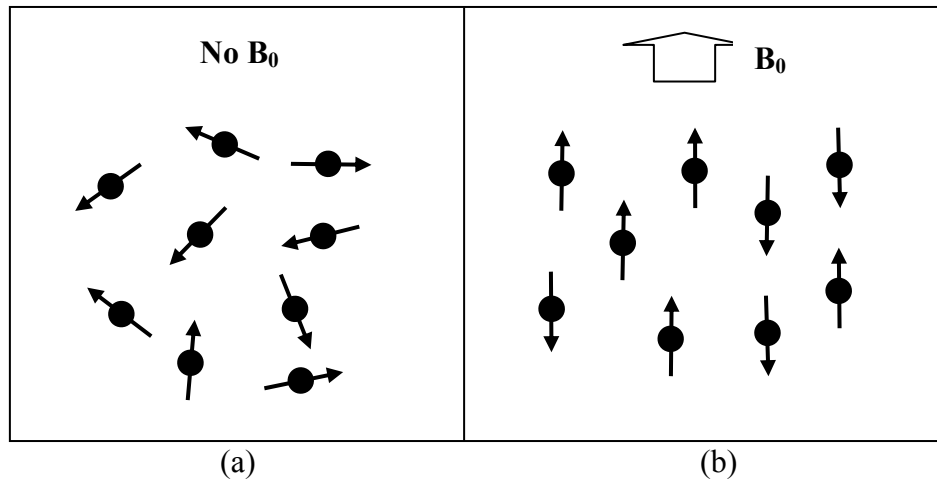
Figure 2.2 The generation of net magnetization in a magnetic field. Without an external magnetic field, nuclear spins in material are randomly oriented, leading to no net magnetization (a). If an external magnetic field (B_0) is applied, slightly more spins are aligned along B_0 compared with those opposite to B_0. The excess spins along B_0 result in an overall net magnetization which makes NMR and MRI possible.

For convenience, the direction of B_0 is defined as the longitudinal, or z-direction. The plane that is perpendicular to B_0 is defined as the transverse plane (x-y plane).

2.1.2 Excitation

Although a net magnetization M can be created by B_0, the transverse component of M is zero at thermal equilibrium because the precessing magnetic moments have random phases in the transverse plane. To obtain a collective signal, phase coherence of spin vectors in the transverse plane has to be generated. This is achieved by applying another external field B_1 to excite the net magnetization to the transverse plane.

B_1 is applied perpendicular to B_0 for a short duration. It is also called an RF pulse because it falls into the radio-frequency (RF) range. An RF pulse can disturb the thermal equilibrium of the longitudinal magnetization generated by B_0, and can establish spin phase coherence in the transverse plane to generate a signal that can be measured by an RF coil. The generation of transverse spin coherence by an α angle excitation is illustrated in Figure 2.3.
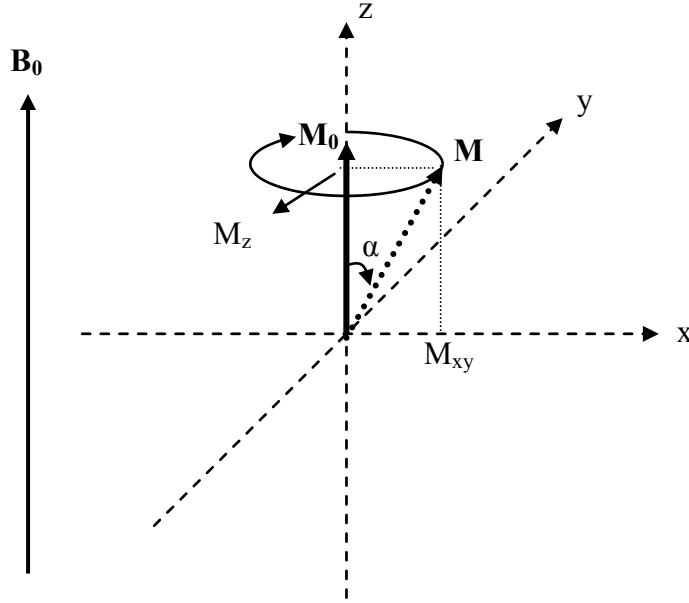
Figure 2.3 Magnetization evolution induced by an RF excitation. The magnetization (**M₀**) is first along z direction and will be tipped to **M** with an α RF pulse. It hence has a longitudinal component (M$_z$) and a transverse plane component (M$_{xy}$). It is the transverse plane component that can generate detectable signal for MRI.

2.1.3 Relaxation

After magnetization is disturbed from the thermal equilibrium by an RF excitation, it will return to the equilibrium state after a sufficient time once the perturbation is withdrawn. This process is known as *free induction decay (FID)* or *relaxation*. The recovery of the longitudinal component, M$_z$, is called *longitudinal relaxation*, whereas the decay of the transverse magnetization, M$_{xy}$, is called *transverse relaxation*.

The longitudinal relaxation process is governed by the equation

$$\frac{dM_z}{dt} = \frac{M_z - M_o}{T_1} \tag{2.2}$$

where T_1 is called the spin-lattice time constant and characterizes the return of the magnetization to equilibrium along the direction of the B_0 direction. The solution of the equation is

$$M_z = M_0 + (M_z(0) - M_0)e^{-t/T_1} \tag{2.3}$$

If the equilibrium is disturbed by a 90° excitation, $M_z(0) = 0$, the above equation can be simplified to

$$M_z = M_0(1 - e^{-t/T_1}) \tag{2.4}$$

which is shown in Figure 2.4(a).

Similarly, the transverse component of the magnetization behaves according to

$$\frac{dM_{xy}}{dt} = -\frac{M_{xy}}{T_2} \tag{2.5}$$

where T_2 is called the spin-spin time constant and characterizes the loss of signal in the transverse plane due to molecular interactions and magnetic field inhomogeneities. If a 90° RF excitation is applied at equilibrium, $M_{xy}(0)$ equals M_0. Therefore, the above equation becomes

$$M_{xy} = M_0 e^{-t/T_2} \tag{2.6}$$

The M_{xy} signal dependence on time is shown in Figure 2.4(b).

(a) (b)
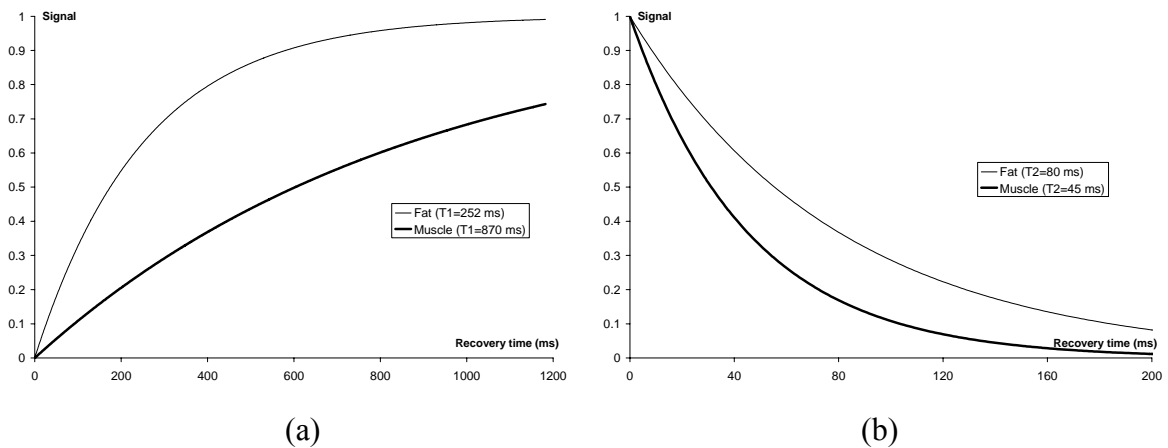
Figure 2.4 Longitudinal relaxation and transverse relaxation of magnetization. (a) The longitudinal component of magnetization decays exponentially toward its thermal equilibrium (1.0) with a time constant T_1. (b) The transverse component of magnetization

decays exponentially toward zero with a time constant T_2. Both fat and muscle signal is simulated.

2.1.4 The Bloch Equation

To account for both the T_1 and T_2 relaxations, the Bloch equation describes the magnetization process as follows (2):

$$\frac{dM}{dt} = (M \times \gamma B) + \frac{M_0 - M_z}{T_1} - \frac{M_{xy}}{T_2} \tag{2.7}$$

where M is the time variant magnetization vector, and B is the magnetic field felt by the protons. In the Bloch equation, the cross product term describes the precessional behavior, while the relaxation terms describe the exponential behaviors of the longitudinal and transverse magnetization components.

2.2 Image Formation

2.2.1 Spatial encoding

In clinical MRI, spatial encoding is realized through the application of magnetic field gradients. Therefore, proton resonant frequency can be spatially dependent. A linear magnetic field gradient generates a linear perturbation to B_0, so that the exact magnetic field can be represented as:

$$B_i = B_0 + G \times r_i \tag{2.8}$$

Where B_i is the magnetic field at location r_i and G is the gradient amplitude (T/m). According to Larmor equation given in Equation 2.1:

$$\omega_i = \gamma(B_0 + G \times r_i) \tag{2.9}$$

where ω_i is the frequency of the proton at position r_i. Magnetic field gradients can be applied along one of the x, y, and z directions, or an arbitrary combination of them. Therefore, spatial encoding along an arbitrary direction can be achieved by using corresponding magnetic field gradients.

Spatially selective excitation can be achieved by employing a bandwidth-limited RF pulse combined with a linear gradient field as shown in Figure 2.5. The slice selection direction is resonant frequency-encoded by the linear gradient. Ideally, a sinc-shaped RF pulse will generate a rectangular shape frequency profile corresponding to the frequency range of the slice to be excited. The position of the excited slice can be adjusted by the RF central frequency, and the thickness of the slice is determined by the RF bandwidth.
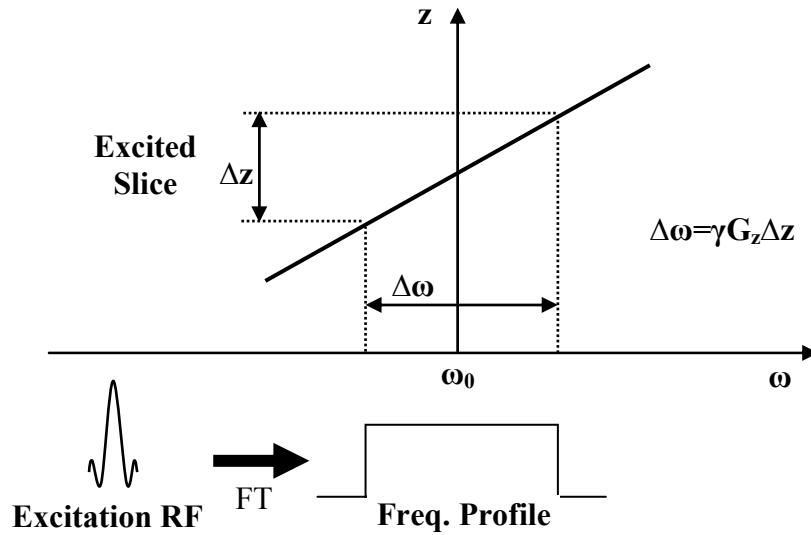
Figure 2.5 Slice selective excitation. This is accomplished by using a sinc-shaped RF pulse in combination with a linear magnetic field gradient along the slice direction. The central frequency (ω_0), and the bandwidth ($\Delta\omega$) of the excitation RF determine the location, and the thickness of the excited slice, respectively.

However, slice selective excitation only reduced one degree of freedom in a three-dimensional (3D) object. Within the selected slice all the spins have the same resonant frequency, and it is impossible to differentiate spins at different locations. To generate a two-dimensional (2D) image of the excited slice, in-plane spatial encoding has to be performed. This is achieved through frequency encoding and phase encoding. The frequency and phase encoding directions are usually referred to as x-, and y-direction, respectively. Similar to the selective excitation, magnetic field gradients G_x and G_y can be applied to produce spatial

variation of the spins. In the frequency encoding direction (x), the spatial position of a spin is encoded by the frequency of the spin. For example, with the presence of a linear magnetic field gradient along x direction, the frequencies of spins at different locations become

$$\omega(x) = \omega_0 + \gamma G_x x \tag{2.9}$$

Therefore, position along the frequency-encoding axis can be resolved using the precessional frequency dependence on the spatial position. Spatial location along the phase encoding direction can be encoded by phase variations. This is done by employing the fact that a spin at position y can accumulate a phase shift that is equal to the time integral of the precessional frequency

$$\phi(y) = \gamma y \int_0^t G(s)ds \tag{2.10}$$

By applying a gradient pulse, G_y, for a specific duration τ_y, spatial position along the y-axis can be differentiated. However, multiple steps of phase encodings have to be performed to achieve spatial differentiation along the phase encoding direction. Each time, the value of $\phi(y)$ is changed to achieve a different phase encoding strength. Accounting for both the frequency and phase-encoding gradients, the transverse magnetization becomes $M_{xy}exp(-i\omega_0 t)exp(-i\gamma G_x xt)exp(-i\gamma G_y y\tau_y)$ for a particular phase encoding gradient G_y.

2.2.2 Image Reconstruction

As shown earlier, the spatial-encoded FID signal that is sensed by the receiver coil will be

$$s_r(t) = \int_x \int_y M_{xy} e^{-i\omega_0 t} e^{-i\gamma G_x xt} e^{-i\gamma G_y y\tau_y} dxdy \tag{2.11}$$

where τ_y is the duration that the G_y is turned on. After demodulation, the baseband signal $s(t)$ can be extracted by ignoring the high-frequency (ω_0) component:

$$s(t) = \int_x \int_y M_{xy} e^{-i\gamma G_x xt} e^{-i\gamma G_y y\tau_y} dxdy \tag{2.12}$$

Two new terms, $k_x(t)$ and $k_y(t)$ can be defined as the time integrals of the $G_x(t)$ and $G_y(t)$

$$k_x(t) = \frac{\gamma}{2\pi} \int_0^t G_x(s)ds \qquad (2.13)$$

$$k_y(t) = \frac{\gamma}{2\pi} \int_0^t G_y(s)ds \qquad (2.14)$$

Here, k_x and k_y form a spatial frequency coordinate space, and each point in that space corresponds to the frequency- and phase-encoding intensities for each data acquisition time point. This space is usually referred to as k-space in MRI. For 2D Cartesian readouts, $G_x(t)$ and $G_y(t)$ can be regarded constant during turned out duration for each readout. Therefore, Equation 2.12 becomes:

$$s(t) = \int_x \int_y M_{xy} e^{-i2\pi k_x x} e^{-i2\pi k_y y} dxdy \qquad (2.15)$$
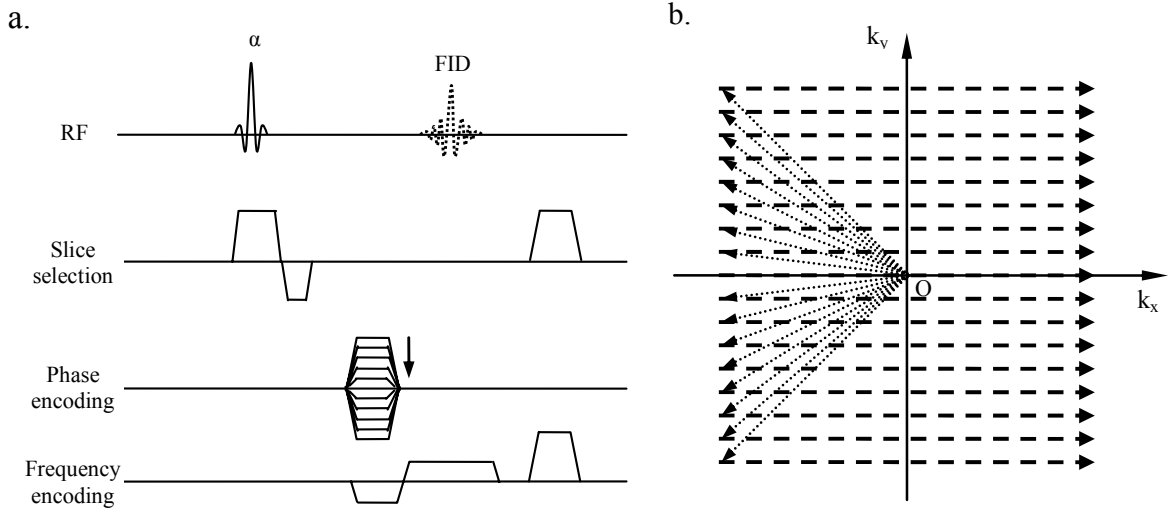
Figure 2.6 Diagram of a pulse sequence and the k-space representation. To acquire a two-dimensional image, different phase encodings have to be performed as shown by the multiple gradients along phase-encoding direction in (a). In (b), each horizontal arrow line stands for an FID data readout as shown in (a), and the number of lines is the number of phase encodings. The negative lobe at the beginning of the frequency encoding gradients, and the different phase encoding gradients are used to initialize the spatial encoding from the center of k-space (point O) to the beginning of each k-space readout line. The initiation is indicated by the dotted arrow starting from point O.

Therefore, the spin distribution, $M(x, y)$ can be easily calculated after performing an inverse Fourier transform on $s(t)$. A 2D gradient echo pulse sequence and the corresponding k-space interpretation of data acquisition are shown in Figure 2.6.

2.3 Chemical Shift

The Larmor frequency of a proton is proportional to the effective magnetic field it feels. Therefore, it is dependent on the applied external magnetic field B_0, and is also influenced by the micro-environment such as the molecular structure of the proton due to the electron shielding effect. For MRI, the bulk of the hydrogen MR signal arises from water and fat. Water has two hydrogen atoms bonded to one oxygen atom, whereas fat has many hydrogen atoms bonded to a long-chain carbon framework. Due to the different molecular environment, a fat proton experiences a difference local magnetic field than a water proton, even when the applied external magnetic field is the same. This effect is known as *chemical shielding*, and it is proportional to the main magnetic field B_0:

$$B_i = B_0(1 - \sigma_i) \tag{2.16}$$

where σ_i is the shielding term for either water or fat proton. Since σ_i is typically small ($\sim 10^{-4} - 10^{-6}$), the resonant frequency difference of water and fat protons is small. A convenient scale to express frequency differences is the ppm scale, defined as follows:

$$\omega_{i(ppm)} = (\omega_{i(Hz)} - \omega_{ref})/\omega_{ref} \tag{2.17}$$

Frequency differences expressed in this form are known as chemical shifts. The major advantage of the ppm scale is that frequency differences are independent of B_0. For fat and water, the difference in chemical shift at all field strengths is approximately 3.5 ppm, with fat at lower frequency. Therefore, the resonant frequency difference is about 220 Hz at 1.5 T, and about 440 Hz at 3.0 T.

The resonant frequency difference of water and fat protons can generate chemical shift artifacts, which is a mis-registration of fat and water protons from a same physical voxel that are mapped to different voxels in an image. Another possible artifact is the phase cancellation artifact often observed in out-of-phase gradient echo images, where signal of water and fat protons from the same voxel add destructively. On the other hand, the resonant frequency difference between water and fat can also be used for chemically selective imaging using spectrally selective imaging techniques, as will be demonstrated later in this chapter.
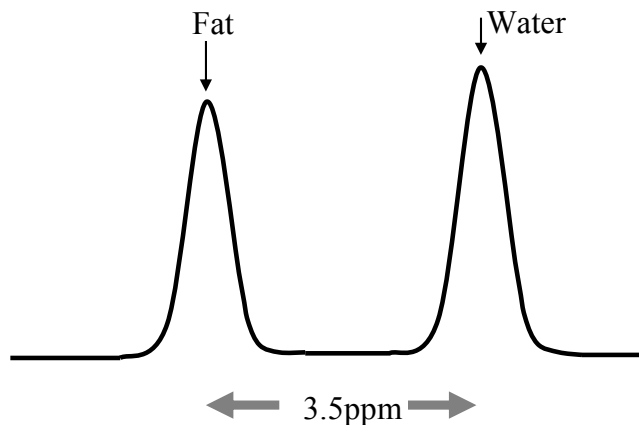
Figure 2.7 Chemical shift between water and fat. The resonant frequency difference is induced by the chemical shielding effect. The resonant frequency of fat protons is 3.5 ppm lower compared with that of water, which corresponds about 220Hz for a 1.5 T scanner.

2.4 Chemically Selective MRI

2.4.1 Introduction

By default, MR signal from both water and fat protons will be acquired by the receive coil or coils. However, sometimes it is advantageous to generate fat- or water-only images to reduce chemical shift-induced artifacts and to improve visibility.

Water-saturated fat imaging is mostly used for body fat distribution imaging to study how human body fat distribution influences, or is influenced by human health. Although fat signal is usually bright in MR images, water-saturated images will improve the contrast between fat and water, leading to easier fat volume measurement during post-processing. It is also much easier to employ automated or semi-automated computer programs to achieve fast and accurate fat quantification.

Fat suppressed water imaging is also of great clinical significance to improve diagnostic accuracy. Generally, body fat is not directly involved in pathology on lean-tissue. Since fat has a relatively short longitudinal relaxation time and a long transverse relaxation time, as well as a high proton density, fat signal is usually bright on images obtained using

non-chemically selective MR sequences. Therefore, fat signal may reduce the conspicuity of disease in three ways. First, the structural and/or functional information on the pathology is difficult to detect in a strong fat signal background, if fat signal is not suppressed. Second, the morphological structure of the lean tissue may be influenced by the chemical shift artifact. Third, as fat signal is usually much brighter compared with lean tissue, it occupies the dynamic range, preventing subtle signal variation in lean tissue from being detectable. This is particularly problematic in contrast enhanced dynamic studies.

There are several approaches to achieve chemically selective imaging. Generally, they take advantage of two differences of fat and water protons. The first difference is the T_1 relaxation difference, and the second is the resonant frequency difference. Four popular chemically selective techniques will be briefly discussed in the following sections.

2.4.2 Inversion Recovery Technique

Inversion-recovery (IR) imaging is a traditional method for chemically selective imaging, which employs the longitudinal relaxation time (T_1) differences between fat and non-fat tissue (3,4). Therefore, it is independent of magnetic field inhomogeneities. In this method, a 180° inversion preparation pulse inverts the longitudinal magnetization for both fat and water spins from thermal equilibrium. Fat has a shorter T_1 relative to most non-fat tissue, and recovers faster to equilibrium as shown in Figure 2.8. An optimal time of inversion (TI) can be chosen before fat suppressed data acquisition since fat signal crosses zero earlier than non-fat.

However, this method is fundamentally limited because it requires a long delay time to allow longitudinal magnetization recovery, and it needs a long TR to allow all tissues to return to the equilibrium before the next inversion pulse. It is also inefficient because the data acquisition is done only at the signal zero-crossings, wasting a considerable amount of time which could otherwise be used for data acquisition. The signal of unsuppressed tissues is also reduced since the longitudinal magnetization is not fully recovered before data acquisition. Another drawback of this technique is that it is not specific. Tissue with a short T_1 and tissue

with a long T_1 may produce similar signal intensities although their longitudinal magnetization has opposite direction (positive or negative). In addition, tissue with a T_1 close to that of fat will also be suppressed.
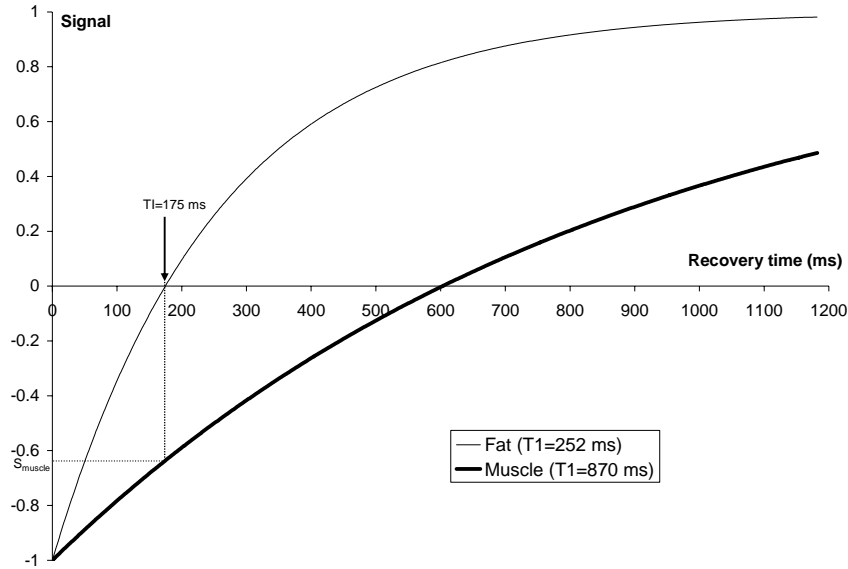
Figure 2.8 Inversion recovery for chemically selective imaging. The technique employs the longitudinal relaxation time (T_1) difference of fat and non-fat tissue. The simulation shows fat and muscle signal behavior after the administration of a 180° RF from the magnetization equilibrium. For fat T_1 = 252 ms, an optimal TI is about 175 ms to generate fat-saturated signal. To generate a fat-only image, TI = 600 ms has to be used to suppress muscle signal.

2.4.3 Dixon's Method

Dixon's method is based on the resonant frequency differences between water and fat protons (5). Due to chemical shift, fat resonant frequency is 220 Hz lower compared with that of water at 1.5 T. The resonant frequency difference can be decoded from the phase images of an adequate MR scan. In a gradient echo imaging sequence, water and fat spins will generally have the same transverse magnetization phases if TE equals to even multiples of 2.3 ms (2.3 ms is the time for water and fat spins to de-phase 180°), and will have 180° phase difference if TE is odd multiples of 2.3 ms. The phase evolution of water and fat spins with TE in a gradient echo is demonstrated in Figure 2.9. If a pair of images with water and

fat magnetizations aligned in-phase and out-of-phase (opposed-phase) is acquired, addition or subtraction of these images will result in either water or fat images as shown in Figure 2.10. This method is first proposed by Dixon, and is often referred to as the 2-point Dixon's method (2PD).
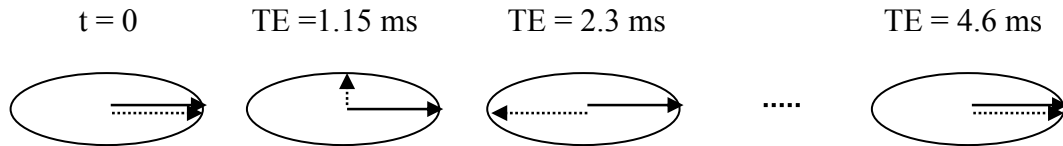
Figure 2.9 Generation of in- and out-of- phase images. It demonstrates the relative phase evolution between water and fat with increasing TE in a gradient echo sequence. The phases are represented by solid (water) and dotted (fat) arrows, assuming scanner synthesizer frequency is set to water resonant frequency.

Water Image   Fat Image
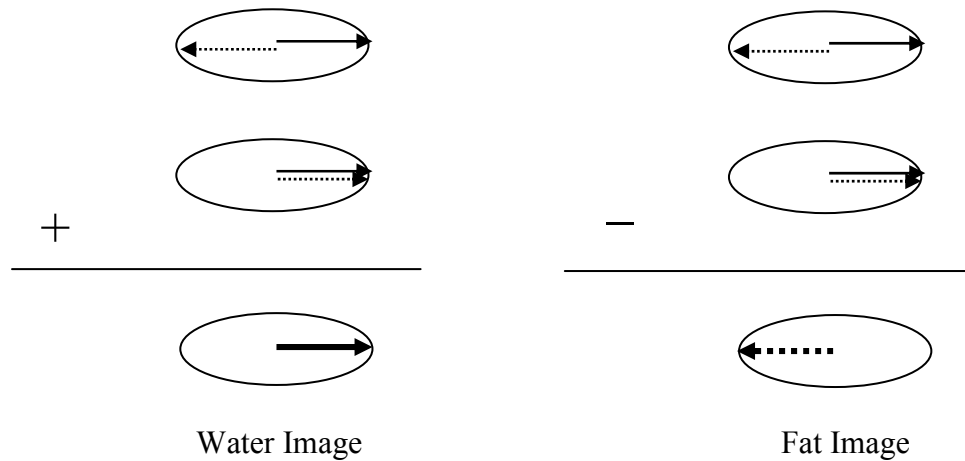
Figure 2.10 Phase sensitive imaging to obtain chemically selective images. This method is known as 2-Point Dixon's method and it requires a pair of images with water and fat magnetization in- and out-of- phase. Adding two (complex) images would result in water image while subtracting would give fat image.

The drawback of this method is that it requires an extra scan, which doubles the scan duration. It is also sensitive to B_0 inhomogeneities. Three-point, and multiple-point Dixon's

method have also been proposed, and these methods are less sensitive to B_0 inhomogeneities (6,7). However, more scan duration is needed. The long scan duration, aggravated by the patient motion problem which is not uncommon for clinical imaging, limits its broader applications.

2.4.4 Spectrally Selective Presaturation

Spectrally selective presaturation is a widely used technique for chemically selective imaging (8,9). As in Dixon's method, this method also takes advantage of the difference in the Larmor frequencies of fat and water. If the magnetic field is homogeneous enough, a narrow band RF pulse can be used to tip either species (fat or water) into the transverse plane without disturbing the magnetization of the other. This technique is usually only spectrally selective but not spatially selective. Therefore, it tips down all fat magnetization regardless of the location. Following this, spoiler gradients (crushers) are applied to destroy the transverse coherence, leading to zero signal in the data acquisition phase.

Practically, the flip angle of the presaturation RF is slightly higher than 90º to allow slight T_1 relaxation for the signal to cross zero at the following RF excitation. Therefore, it is called a spectral partial inversion recovery (SPIR) pulse on Philips scanners. Spectral presaturation is clinically attractive because it only modifies signal of one species, and is flexible to use in a variety of pulse sequences. However, because of T_1 relaxation, the suppressed signal recovers, thus only a limited time is available for high quality chemically selective imaging. This is particularly problematic for fat suppressed imaging as fat has a relatively short T_1. Frequent repeating of the presaturation phase is therefore mandatory to avoid degraded image quality. This consumes a significant amount of time and lengthens scan duration. Another major drawback of the spectral presaturation technique is that it is sensitive to B_0 inhomogeneity, as water and fat off-resonances might overlap in a nonuniform magnetic field, and can not be separated spectrally.
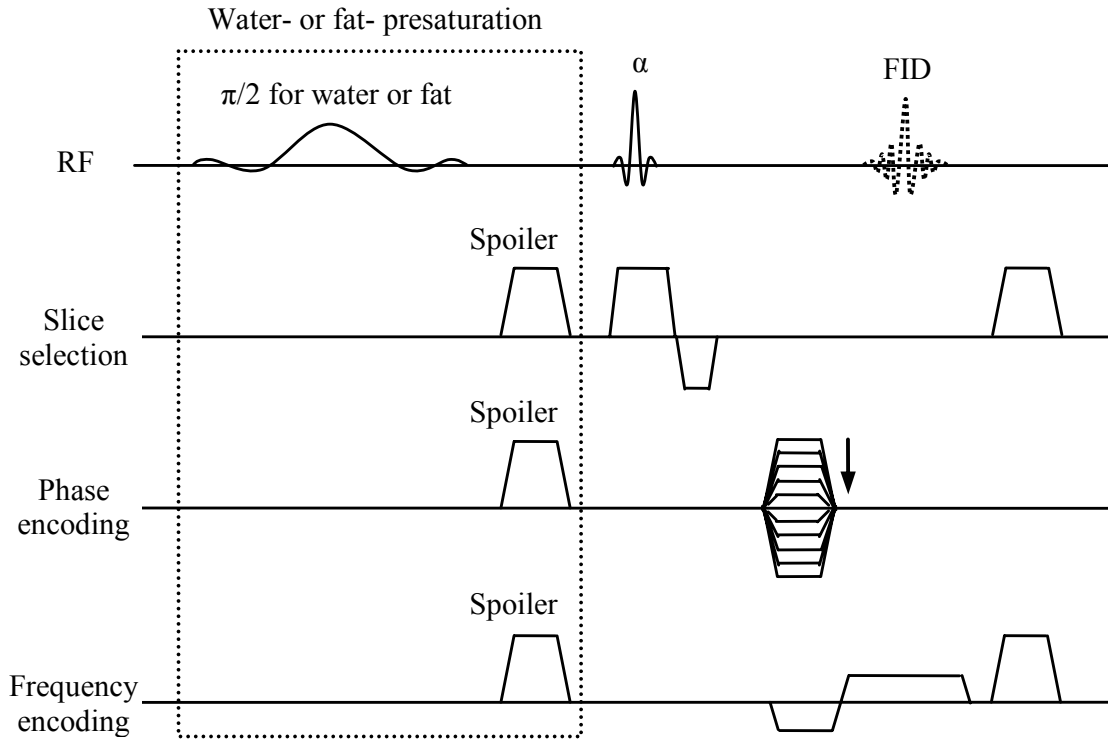
Figure 2.11 Pulse sequence of the spectrally selective presaturated imaging. Water- or fat-presaturation is achieved by applying a narrow band RF pulse with a flip angle of $\pi/2$, immediately followed by spoiler gradients to destroy magnetization coherence in the transverse plane. One or multiple gradient echo readouts can be followed for chemically selective data acquisition. The readout train length (shot duration) is limited due to longitudinal relaxation of the suppressed species.

2.4.5 Spatial-Spectral Excitation (SSE)

Spatial-spectral excitation (SSE, or SPSP excitation) employs an RF pulse train in conjunction with spatially selective magnetic field gradients to achieve simultaneous selection in space and resonant frequency. The concept was first introduced by Meyer et al based on the k-space interpretation of the small-tip excitation (10). A simplified SPSP pulse design was proposed by Schick in 1998, which employs binomial RF pulse train for spectrally selective excitation in combination with spatially selective magnetic field gradients (11). An example of a 3rd order binomial SSE pulse train designed for water selective

excitation is illustrated in Figure 2.12. The simulated transverse magnetization disturbed from thermal equilibrium by the SSE is shown in Figure 2.13.
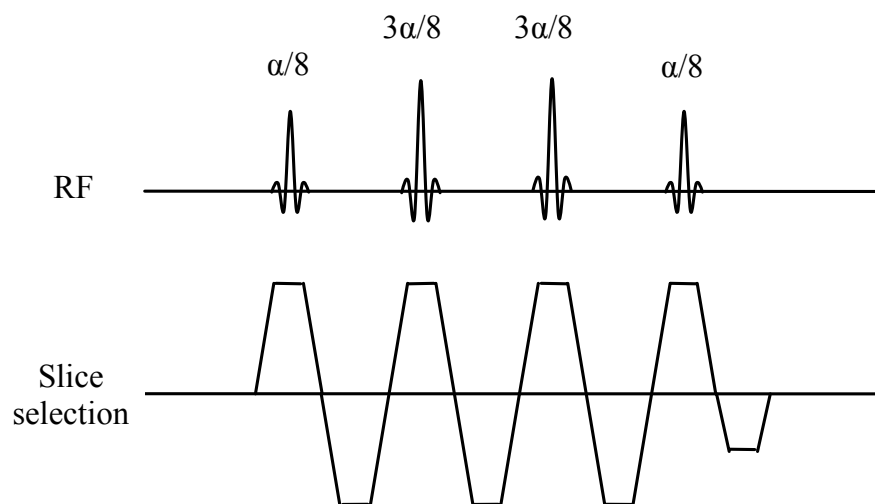
Figure 2.12 SSE pulse train. The figure shows the timing diagram of a 3rd order (1-3-3-1, 4 subpulses) spatial-spectral pulse train. The inter-pulse interval is 2.3 ms on a 1.5 T scanner. The flip angles for the RF pulses have a binomial distribution. The phases of the four pulses are (0°-0°-0°-0°) for water selective excitation, and (0°-180°-0°-180°) for fat selective excitation.

Chemically selective imaging using SSE is generally effective and fast. It also gains with higher magnetic fields as the difference of water and fat resonant frequencies increases. Furthermore, it is less sensitive to B_1 inhomogeneities compared with RF presaturation methods. However, SSE demands high gradient slew rates to drive the slice selection gradients fast enough to achieve the short RF inter-pulse interval. The existence of eddy currents might degrade the performance of SSE, and makes the implementation of these pulses difficult and complicated. In addition, high-order binomial SSE is usually mandatory to achieve good spectral selection, which increases both minimum achievable TR and TE. Therefore, it is very sensitive to motion-induced artifacts and T_2^* decay.
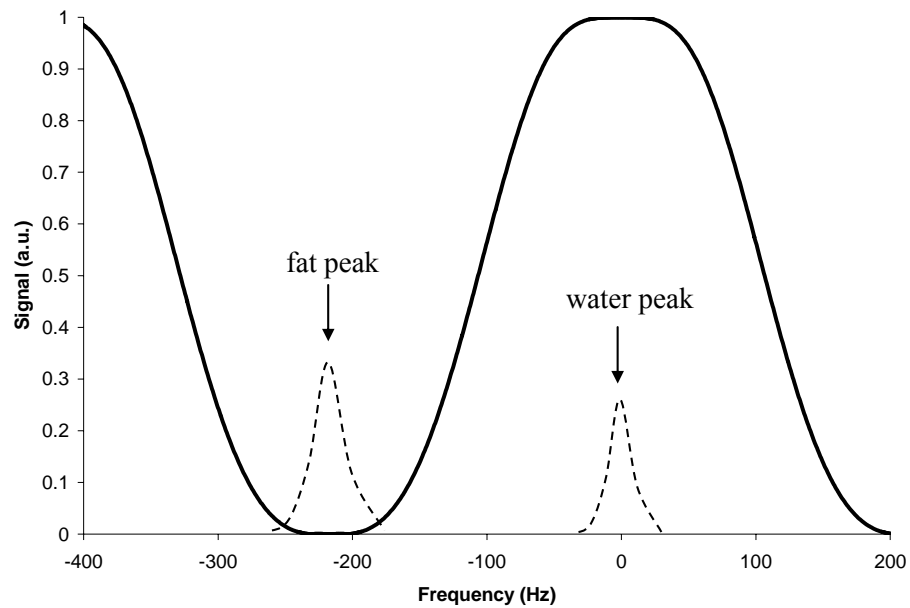
Figure 2.13 Spectral response of SSE. It demonstrates the simulated transverse magnetization magnitude after a 3rd order spatial-spectral, water selective excitation. The flip angles and phases of the four subpulses are (11.25°, 33.75°, 33.75°, 11.25°) and (0°, 0°, 0°, 0°), respectively. It is obvious that water spins are excited to transverse plane while fat signal is suppressed.

Chapter 3 Rapid Fat Imaging: Pulse Sequence

3.1 Introduction

The need for a rapid fat imaging technique using MRI stems from the demand for human body fat (or adipose tissue) distribution quantification in clinical and research environments. It is now established that the distribution of body fat has important effects on human health. The regional accumulation of intraabdominal fat (IAF) has been widely regarded to be highly correlated with the development of major western diseases, such as type II diabetes, cardiovascular disease, and cancer (12-15). Conversely, regional-selective loss of adipose tissue can also be a predictor of certain diseases such as diabetes and dyslipidemia. Clinically, an accurate measurement of adipose volumes over the whole body can also be a screening and monitoring method for healthy individuals and patients. Research-wise, further understanding of the correlation of obesity and a variety of diseases are still under intensive investigation. Unfortunately, a safe, reliable, and cost-effective imaging method is still needed.

Traditionally, human body composition, including obesity or body fat volume can be estimated by non-imaging methods such as anthropometric measurements (i.e. BMI), underwater-weighting, air-displacement plethysmography, and bioelectrical impedance and conductance measurements. Those methods suffer from the fact that no three dimensional adipose tissue distribution is obtained. Computed tomography (CT), and MRI are the two major imaging modalities that have been proposed for body fat distribution imaging and quantification. CT is not preferable for fat quantification in the clinical environment due to the associated radiation exposure. It is particularly not suitable for repeated studies on infants, children, and healthy subjects. Because multiple images can be obtained without any known health risks for the subjects, MRI is well suited for assessment of regional or whole-body fat distribution (16-19).

3.2 Traditional MR Fat Imaging Approaches

There are a variety of approaches to generate images adequate for fat quantification. Those approaches generally fall into two categories. The first category is to use non-chemically selective imaging techniques, and then to perform water-fat separation during post processing. Fat distribution can hence be evaluated based on the generated fat images. In the second category, chemically selective imaging is performed to generate fat-only images for further fat volume quantification.

A representative method in the first category is to make use the signal intensity difference of fat and water to achieve fat-water separation. Since lipids have a relatively short longitudinal relaxation time and a long transverse relaxation time, as well as a high proton density, lipid signal is usually bright on images obtained using non-chemically selective MR sequences. Lipid tissue can thus be differentiated from relatively darker lean-tissue. Therefore, fat-only images can be generated from an original image if high contrast between lipid and lean-tissue is obtained. The most widely used approach for fat quantification in this category is to use T1-weighted turbo spin echo (T1W TSE). It is readily available on most clinical scanners, and also offers high quality images. However, a relatively long TR has to be used to accumulate longitudinal magnetization before the next excitation, making image acquisition relatively slow. In addition, traditional T1W TSE sequences can suffer from low fat-water contrast, motion (i.e., bulk motion, respiratory motion, and bowel or cardiac motion) and flow artifacts. These drawbacks lead to degradation in image quality, resulting in difficulties in post-processing, and measurement errors. This is especially problematic for intraabdominal fat quantification. Usually, laborious contour drawing is used for fat quantification, which is both time-consuming and inaccurate.

There are also several methods in the second category. A well-known method is Dixon's method or its variations (5,6). It acquires two or multiple set of both magnitude and phase images with different TEs. It is different than most other approaches because it employs MR phase images to generate fat- and water-only images. Dixon's method usually can give a better water-fat separation than most other approaches. However, it generally

requires two or more scans, making it time-consuming and sensitive to motion. It also requires intensive post-processing and is therefore rarely used clinically.

Several other chemically selective approaches have also been proposed before to obtain fat-only images, such as inversion recovery SE or TSE (17), and water-suppressed T1W TSE (WS T1W TSE) (20). Inversion-recovery approaches offer much better fat-water contrast but are less commonly used because imaging duration is significantly lengthened. It also suffers from a relatively low SNR. WS T1W TSE can generate images with much higher fat-to-water contrast in almost the same scan duration compared with corresponding non-water-suppressed T1W TSE, and is therefore preferable. However, motion-induced artifacts, mostly along the phase encoding direction, are still a problem for accurate fat quantification. Therefore, for more accurate fat quantification, a rapid and chemically selective technique has to be developed.

3.3 Balanced Steady-State Free Precession (b-SSFP)

3.3.1 Introduction

There are a number of fast imaging techniques available in MRI, such as single- or multiple-shot echo-planar imaging (EPI) (21), and short-TR sequences (including incoherent imaging, and coherent imaging sequences). As EPI sequences can generate images which suffer severely from geometric distortion due to B_0 inhomogeneities and eddy currents, images generated using these sequences can not be used easily for accurate volume calculation. Among the short TR sequences, b-SSFP (also called true fast imaging with steady precession (TrueFISP), balanced-fast field echo (b-FFE), and fast imaging employing steady-state excitation (FIESTA)) is unique since it is a coherent imaging technique, and SNR improves as TR goes down (22). Although initially formally described in 1953 by Carr (23), balanced steady-state free precession (b-SSFP) has only gained interest recently for clinical imaging due to the increasing availability of high-performance gradient MR systems. B-SSFP has inherent advantages compared with other MR sequences such as high acquisition speed, and high SNR. The applications of b-SSFP sequences have been proposed in cardiac

imaging (24), MR angiography (25), MR diffusion imaging (26,27), MR thermometry (28,29), and functional MRI (30). As b-SSFP sequences are T_2/T_1 weighted, and adipose tissue has a relatively high T_2/T_1 compared with most lean tissues, fat signal can be undesirably bright since it may obscure nearby tissues of greater clinical significance. Conversely, b-SSFP sequences can provide high signal to noise ratio if fat signal is wanted.

3.3.2 Sequence Description

The b-SSFP excitation usually consists of an initial α/2 preparation pulse followed by a train of alternating ±α excitation pulses. The RF excitation timing paradigm is shown in Figure 3.1. The ±α pulses are separated by TR, whereas the time interval between the α/2 preparation pulse and the first −α pulse is TR/2.
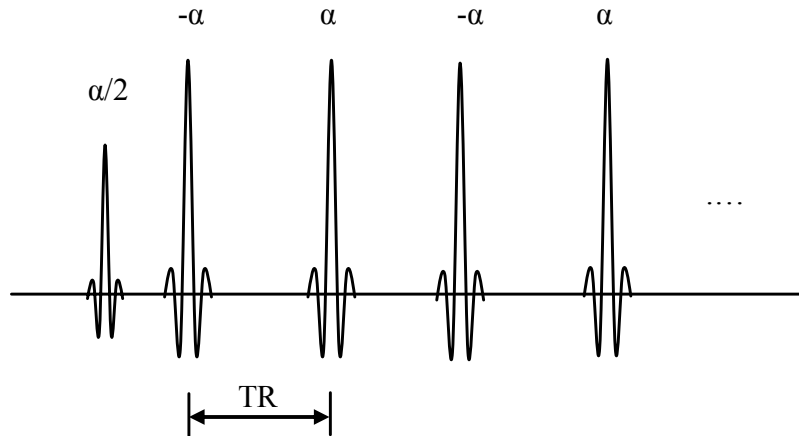
Figure 3.1 RF schematic of a b-SSFP pulse sequence. A preparation α/2 is used to catalyze the generation of a steady state. The first several acquisitions (dummy echoes) obtained in the transient phase are usually discarded to improve image quality.

The schematic of the pulse sequence in each TR cycle are shown in Figure 3.2. B-SSFP pulse sequence is characterized by the fact that no spoiling RF pulses or gradients are employed compared with other short TR gradient echo sequences. All gradient waveforms are balanced, leading to a refocused transverse magnetization at the end of TR. Since TR is usually much smaller compared with T_2 relaxation of most tissues, the residual transverse coherent magnetization from many previous RF excitations is actually reused in the following acquisitions, leading to a theoretically optimal SNR per acquisition time.
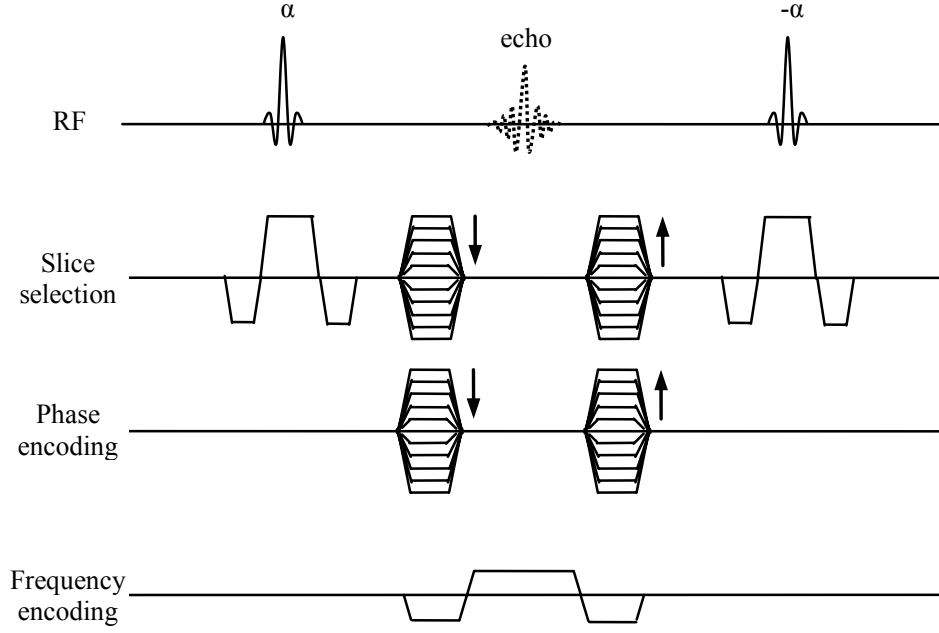
Figure 3.2 Diagram of the kernel of a 3D b-SSFP pulse sequence. TR is defined as RF-to-RF interval, and TE is defined as RF to the center of the following readout duration. Gradients along all three directions are balanced (zero net gradient) for transverse coherence signal imaging. The transverse coherent magnetization from previous RF excitations is reused in the subsequent acquisitions to achieve an optimal SNR efficiency.

3.3.3 Signal Properties

For balanced SSFP, when TR is much less than T_1 and T_2, the magnitude signal in the steady state for on-resonant spins can be described as (31):

$$S_{bSSFP} = k\rho \frac{\sin \alpha}{1 + \cos \alpha + (1 - \cos \alpha)(T_1 / T_2)} \tag{3.1}$$

where α is the flip angle. S_{bSSFP} here is only a function of flip angle: for a given tissue, with known T_1, T_2, the optimal flip angle α_{opt} for maximal signal is determined by $\cos \alpha_{opt} = (T_1 / T_2 - 1) / (T_1 / T_2 + 1)$, and the signal is approximately given by:

$$S_{bSSFP} = \frac{1}{2}k\rho\sqrt{T_2/T_1} \tag{3.2}$$

Hence flip angle-optimized b-SSFP signal is essentially $\sqrt{T_2/T_1}$-weighted (or T_2/T_1-weighted), and is influenced little by the change of TR and TE when both of them are much smaller than T_1 and T_2 of imaged tissue.

3.3.4 Magnetization Prepared b-SSFP Imaging

The b-SSFP pulse sequences discussed earlier will generate non-chemically selective images. To perform water- or fat-suppression, modification and optimization of the contrast behavior of b-SSFP sequences have to be performed. This can be achieved through certain magnetization preparation techniques, such as inversion or spectrally selective pulses. Magnetization preparation techniques are widely used in combination with turbo gradient echo (or turbo field echo, TFE) or turbo spin echo (TSE) readout train. Ideally, the contrast of the magnetization-prepared sequences is purely determined by the preparation phase, and the acquisition block is used to detect the prepared magnetization. In real situations, signal contrast is further influenced by the relaxations during the signal readout phase. B-SSFP is particularly suited to read-out prepared magnetization as it is ultra-fast, and offers optimal SNR per unit of acquisition time.

Two magnetization preparation approaches have been proposed for b-SSFP sequences. The first is magnetization prepared single-shot b-SSFP as shown in Figure 3.3. This approach is comparable to the magnetization prepared TFE or TSE. As in those sequences, the prepared contrast is partially modified by the b-SSFP contrast. Therefore, centric (or low-high) reordered phase acquisition is usually used to acquire central k-space soon after magnetization preparation.
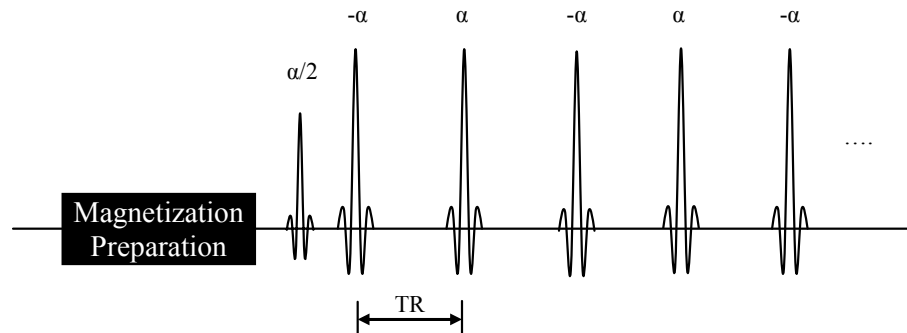
Figure 3.3 Magnetization prepared single-shot b-SSFP. After the magnetization preparation, b-SSFP is started with an α/2 preparation pulse.

The second approach is to perform magnetization preparation during steady-state (32,33). This approach maximally utilizes the already established steady-state from the previous shot and is therefore both time-efficient and effective. The scheme of this approach is shown in Figure 3.4. The steady-state magnetization is preserved in the longitudinal direction by the -α/2 pulse before the magnetization preparation. The magnetization is then modified by the preparation phase and the needed magnetization is therefore restored by the α/2 pulse before the new b-SSFP readout train.
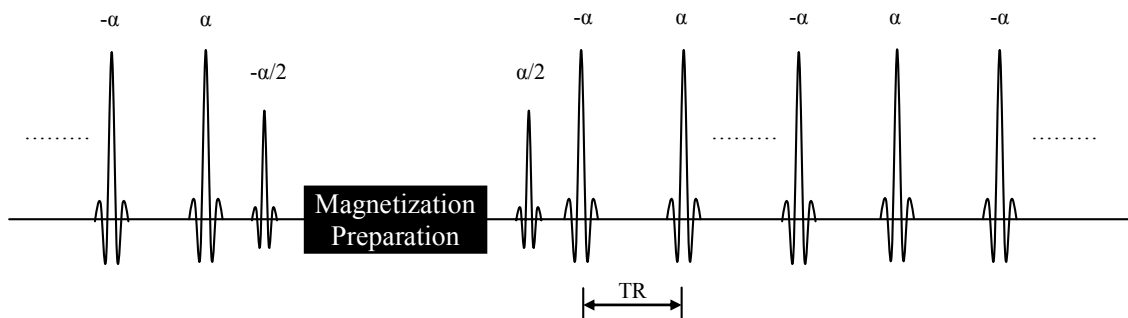
Figure 3.4 Magnetization preparation during the steady-state of b-SSFP. The steady-state magnetization is stored in longitudinal direction before magnetization preparation, and is recalled after preparation.

3.4 Fat Imaging Simulation

As T_1 of lipid tissue is short compared with most lean tissues, T1W SE sequences or their faster derivatives (e. g., TSE) are usually used for fat imaging. A TSE sequence has similar contrast behavior to a conventional SE sequence with the same TR and TE. For an SE sequence, the steady state signal can be characterized by:

$$S_{SE} = k\rho(1 - 2e^{-(TR-TE/2)/T_1} + e^{-TR/T_1})e^{-TE/T_2}$$

(3.3)

where the quantity k is a proportionality constant which depends on the sensitivity of the signal detection circuitry on the imager, and the values of T_1, T_2, and ρ (spin density) are specific to a tissue or pathology. If TE $\ll$ TR and TE $\ll$ T_2, *exp(-TE/T₂)* and *exp(TE/T₁)* are close to 1; thus S_{SE} is only a function of TR, which leads to:

$$S_{SE} = k\rho(1 - e^{-TR/T_1})$$

(3.4)

For balanced SSFP, when TR is much less than T_1 and T_2, the magnitude signal in steady state can be described as (31):

$$S_{bSSFP} = k\rho \frac{\sin\alpha}{1 + \cos\alpha + (1 - \cos\alpha)(T_1/T_2)}$$

(3.5)

where α is the flip angle. S_{bSSFP} here is only a function of flip angle: for a given tissue, with known T_1, T_2, the optimal flip angle α_{opt} for maximal signal is determined by $\cos\alpha_{opt} = (T_1/T_2 - 1)/(T_1/T_2 + 1)$, and the signal is approximately given by:

$$S_{bSSFP} = \frac{1}{2}k\rho\sqrt{T_2/T_1}$$

(3.6)

The simulated signal behavior of fat and some other abdominal organs for T1W SE (using Equation 3.3) and b-SSFP without water-saturation (using Equation 3.5) is shown in Figure 3.5. If TR for SE and flip angle for b-SSFP are selected appropriately, both techniques offer high fat signal and adequate fat-water contrast. The selection of TR for T1W SE/TSE and the selection of flip angle for b-SSFP are compromises between SNR and CNR. For SE/TSE, higher TR will offer better SNR but CNR is lowered. For b-SSFP, the optimal SNR for fat occurs at about 55° ~ 60°. A flip angle less than 55° is not desirable because it decreases both SNR and CNR. A flip angle greater than 60° will improve CNR, but SNR will

be reduced. If TR = 300 ms and TE = 10 ms for spin echo, and flip angle = 55° for b-SSFP are selected, fat-muscle contrast of b-SSFP vs. SE is 4.8 vs. 3.8, and fat signal is 0.28 vs. 0.61 (see Figure 3.5). This means that the b-SSFP technique inherently offers better fat-muscle contrast than the SE technique on typical imaging acquisition settings. If all other settings are the same, the signal of b-SSFP is about 1/2 of that of SE, but theoretical imaging speed is about 100 times faster than that of SE scans (TR = 200 ~ 500 ms for SE versus TR = 2 ~ 5 ms for b-SSFP), and is about 10 times faster than that of TSE scans (assuming a turbo factor of 10, e.g., 10 k-space profiles are acquired after one SPIR preparation). In addition, as b-SSFP is usually used with three-dimensional (3D) acquisition, SNR is improved significantly. Thus, b-SSFP may offer comparable SNR as T1W SE/TSE even when b-SSFP uses much higher acquisition bandwidth. The rest of this dissertation only compares the two rapid techniques (b-SSFP vs. TSE) since TSE is more commonly used clinically than SE in high field scanners.
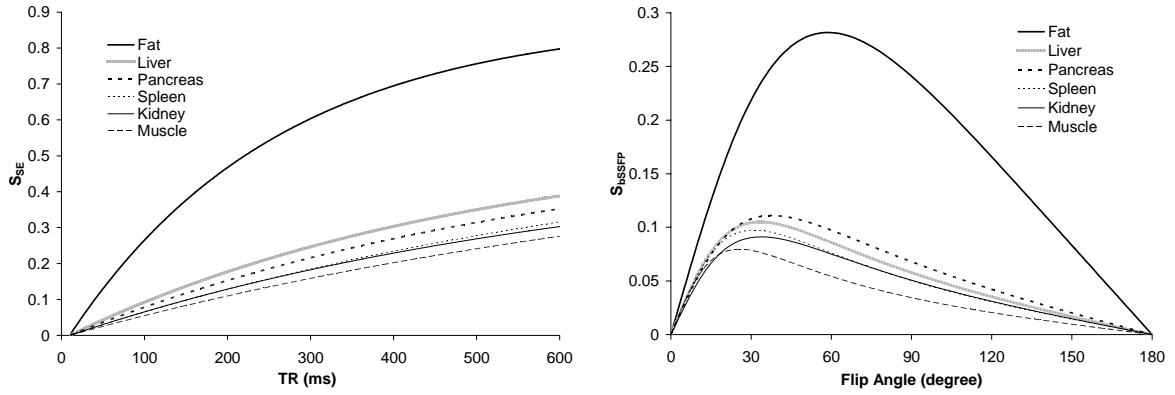
Figure 3.5 Simulated signal behavior of fat, muscle, and some abdominal organs. Left: T_1-weighted Spin echo sequence assuming TE = 10 ms. Right: T_2/T_1-weighted Balanced SSFP sequence if TR $\ll$ T_1, T_2 and TE = TR/2. ρ, T_1 (in ms), T_2 (in ms) values of the tissues used for the simulation are: fat (100, 252, 80), liver (70, 500, 45), pancreas (65, 600, 70), spleen (70, 775, 60), kidney (60, 650, 60), muscle (70, 870, 45). Values provided by Philips Intera 1.5T scanner.

As b-SSFP signal is subject to local B_0 inhomogeneity, signal amplitude changing with off-resonances was simulated as shown in Figure 3.6. It is clear from the simulation that b-SSFP gives a wide high signal plateau (pass-band) for fat which will tolerate resonance shifts

of ±170Hz without banding artifacts, and provides relatively constant signal for off-resonances less than 100Hz.
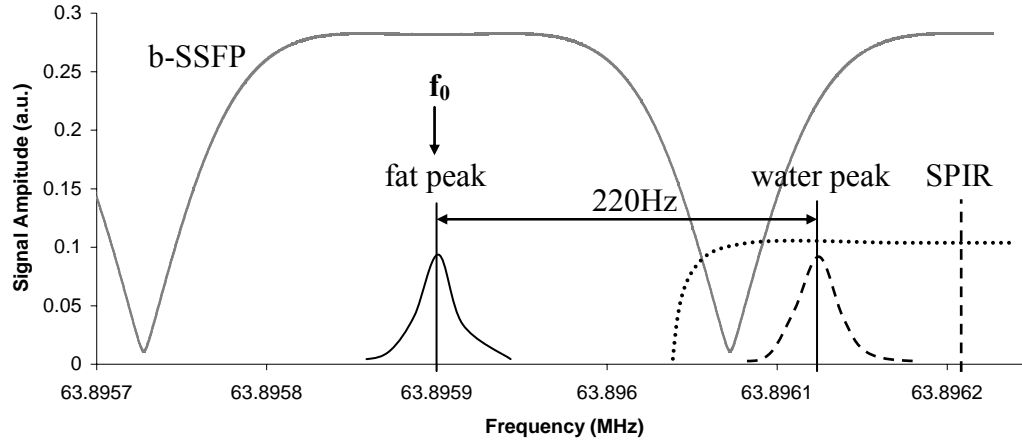
Figure 3.6 Spectral response of b-SSFP. It demonstrates water, fat frequency spectra and b-SSFP magnitude signal dependence on frequency. The synthesizer frequency f_0 is adjusted to the fat peak manually for fat imaging. The water signal is saturated using a SPIR pulse with a bandwidth of 340 Hz and with the center frequency manually shifted to +310 Hz. An off-resonance frequency of less than 100 Hz will lead to relatively constant and fat-only signal. B-SSFP signal is theoretically simulated with TR/TE/flip angle = 2.9 ms/1.2 ms/55°, and T_1/T_2 = 252/80 ms (fat).

3.5 Water Saturated b-SSFP (WS b-SSFP)

3.5.1 Pulse Sequence Design

From the theoretical analyses and simulations discussed previously, it is obvious that a b-SSFP sequence, in combination with magnetization prepared techniques to achieve water-suppressed fat images, would be promising for improved fat imaging. A clinically available magnetization prepared, segmented, 3D b-SSFP sequence (b-TFE, balanced turbo field echo, Philips Gyroscan Intera, Release 9.11) was employed and modified to test the effectiveness on fat imaging. To achieve water saturation instead of fat saturation in the default settings, the synthesizer frequency was first shifted to center resonant frequency of fat (a shift of -220Hz) before 3D WS b-SSFP scans. The schematic of the pulse sequence was shown in Figure 3.7. The water-saturation preparation block included an α/2 flip-back pulse, a 15-ms

spectral presaturation pulse (SPIR), a spoiler gradient to eliminate remaining coherent magnetization in the transverse plane, and an $\alpha/2$ preparation pulse. The SPIR pulse had a flip angle of 120°, a bandwidth of 340 Hz, and the frequency was manually shifted from -260 Hz to +310 Hz for water-saturation. Automatic shimming was applied to the volume of interest during the preparation phase. A small TR in b-SSFP sequences is essential to reduce off-resonance effects, as well as motion artifacts. In order to minimize TR, an asymmetric sampling (62.5%) was used resulting in a TR of 2.9 ms and a TE of 1.2 ms for a 160-sample readout (x-) asymmetric echo (leading to an x- resolution of 256) in all the phantom and human studies (34). The phase-encoding direction was left-right to minimize respiratory motion. A flip angle of 55° was used to obtain optimal signals for fat, and the echo train length (ETL) was 128 with 12 dummy echoes, leading to an SSFP readout window of about 370 ms for each shot. The TFE shot interval (or SPIR-SPIR interval) was determined automatically by the scanner and was therefore not fixed (604.2 ms for phantom protocol, and about 509 ms for human protocols). The signal contribution from the T_1-recovered magnetization from water was minimized by using a center-out profile order along y-direction, and a linear phase encoding in the slice-encoding (z-) direction. The magnitude signal behaviors of water and fat spins for b-SSFP with these parameters were simulated and are as shown in Figure 3.6. Since TR was not limited to specific values which make water resonant frequency center at the adjacent signal pass-bands as shown in Figure 3.6, suppression of water signal was therefore important to reduce blurring and artifacts that may otherwise be introduced by transient signal oscillations in b-SSFP readout due to water off-resonances (33,35).
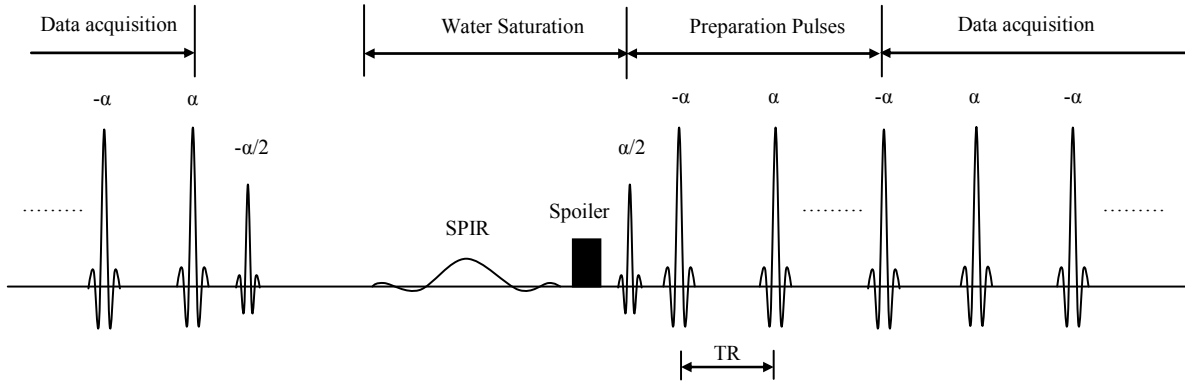
Figure 3.7 Schematic of the water-saturated 3D b-SSFP pulse sequence. The 0th moment of the gradients is balanced in each TR cycle so that transverse coherences are maintained. An α/2 pulse precedes the imaging echo train to force the magnetization toward steady state. Data acquisition is performed after 12 dummy cycles to reduce transient artifacts. The magnetization is tipped back to the longitudinal plane by another α/2 pulse before water-saturation SPIR is administered. A spoiler gradient is used to eliminate remaining coherent magnetization in the transverse plane before the next b-SSFP readout cycle.

3.5.2 Imaging Results

The pulse sequence was tested on a 44-year-old male volunteer on the abdomen for fat imaging. Informed written consent was obtained from the volunteer prior to the exams. 8 slices were obtained with one breath-hold in 11 seconds. The sequence also had field of view (FOV) = 460 mm, slice thickness = 10 mm, and matrix size = 256 × 256. Other parameters are described in "Pulse Sequence Design" section. The resultant images are demonstrated in Figure 3.8. High quality images are obtained with few discernable image artifacts. Very high SNR of fat and very low signal from lean tissue (muscle, bowel, etc) are achieved from visual inspection. The high image quality obtained is consistent with the previous theoretical analyses. Phantom studies, quantitative analyses on the images obtained from more human subjects, as well as the comparison with the traditional methods on image quality and fat quantification accuracy, will be discussed in detail in Chapter 4.
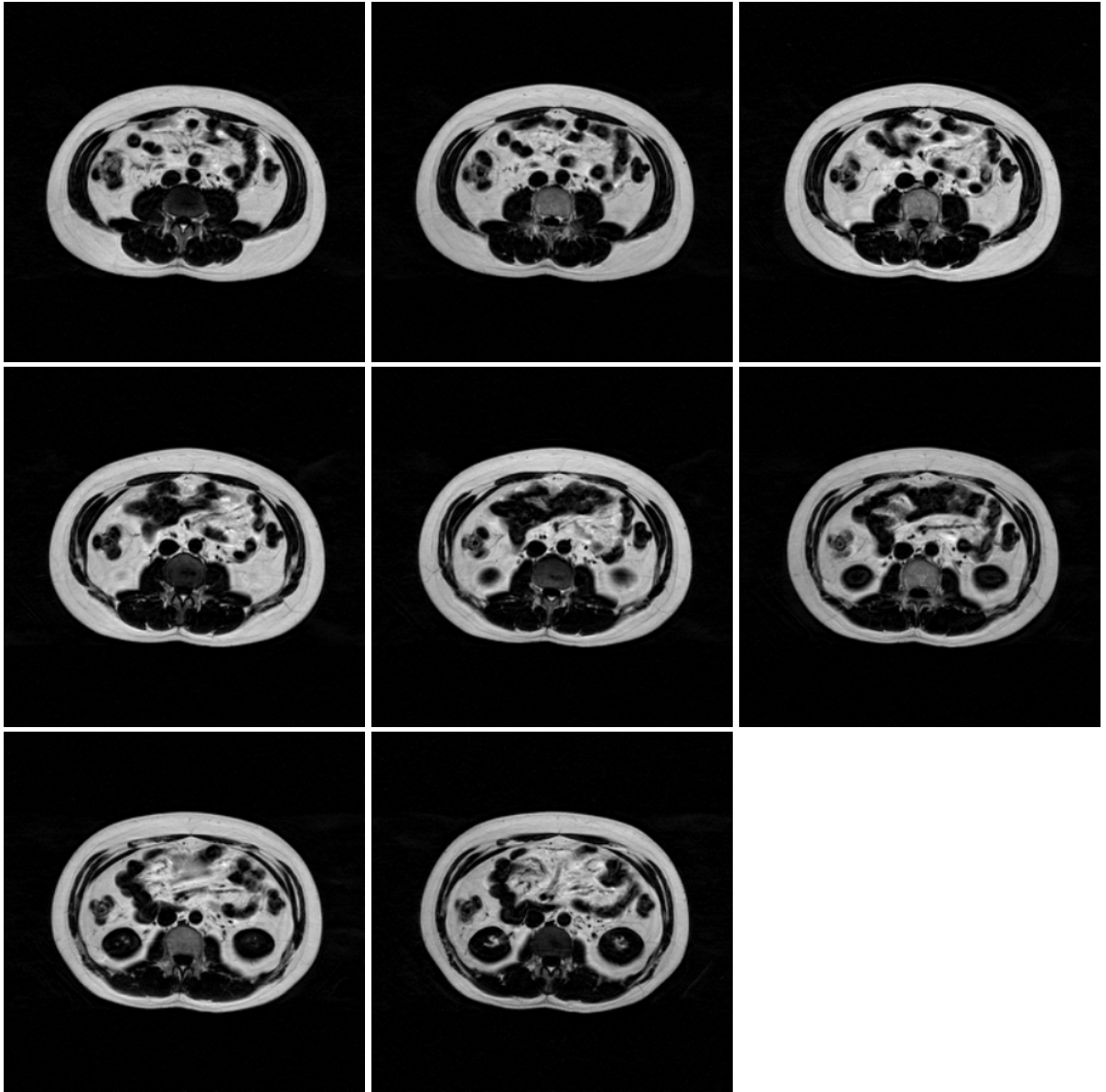
Figure 3.8 WS b-SSFP image results. Eight slices are shown, obtained in one scan on human abdomen with breathhold using the 3D WS b-SSFP pulse sequence. All images have high SNR on fat and have very low signal from non-fat tissue. They also have few artifacts due to motion, flow, and B_0 inhomogeneities, despite the difficulties of abdomenal imaging.

3.6 Summary

In this chapter, the principle of MR fat imaging using b-SSFP pulse sequences is discussed. The general SNR/CNR behaviors of b-SSFP are theoretically analyzed to compare

with the traditional T1W TSE approach. Much higher contrast between fat and non-fat tissue is further achieved by performing water saturation. High quality fat images are obtained on human abdomen with an optimized fat imaging pulse sequence on a 1.5 T clinical scanner. Therefore, this novel technique using WS b-SSFP is feasible for fat imaging.

Chapter 4 Abdominal Fat Imaging: Method Validation

4.1 Introduction

In Chapter 3, the theory and some simulated results of a novel rapid fat imaging technique, water saturated balanced steady-state free precession (WS b-SSFP), is discussed. In this chapter, this technique is used for human abdominal fat imaging. The resultant image quality and fat quantification accuracy are studied and compared with traditional methods, both in phantom studies and in human studies.

There are mainly two reasons to focus on validation of the method on human abdominal fat imaging and quantification. The first is due to the significance of fat quantification on human abdomen, as has been discussed in Chapter 3.

The second reason to investigate the novel fat imaging technique on human abdomen is due to the technical difficulties to image this region using MRI. Specifically, images obtained on human abdomen are easily degraded by geometric distortion, as well as a number of artifacts. The geometric distortion can originate from B_0 magnetic field inhomogeneities, gradient nonlinearity, and system imperfections (such as eddy currents). Geometric distortion can be particularly severe on human abdomen because a large field of view has to be employed to cover the whole abdomen. Image artifacts can be induced by B_0 and B_1 field inhomogeneity, bulk motion, respiratory motion, bowel motion, and blood flow. These problems lead to degradation in image quality, resulting in difficulties in post-processing, and measurement errors. This is especially problematic for intraabdominal fat quantification. Previous research suggests that the expected error of MRI measurements of intraabdominal fat is higher than that of subcutaneous fat (36,37). A recent phantom study also showed the same result for all three T1W MR sequences investigated (38). A fast MR sequence which gives accurate predictions of both intraabdominal and subcutaneous fat volumes would be significant for clinical and research purposes.

4.2 Phantom Study: Methods and Materials

4.2.1 Human Abdomen Phantom

To evaluate the performance of fat quantification of the WS b-SSFP sequence, a human abdomen phantom was constructed. It had dual-layered concentric cylinders (internal cylinder diameter = 17 cm, external cylinder diameter = 27 cm, length = 20 cm). The outer layer was filled with vegetable oil, while the inner cylinder was filled with the same oil, as well as an IV fluid bag, a bottle, and a tube, each filled with water fluids with different T_1 between 400 ~ 640 ms, T_2 between 60 ~ 90 ms, to simulate abdominal organs. The true volumes of oil in the internal cylinder and the external layer were 3.16 L and 6.34 L, respectively, simulating an intra-abdominal fat to subcutaneous fat ratio of 0.498. CT, and MRI (using both T1W TSE and WS b-SSFP sequences) scans were performed for oil volume quantification on the phantom.

4.2.2 CT Scans

CT scans were performed in the human abdomen phantom on a GE Lightspeed16 CT scanner operating in axial mode with the following parameters: 140 kvp, 250 mA, exposure time = 1 second, and FOV = 400mm. Each sequence was performed 3 times in three different days to get 3 independent image sets.

4.2.3 MRI Scans

All MR imaging experiments were performed on a 1.5 T clinical MR scanner with 30 mT/m, 120 T/m/s performance (Gyroscan Intera, Philips Medical Systems, Best, The Netherlands) and a standard quadrature-body coil was employed. A traditional T1W TSE sequence and a water-saturated, segmented, 3D WS b-SSFP sequence were scanned sequentially for each to obtain 20 axial slices with FOV = 400 mm, matrix size = 256 × 256, and slice thickness = 10 mm with no gap. For the T1W TSE sequence, the parameters were as follows: TR/TE/flip angle = 500 ms/5 ms/90°, turbo factor = 7 and readout bandwidth =

128 KHz. The scan duration was 58.5 seconds. For water-saturated 3D b-SSFP sequences, the imaging parameters were as follows: TR/TE/flip angle = 2.9 ms/1.2 ms/55°, ETL = 128 with 12 dummy echoes, and readout bandwidth = 200 KHz. The total scan duration was 33.3 seconds. A non-water-saturated 3D b-SSFP was also tested to investigate the outcome of the same b-SSFP sequence without water-saturation.

4.2.4 Post-processing

To evaluate the accuracies of oil volume quantification using the two methods, a computer software package developed in-house (Wafter) based on IDL was employed. The volumes of the oil in the internal cylinder and external layer on MR images were measured in the following manner. For each slice, a grey level histogram of the image was first generated for the whole image, and the optimal intensity threshold value to differentiate oil (i.e., fat) from non-oil pixels was visually chosen to generate a binary image characterizing the oil area (fat map). A region-of-interest (ROI) was then drawn manually on the fat map to include the whole phantom region to calculate total area of oil-pixels on this slice. Oil in the internal cylinder and external layer were differentiated by drawing a contour between them (e.g., internal ROI) and hence the area of oil-pixels in the internal ROI was also calculated automatically by the program. The oil area in the external layer for each slice was obtained by subtracting the area of the oil-pixels of internal ROI from that of the external ROI. The total oil volumes for internal oil and external oil were then calculated respectively by adding corresponding areas calculated from each slice times slice thickness. Finally, the internal to external oil volume ratio was then determined by dividing the internal oil volume by the external oil volume. The CT images were processed similarly, except two thresholds (upper-, and lower-threshold) had to be defined to obtain the desirable oil-only image, since oil signal is between signal of air and phantom materials.

Each of the three image sets were processed twice by one observer in different days to generate 6 data points for internal oil volume, external oil volume, total oil volume, and internal to external ratio. The percentages of the estimated to true values for each parameter by both techniques were calculated and further statistical analysis was performed to compare the accuracies for fat quantification. Single factor analyses of variance were used to

determine whether WS b-SSFP vs. T1W TSE and WS b-SSFP vs. CT predicted significantly different oil volumes and ratios.

4.3 Phantom Study: Results

4.3.1 WS b-SSFP vs. CT

Example images obtained using CT and WS b-SSFP are shown in Figure 4.1. As CT can only capture the density of the imaged object, oil, as well as phantom materials (tubes) are shown in the resultant image (Figure 4.1a). WS b-SSFP, however, is only sensitive to hydrogen spins, and since water spins are effectively saturated, fat-/oil- only images are obtained (Figure 4.1b).

The measured oil volumes/ratios are shown in Table 4-1 as the percentage of the corresponding true volumes or ratio. Both techniques provided very accurate predictions (error ≤1.5%). There was no statistical difference for internal and total volume predictions between the two modalities. The external oil volume, and internal/external oil volume ratio, however, are significantly different, although this difference is very small (1.2% and 1.7%, respectively). CT also provided a very accurate internal/external oil volume ratio (100.2%).
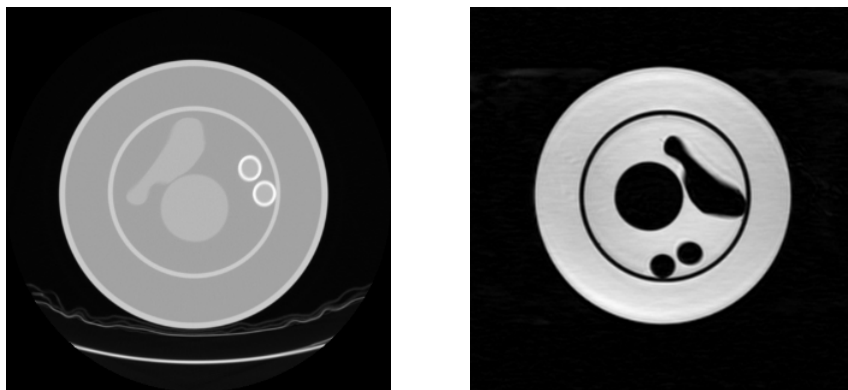
Figure 4.1 Comparison between CT and WS b-SSFP images. (a) CT example image on phantom. (b) Image obtained using water saturated b-SSFP (MRI) at the same slice position.

Although relatively accurate, CT is not preferable for fat quantification in the clinical environment due to the associated radiation exposure. It is especially not suitable for repeated studies of infants, children, and healthy subjects. It has been demonstrated in this study in phantoms that both CT and MRI (using WS b-SSFP) can provide accurate oil volume/ratio estimation. CT provides a more accurate internal/external oil volume ratio because any systematic geometric error of CT is corrected in the ratio calculation. WS b-SSFP provides slight under-estimation of internal oil volume, and slight over-estimation of external oil volume due to B_0 inhomogeneity and gradient non-linearity. The estimation error is, however, very small ($\leq 1.5\%$).

In human studies, the fast speed of CT may lead to more accurate fat quantification for intra-abdominal fat, as it is less sensitive to motion-induced errors. The disadvantage of CT is that, the signal intensity of fat is low, close to that of air and bowel gas. This may potentially lead to fat quantification error. It is also important to note that WS b-SSFP can provide fat-only images without the need of further image post-processing, and lends this technique to much easier fat quantification using automatic or semi-automatic fat quantification than CT.

4.3.2 WS b-SSFP vs. T1W TSE

Examples of the original images are shown in Figure 4.2, together with their gray level histograms, and the corresponding binary fat maps acquired using T1W TSE (left column), WS b-SSFP (middle column), and non-WS b-SSFP sequences (right column). No significant artifacts or distortion are noticed in images of T1W TSE and WS b-SSFP sequences (Figure 4.2a, and Figure 4.2b). Images obtained using both techniques show high SNR and CNR as can be seen from the histograms, which makes them adequate to differentiate oil in the phantom. Compared with TSE, however, WS b-SSFP images show a much better fat-water contrast as predicted, which gives a larger latitude for the selection of fat threshold. Adequate fat-water contrast is also obtained on the non-WS b-SSFP images as predicted, but transient artifacts of the water signal are visible along the phase-encoding direction (Figure 4.2c).
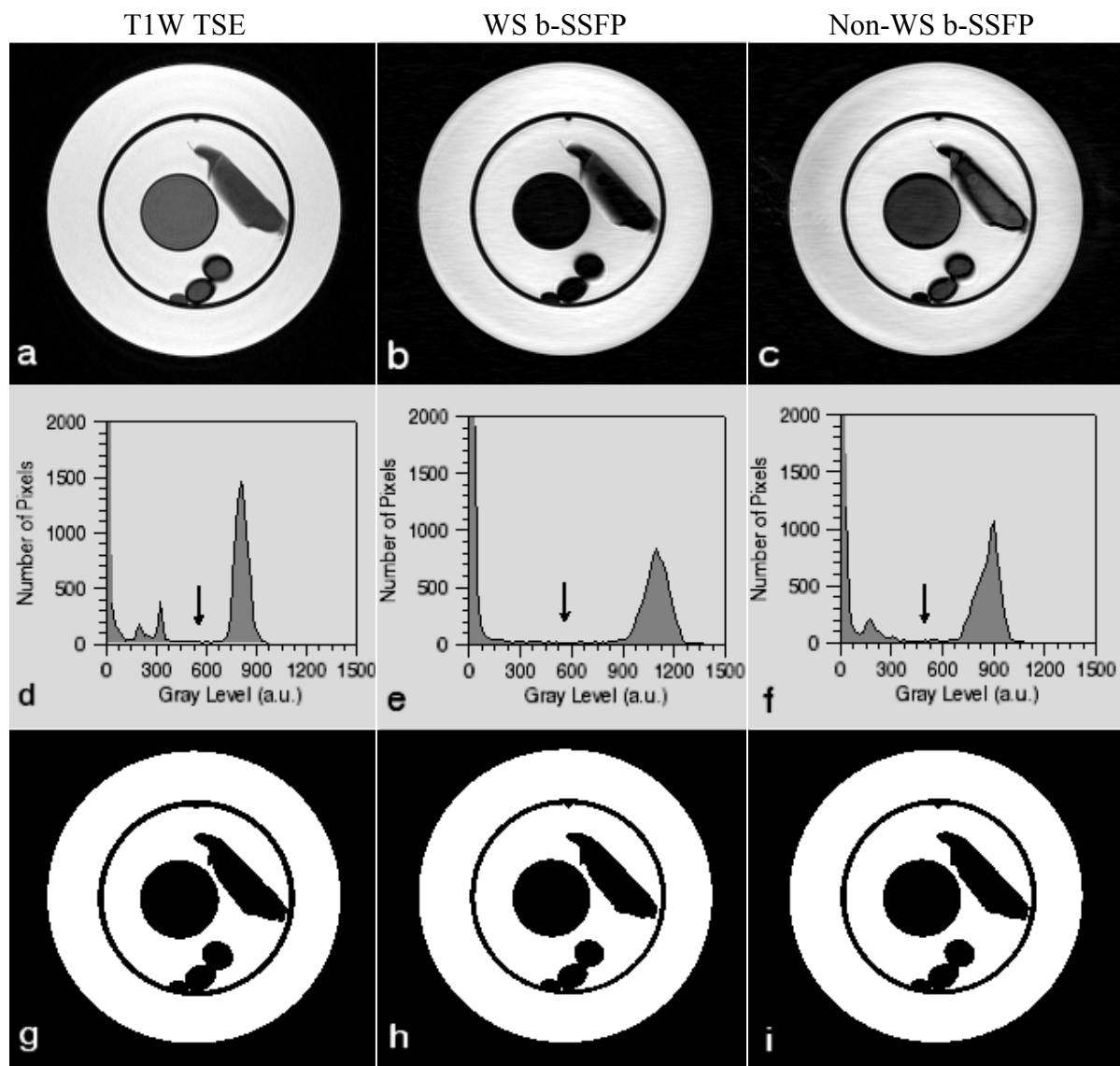
Figure 4.2 Representative phantom images. Phantom images and post-processing for T1W TSE (left column), WS b-SSFP (middle column), and non-WS b-SSFP (right column) sequences are shown. Fat images (g, h, i) for each sequence were generated using threshold values indicated by the arrows on the corresponding histograms (d, e, f). A much sharper fat-water contrast was obtained by using WS b-SSFP (b) compared to T1W TSE (a). An adequate water-fat contrast is also shown in (c) obtained by non-WS b-SSFP, confirming that b-SSFP sequences inherently provide good fat-water contrast even without water-saturation.

The measurement results of the two techniques (T1W TSE and WS b-SSFP) for oil volume in phantom are compared in Table 4-1. WS b-SSFP provided significantly improved estimation of all four parameters examined. In particular, the prediction of internal oil volume by b-SSFP was much more accurate than that of T1W TSE technique (with a mean value of 99.1% vs. 93.8%).

Table 4-1 Comparison of Phantom Oil Volume Measured Using CT, T1W TSE and WS b-SSFP (n = 6)

Repeat #	Internal			External			Total			Internal-external Ratio		
	CT	TSE	b-SSFP	CT	TSE	b-SSFP	CT	TSE	b-SSFP	CT	TSE	b-SSFP
1	100.3	93.5	99.7	99.7	98.0	100.7	99.9	96.5	100.4	100.6	95.4	99.0
2	99.7	95.2	98.5	99.4	98.5	100.3	99.5	97.4	99.7	100.3	96.6	98.2
3	98.7	93.8	98.1	99.2	98.4	100.5	99.1	96.9	99.7	99.5	95.3	97.6
4	100.0	92.6	99.8	99.7	98.1	100.9	99.8	96.2	100.5	100.3	94.4	99.0
5	98.7	92.4	100.8	99.1	98.0	101.2	98.9	96.1	101.1	99.7	94.3	99.6
6	100.3	95.5	97.5	99.5	99.5	100.2	99.8	98.2	99.3	100.8	96.0	97.4
Mean	99.6	93.8	99.1	99.4	98.4	100.6	99.5	96.9	100.1	100.2	95.3	98.5
Std Dev	0.7	1.3	1.2	0.3	0.6	0.4	0.4	0.8	0.7	0.5	0.9	0.9
$P_{TSE-bSSFP}$	<0.0001			<0.0001			<0.0001			0.0001		
$P_{CT-bSSFP}$	0.373			<0.0001			0.081			0.002		

*: All measurements are shown as the percentage of the corresponding true oil volume or ratio.

4.4 Human Study: Methods and Materials

4.4.1 Introduction

Several studies were performed to investigate the performance of fat quantification using WS b-SSFP on human abdomen. First, SNR and CNR of WS b-SSFP were compared with those of traditional T1W TSE and WS T1W TSE. Second, fat quantification using WS b-SSFP was compared with WS T1W TSE, which was regarded as an accepted gold standard, to validate the consistency of the two methods. Lastly, fat quantification using free-breathing WS b-SSFP vs. breathhold WS b-SSFP was also compared to study the feasibility of abdominal fat quantification with free-breathing MRI.

4.4.2 Subjects

15 healthy (6 female and 9 male) volunteers were recruited into the human study. The volunteers had a mean age of 41 years (range 27-60 years), and a mean body mass index (BMI) of 26.9 Kg/m^2 (range 20.7-38.1 Kg/m^2). Informed written consent was obtained from each volunteer prior to the examination.

4.4.3 MR Scans

Each subject underwent three or all of the following four scans: T1W TSE with breath-hold, WS T1W TSE with breath-hold, WS b-SSFP with, and without breath-hold. For T1W TSE sequence, 6 axial slices centered at L2-L3 level were acquired in two consecutive expired breath-holds, with 14 seconds each. Since b-SSFP is a much faster scan, 8 slices (with slice 2-7 imaged at the same positions of the 6 TSE slices) were obtained in 11 seconds which could be achieved in one breath-hold. All other imaging parameters were the same as these in the phantom studies, except that the FOV varied from 400 mm to 500 mm depending on the size of each volunteer. A non-water-saturated 3D b-SSFP scan was also tested on one subject to investigate the outcome of the same b-SSFP sequence without water-saturation.

4.4.4 Post-processing

All image post processing was performed using Wafter, and in-house computer programs written in IDL. For SNR and CNR comparisons, fat, muscle, and bowel content signals (S_{fat}, S_{muscle}, and S_{bowel}) were measured on hand-drawn ROIs on images obtained with T1W TSE, WS T1W TSE, and WS b-SSFP with breathhold. Noise (σ_n) was estimated from the background air anterolateral to the anterior chest wall. The SNR and CNR were defined as follows: $SNR_{fat} = S_{fat}/\sigma_n$, $CNR_{fat-muscle} = (S_{fat} - S_{muscle})/\sigma_n$, and $CNR_{fat-bowel} = (S_{fat} - S_{bowel})/\sigma_n$. SNR and CNR of each of the 6 common slices of the three techniques on every subject were calculated and averaged respectively to obtain the overall SNR and CNRs of this subject, leading to 6 datasets for each technique. Two-tailed paired sample t-tests were then performed in Microsoft Excel to determine the statistical significance of SNR and CNR differences between images obtained using WS T1W TSE, T1W TSE and WS b-SSFP sequences.

Fat quantification of WS T1W TSE, WS b-SSFP with and without breathhold was performed in the same manner as in the phantom studies. IAF, SAF, TAF were calculated for each method. Fat quantification results of WS b-SSFP with breathhold were compared with that of WS T1W TSE, and WS b-SSFP without breathhold, and statistical analyses were performed to study abdominal fat measurement differences using these methods.

4.5 Human Study: Results

4.5.1 SNR/CNR: WS b-SSFP vs. T1W TSE

Although WS T1W TSE offers much better fat-to-water contrast, T1W TSE is currently overwhelmingly used for abdominal fat imaging. Therefore, comparison between WS b-SSFP and T1W TSE was first performed.

Examples of the original images, corresponding histograms, and the processed fat images on volunteers using T1W TSE, WS b-SSFP with and without breath-hold are shown in Figure 4.3. While T1W TSE images suffer from bowel motion and flow artifacts (Figure

4.3a), only hardly noticeable artifacts are shown on images obtained using WS b-SSFP with breath-hold (Figure 4.3c). Images obtained using free-breathing WS b-SSFP appear to suffer only slight respiratory motion artifacts (Figure 4.3b), indicating that the WS b-SSFP sequence is not very sensitive to respiratory motion.

The calculated SNR and CNR results for T1W TSE and breath-hold WS b-SSFP are shown in Table 4-2. Fat SNR in b-SSFP data was poorer than that of T1W-TSE (103 vs. 108). However, fat-muscle CNR, and fat-bowel CNR were significantly improved to a much greater degree (99.6 vs. 70.3, 97.1 vs. 57.8) by using b-SSFP over T1W TSE.
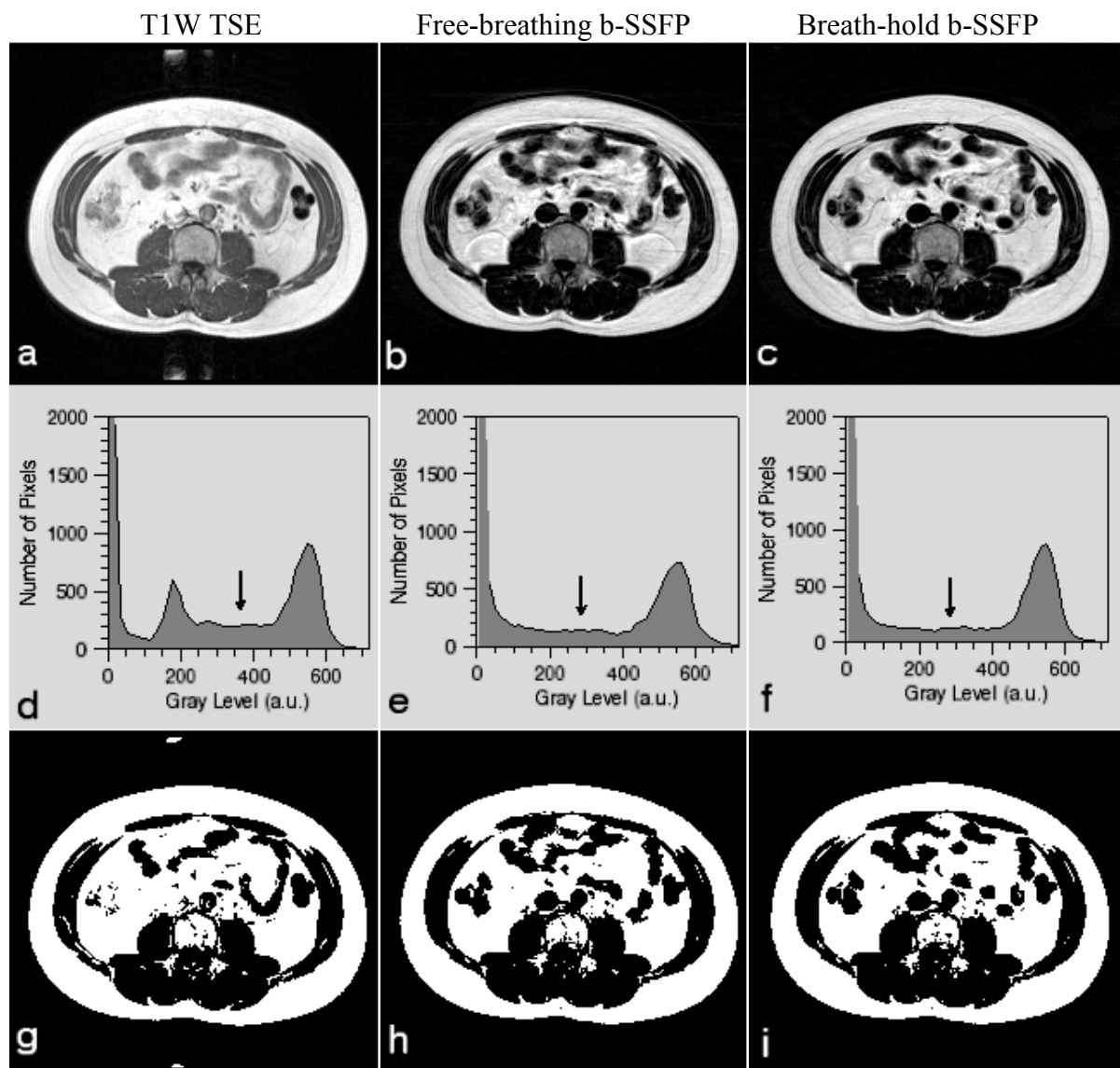
Figure 4.3 Example images from a volunteer using T1W TSE (left column), free-breathing WS b-SSFP (middle column), breath-hold WS b-SSFP (right column). Fat images (g, h, i) for each sequence were generated using threshold values indicated by the arrows on the corresponding histograms (d, e, f). Note the obvious bowel motion during the three consecutive scans. Much sharper fat to muscle and fat to bowel contrast was obtained by using 3D WS b-SSFP (b, c) compared with T1W TSE (a), and only slight respiratory motion artifacts were noticed on image (b) which was obtained without breath-hold, demonstrating that this b-SSFP sequence is not highly sensitive to respiratory motion.

Table 4-2 SNR and CNR Comparison on Human between T1W TSE and Breath-hold WS b-SSFP Sequences (n=6)

Subject	SNR$_{fat}$		CNR$_{fat-muscle}$		CNR$_{fat-bowel}$	
	T1W TSE	b-SSFP	T1W TSE	b-SSFP	T1W TSE	b-SSFP
A	124	109	82.8	107	63.1	103
B	119	117	76.1	113	56.4	110
C	90.9	88.4	60.8	85.7	47.8	83.0
D	102	97.3	63.0	92.7	65.3	93.2
E	92.8	89.5	59.2	85.8	55.4	84.5
F	124	117	79.9	113	58.8	109
Mean±SD	108±15.1	103±13.1	70.3±10.5	99.6±13.1	57.8±6.2	97.1±11.9
P	0.045		<0.0001		<0.0005	

4.5.2 SNR/CNR: WS b-SSFP vs. WS T1W TSE

Example images of WS T1W TSE and WS b-SSFP are shown in Figure 4.4. WS TSE images (Figure 4.4a) tend to suffer from slight motion artifacts due to bowel motion and residual respiration. No obvious motion-induced artifacts were noticed on WS b-SSFP images (Figure 4.4b) as imaging bandwidth along phase-encoding directions is high. WS b-SSFP images, however, suffer slightly from transient effects of off-resonant fat spins.
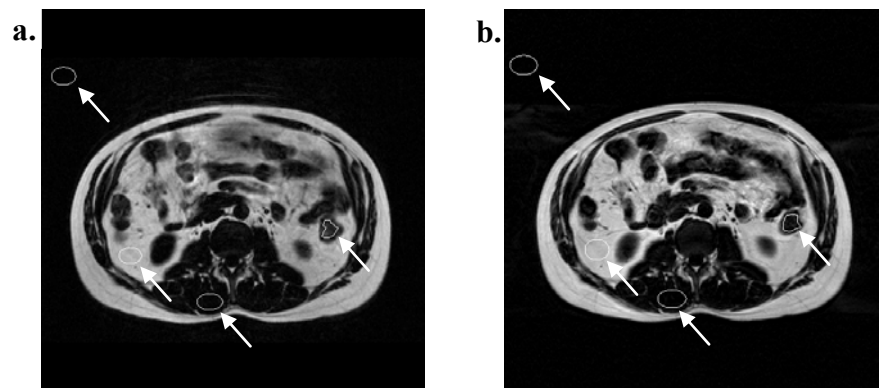
Figure 4.4 Comparison of WS T1W TSE and WS b-SSFP. (a) Water-suppressed T1W TSE. (b) WS b-SSFP at the same slice position. Examples of ROI contours are also shown in the two images (arrows).

SNR and CNR results on hand-drawn ROIs are shown in Table 4-3. SNR_{fat}, $CNR_{fat-muscle}$, and $CNR_{fat-bowel}$ of WS b-SSFP are significantly higher than that of WS T1W TSE (all $P<0.005$), with the improvement being 21.2%, 24.5%, and 31.3%, respectively.

Table 4-3 SNR and CNR Comparison between WS T1W TSE and WS b-SSFP (n=6)

Subject #	SNR_{fat}		$CNR_{fat-muscle}$		$CNR_{fat-bowel}$	
	TSE	b-SSFP	TSE	b-SSFP	TSE	b-SSFP
1	91.3	105.5	87.0	103.3	82.4	100.8
2	95.9	121.0	91.5	117.3	87.2	115.3
3	80.3	110.2	75.9	107.5	70.4	103.6
4	88.5	96.7	83.5	93.2	68.9	89.8
5	77.6	96.6	74.8	94.8	70.5	91.6
6	77.2	89.8	71.6	86.7	65.9	83.2
Mean±SD	85.2±7.9	103.3±11.3	80.7±7.8	100.5±11.1	74.2±8.5	97.4±11.5
P	0.0028		0.0017		0.0003	

Employing water suppression/saturation techniques can greatly improve the CNR between fat and lean-tissues. However, SNR of the resultant images will be compromised when compared to corresponding non-water-suppressed sequences since a large portion of spins (water magnetizations) are suppressed. In the case of non-water-suppressed T1W TSE, SNR_{fat} decreases from 108 to 85.2 (23.6%) after employing water-suppression. WS b-SSFP, however, can provide superior SNR and CNR over WS T1W TSE due to the inherent high SNR property of coherent imaging, even though higher readout bandwidth and partial-Fourier acquisition are employed. The ultra-short TR (2.9 ms) increases SNR, decreases total scan duration, and minimizes the motion-induced artifacts that complicate abdominal imaging. Therefore, WS b-SSFP is preferable for fat imaging using MRI compared to WS T1W TSE.

4.5.3 Quantitative Validation: WS b-SSFP vs. WS T1W TSE

Fat quantification results of TAF, IAF, and SAF on both WS b-SSFP and WS TSE images on ten available subjects are shown in Table 4-4. For each subject, fat volumes from six common slices of WS TSE and WS b-SSFP were measured and summed in each method. The mean differences of the two methods of TAF, IAF, and SAF are only 0.34%, -0.25%, and 0.91%, respectively. TAF, IAF, and SAF volumes measured with WS TSE and WS b-SSFP sequences are also shown in Figure 4.5 to illustrate the correlation of the two methods. All measurement points are on or very close to the line of equality. To study whether they agree sufficiently, formal statistical analyses using Bland-Altman's method were also performed. The systematic bias and degree of agreement between two measurement methods can be easily shown on a Bland-Altman plot. The Bland-Altman plots of TAF, IAF, and SAF measurement of the two methods are shown in Figure 4.6. It is clearly shown from these plots that all the measurement differences are within the 95% of difference. Therefore, it can be concluded that the two methods are the same in terms of the measurement accuracy for human abdominal imaging, although more subjects are needed in the future study.

Table 4-4 Fat Quantification Comparison between WS T1W TSE and WS b-SSFP (n=10)

Subject #	TAF (cm^3)		IAF (cm^3)		SAF (cm^3)	
	TSE	b-SSFP	TSE	b-SSFP	TSE	b-SSFP
1	234.9	232.6	65.6	64.9	169.3	167.7
2	241.0	250.2	184.2	192.8	56.9	57.4
3	112.1	115.8	44.2	45.8	68.0	69.9
4	334.9	342.2	213.1	216.2	121.8	126.0
5	420.8	410.5	270.7	258.4	150.1	152.1
6	459.3	459.4	225.1	225.4	234.3	234.0
7	524.4	524.2	177.1	172.1	347.3	352.1
8	310.3	307.4	169.4	164.2	140.9	143.2
9	262.4	254.7	105.6	100.2	156.8	154.6
10	309.5	323.6	115.3	126.2	194.2	197.3
Mean	321.0	322.1	157.0	156.6	164.0	165.4
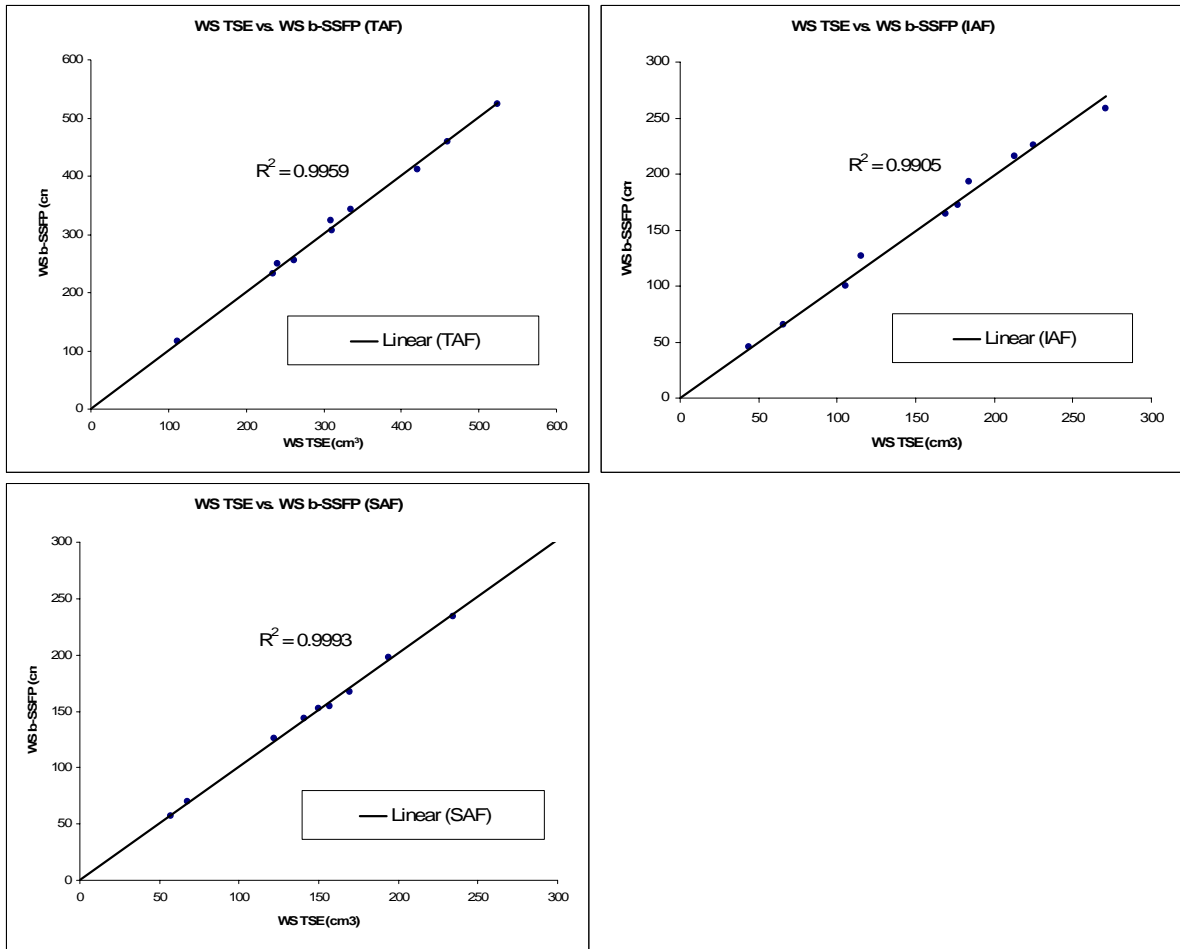
Figure 4.5 Correlation of fat volumes measured by WS TSE and WS b-SSFP. It shows TAF, IAF, and SAF volumes measured by the two sequences, with lines of equality. It is shown from the plots that the two methods agree well in the measurement of TAF, IAF, and SAF.
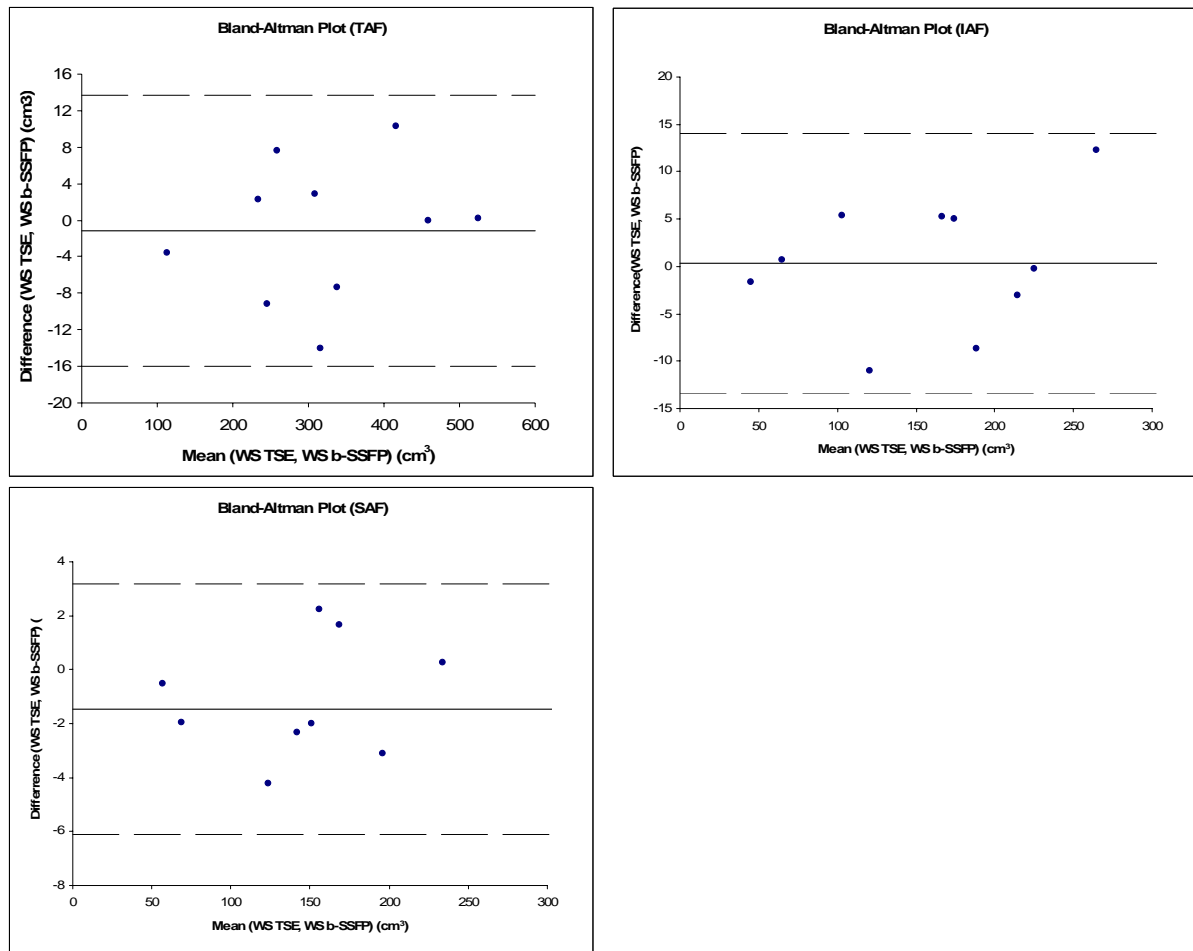
Figure 4.6 Bland-Altman plots of fat volumes measured by WS TSE and WS b-SSFP. The upper- and lower-limits represent 95% of differences (mean ± 1.96 standard deviation). The measurement differences are all within the limits, confirming that the two methods can be used interchangeably.

4.5.4 WS b-SSFP: Free Breathing vs. Breathhold

Examples of resultant images obtained using WS b-SSFP with and w/o breath-hold are shown in Figure 4.7. Compared with breath-hold WS b-SSFP (Figure 4.7a), free-breathing images suffer slightly more from motion-induced blurring in anterior portion of subcutaneous and intra-abdominal regions. Slight motion artifacts were also seen close to the kidneys, as indicated by the white arrows in Figure 4.7b.
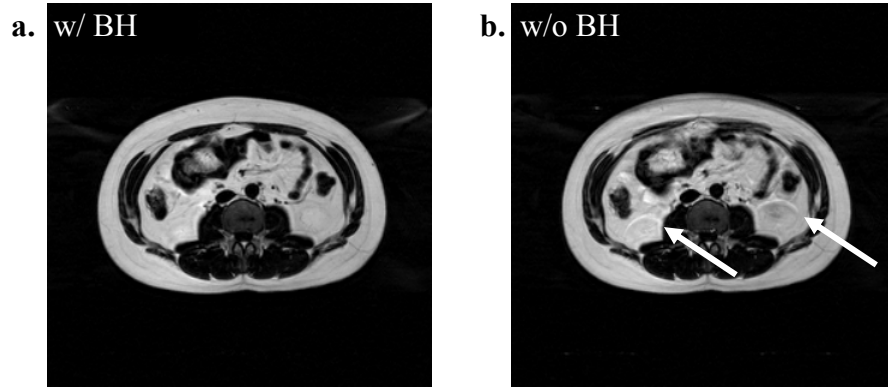
Figure 4.7 Comparison of WS b-SSFP with and without breathhold. (a) WS b-SSFP abdominal fat imaging with breathhold. (b) Same sequence without breath-hold imaged at the same slice position.

The data from the 11 subjects, as well as the statistical analysis are shown in Table 4-5. Pearson's correlation coefficients for all the four parameters investigated (intra-, sub-, total fat volume, and intra-/sub- ratio) are very close to 1.0 ($\geq$0.998), indicating the strong agreement between the two techniques. No statistical differences were found for subcutaneous fat volume and intra-/sub- fat ratio estimated using WS b-SSFP with and without breathhold (P = 0.11 and 0.47, respectively). Slight over-estimation of intra- and total fat volume were found by using free-breathing b-SSFP (1.1% for both, P = 0.04 and 0.02, respectively).

It has been shown that the proposed WS b-SSFP sequence suffers little from motion artifacts. This is due to the ultra-short TR that is used in the sequence, leading to a high acquisition bandwidth along phase-encoding directions. The centric phase encoding profile order used also contributes to its reduced sensitivity to motion. Statistical results show a strong linear correlation between breathhold and free-breathing variants of WS b-SSFP, and very close agreement in fat quantification estimation. Therefore, abdominal fat quantification using the proposed WS b-SSFP sequence without breath-hold is clinically feasible.

Table 4-5 Fat Quantification and Statistical Results for WS b-SSFP w/ and w/o Breath-hold (n=11)

Subject #	IAF (L)		SAF (L)		TAF (L)		IAF/SAF	
	w/o BH	w/ BH	w/o BH	w/ BH	w/o BH	w/ BH	w/o BH	w/ BH
1	0.31	0.29	0.97	0.97	1.30	1.27	0.32	0.30
2	0.57	0.56	0.80	0.79	1.39	1.38	0.72	0.71
3	0.25	0.26	0.77	0.77	1.02	1.04	0.32	0.34
4	1.05	1.06	1.08	1.08	2.19	2.19	0.97	0.98
5	1.24	1.27	0.78	0.76	2.09	2.10	1.60	1.66
6	1.08	1.02	0.84	0.84	1.95	1.90	1.29	1.21
7	1.35	1.32	1.43	1.42	2.85	2.81	0.95	0.93
8	1.70	1.62	0.96	0.95	2.70	2.60	1.77	1.71
9	1.41	1.38	0.71	0.71	2.23	2.20	1.97	1.93
10	0.28	0.29	0.43	0.43	0.73	0.73	0.65	0.69
11	0.70	0.69	0.92	0.91	1.67	1.65	0.76	0.76
Mean±SD	0.90±0.51	0.89±0.49	0.88±0.25	0.88±0.25	1.83±0.67	1.81±0.66	1.03±0.56	1.02±0.55
Pearson Correlation	0.999		1.00		0.999		0.998	
P	0.04		0.11		0.02		0.47	

4.6 Discussion

Abdominal fat quantification using MRI remains a technical challenge due the many problems it has with currently available scan techniques. The most popularly used techniques, T1W SE or TSE, suffer from low fat-water contrast, flow and motion-induced artifacts and long scan duration. Previously, water-suppressed TSE sequences have been found to be helpful to improve fat-water contrast (20). However, T1W TSE sequences are inherently slow and thus motion-induced artifacts are not avoidable. Although respiratory motion artifacts can be reduced by patient breath-hold or respiratory triggering, bulk motion and involuntary bowel motion are not predictable over the long scan duration. Fast imaging approaches are therefore preferable for abdominal fat imaging.

B-SSFP is a fast imaging technique which offers the best SNR per unit of time. It reuses the spin coherence and hence SNR improves as TR goes down (22). Since it has high bandwidth in both frequency- and phase-encoding directions, motion artifacts due to various sources are significantly suppressed. B-SSFP is particularly suited for fat imaging due to a combination of several factors. Firstly, b-SSFP is inherently T_2/T_1 weighted, and T_2/T_1 of fat (about 80/252 ms) is larger than most organs in human body, especially in the abdomen. Thus, b-SSFP sequences offer a fat to lean-tissue contrast superior to T1W TSE sequences. Secondly, by employing an optimal flip angle for fat, SNR (fat to noise ratio) is also much higher for fat while the water signal is low. Thirdly, a relatively long T_1 value of lean tissues makes WS b-SSFP less contaminated by water signal even when a long echo train length (ETL) is used for fat imaging. As most water-spins are tipped onto the transverse plane, then spoiled using spectral selective pulses before b-SSFP readouts, a slower T_1 relaxation of those spins allows a relatively longer ETL for fat spins to reach a steady state. In an inhomogeneous magnetic field, off-resonance behavior will lead to signal oscillation. A long ETL results in more signal acquired in the steady state, generating images with less blurring and artifacts even when the imaging FOV is large. The reverse applies to clinical b-SSFP imaging acquisitions using SPIR for fat suppression (like cardiac imaging); in this situation, images are easily contaminated by fat signal and transient artifacts due to the short longitudinal relaxation time of fat, and hence a short ETL has to be employed. This leads to a

frequently interrupted readout, and the water steady state is not adequately reached before the next preparation. These restrictions are especially problematic for imaging regions with large off-resonant frequencies, often leading to image blurring and artifacts.

Although the non-WS b-SSFP sequence also provides inherently high contrast between adipose and lean tissues as demonstrated in Figure 4.2c, water saturation plays a crucial role in obtaining high quality images for easier fat quantification. First, through the use of water-saturation, fat-only images are obtained directly, without further image processing, and fat regions can be differentiated easily by simple intensity threshold, due to the high water-fat contrast. Second, when water saturation is used, artifacts that might otherwise be introduced by off-resonant water signals are suppressed (the presented b-SSFP sequence does not impose a limitation on the choice of TR; therefore the water resonance frequency is not guaranteed to be on-resonant). Third, water saturation also suppresses flowing blood signal and hence the flow artifacts commonly seen in T1W TSE images are minimized. Although 3D b-SSFP sequences are widely regarded to be less sensitive to flow motion, they are not immune to such artifacts, especially for the edge-slices of 3D stacks with inflow spins (39), as shown in Figure 4.8c. In WS b-SSFP, a non-slice-selective SPIR pulse tips blood spins to transverse plane, even for spins outside of the FOV; flow effects in edge-slices are also suppressed (Figure 4.8d). A fourth reason for water saturation is that, it minimizes partial volume effects related to fat-water tissue mixing within a voxel. At 1.5T, a TR range of 2.3 to 6.9 ms (corresponding water-fat phase offset of 90° to 270° when TE is close to TR/2) will lead to serious partial volume effects as signal components of water and fat add destructively in each voxel, and this is eliminated by suppressing the water signal.
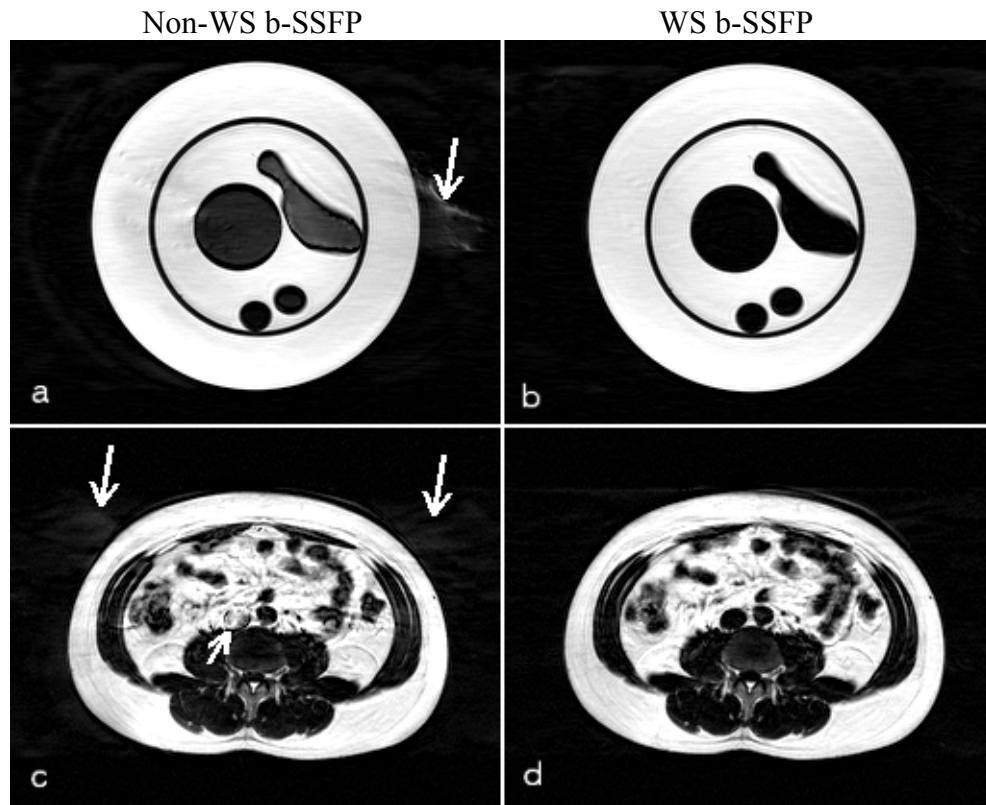
Figure 4.8 Comparison of b-SSFP with and without water saturation. Left column shows example images of phantom and volunteer studies using b-SSFP sequences without water-saturation, and right column shows same images with water-saturation. The two volunteer images (c, d) were both obtained without breath-hold. While WS b-SSFP images (b, d) suffer from fewer artifacts, transient artifacts originating from off-resonant water spins are obvious in both phantom and volunteer images (long arrows in a, c) in non-WS images. In addition, a flow artifact is also shown on the volunteer image (short arrow in c) due to the lack of water-saturation.

Several other approaches based on b-SSFP sequences (40-42) are reported to be effective on water-fat separation. Most of those sequences, however, try to obtain both water images and fat images, and are not optimized for abdominal fat quantification where only fat images are needed. Some of these techniques are derived from two- or multi-point Dixon's method (5,6,43,44) wherein several images with different TEs, or images acquired using several different synthesizer frequencies (42), are combined to calculate water-only and fat-only images. This is commonly accomplished either by repeating single-echo scans with different TEs (or synthesizer frequencies), or obtaining multiple echoes in one scan. The

former approach dramatically lengthens scan duration and is thus rarely used. The later approach results in a large increase in the minimum achievable TR since multiple echoes have to be readout in each TR; this will decrease the width of signal pass-bands on the periodic frequency-amplitude profile of balanced SSFP (Figure 3.6). Multiple-echo b-SSFP sequences are therefore not preferable, particularly for abdomen regions where the field of view is large, and the field inhomogeneity is severe. Hargreaves et al. propose a method which can elegantly separate water and fat signals through the use of the phase information obtained from a specific combination of TR and TE (40). However, the specific TR and TE (4.6 ms and 2.3 ms at 1.5 T) that must be selected reduce the flexibility to choose other imaging parameters (e.g., FOV, matrix size). In addition, a TR of 4.6 ms is too large for abdominal imaging since banding artifacts occur readily on subcutaneous fat regions due to the large FOV. Hargreaves' technique also suffers from partial volume effects since the voxel size for abdominal fat imaging is relatively large (35.2 mm^3 per voxel if FOV = 480 mm, matrix size = 256, and slice thickness = 10 mm), leading to destructive addition of water and fat signals in the same voxel. It should be noted that all of the above mentioned techniques also involve complicated post-processing to generate fat-only images before fat quantification can be performed.

As b-SSFP is sensitive to B_0 inhomogeneity, care has to be taken to ensure banding artifacts do not arise in subcutaneous regions. The steps to achieve this involve minimizing TR, obtaining a high quality shim and limiting the number of slices for the 3D stack. To image the whole abdomen in one scan, multiple stacks have to be planned and imaged serially. During this process, each stack must be moved to the most homogeneous region of the magnet (isocenter), and automatic or volume shimming must be performed before scanning. The number of slices per stack will vary depending on the size of the subject to ensure banding artifacts are avoided. If slice thickness is 10 mm in 3D mode, 6~7 slices for larger subjects (FOV ~ 500 mm) and about 9~10 slices for smaller subjects (FOV ~ 440 mm) ensures the avoidance of banding artifacts, at least in our experience (TR = 2.9 ms with manufacturer auto shimming). Limiting the number of slices in each 3D stack also reduces sensitivity to respiratory and bulk motion, and results in less geometric distortion due to the

more uniform B_0 and more linear gradient field in the 3D FOV close to isocenter. T1W TSE sequences are generally believed to be less sensitive to B_0 inhomogeneity, and the whole abdomen is usually imaged in one scan without table motion. However, although the resultant images suffer less from artifacts induced by off-resonance spins, geometric distortion may be severe without being recognized, especially when a low readout bandwidth is used (45). Such distortion may introduce considerable errors in both intraabdominal and subcutaneous fat volumes, as well as their ratio since they are distorted to a different degree. B-SSFP images, however, suffer much less from geometric distortion and chemical shift artifacts as the images are obtained at or close to the isocenter, and the maximal acquisition bandwidth is usually applied, leading to more accurate fat volume quantification.

The WS b-SSFP sequence proposed herein provides additional great flexibilities. Higher resolution images can be obtained using this technique by simply increasing matrix size, as no limitation on the selection of TR is imposed. For less cooperative patients, 2D single-slice or sequential 2D multi-slice WS b-SSFP sequences can be employed, and each image can be acquired in less than 0.7 second; respiratory and bulk motion artifacts are therefore minimized. This sequence is also compatible with parallel imaging, which may improve imaging speed even more. Most importantly, free-breathing WS b-SSFP has been validated to be adequate for fat quantification without greatly compromising accuracy. The use of non-breath-hold acquisitions will decrease total MR exam duration, will increase scanner throughput, and will decrease both operator and patient involvement.

4.7 Summary

A safe, reliable, and cost-effective adipose tissue imaging method is strongly demanded in both clinical and research arenas. Both MRI and CT can generate 2D and 3D images for the study of fat distribution and quantification. MRI is preferable, especially for infants, children, and healthy subjects, because it imposes no radiation exposure compared with CT. On phantom studies, the proposed WS b-SSFP sequence gives more accurate oil volume estimations compared with T1W TSE, and very close estimation compared with CT. On human studies, it offers much improved CNR and very close SNR compared with

traditional T1W TSE, and provides both significantly better CNR and SNR compared with WS T1W TSE, in much shorter scan duration. Fat quantification using WS b-SSFP has also been compared with that of WS TSE on ten volunteers, and the results agree well. In addition, free-breathing WS b-SSFP has also been validated for abdominal fat imaging and quantification without greatly compromising accuracy of the measurement. Although in this chapter, the focus has been on the application to abdominal adipose tissue imaging, water-saturated, 3D b-SSFP may be readily applied as a general means for whole-body (46,47), muscular (48,49), and epicardial (50,51) adipose tissue imaging. Since fat quantification calculations based on the resultant images requires negligible post-processing (see more in Chapter 5), it is a preferable method for both clinical and research purposes.

Chapter 5 Abdominal Fat Quantification

5.1 Introduction

Fat distribution measurement on human is of great significance for a cluster of obesity-related diseases generally referred to as metabolic syndrome. How fat distribution correlates with these diseases is still a very controversial subject. In addition, monitoring the change of fat distribution longitudinally for patients with metabolic syndrome after pharmaceutical intervention or life style change is also of great importance for improved drug development/test and disease treatment.

Rapid and accurate fat quantification on MR images obtained in the human abdomen has been a challenge since MRI was first used for fat distribution imaging. Although fat signal is usually significantly higher than non-fatty tissues, several factors may complicate the quantification of fat. First, the image quality is usually compromised by a number of motion artifacts. Patient bulk motion, respiratory motion, and involuntary peristalsis can all contribute to these artifacts. Second, images obtained using traditional methods usually suffer from blood flow artifacts, if water suppression is not performed. Third, the traditional methods may have relatively low SNR and CNR, because several images have to be acquired in a limited time window as breath hold is usually mandatory to minimize respiratory motion. Another factor that contributes to the difficulties is that the signal intensity of different non-fatty tissues is not the same, as T_1 and T_2 vary. In addition, the images may be contaminated by artifacts due to blood flow. A representative image obtained using T1W TSE and the corresponding histogram is shown in Figure 5.1. For these reasons, rapid automated or semi-automated fat quantification methods have difficulties achieving reliable fat volume measurement. Therefore, manual contour drawing still seems to be the most accepted approach for fat quantification, although it is slow, and suffers greatly from inter- and intra-observer variations. In addition, partial volume effects can not be accurately evaluated using a manual contour drawing method.
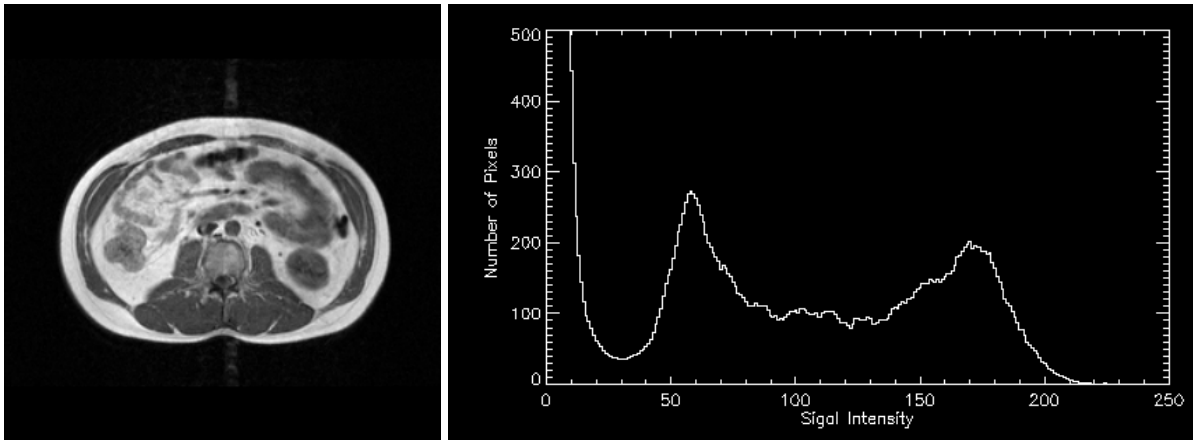
Figure 5.1 Representative TSE abdominal image and the histogram. The contrast between fat and non-fatty tissue is not always high enough, and the water and fat signal peaks are overlapping in the histogram.

Despite these difficulties, several automated or semi-automated approaches have been proposed for the quantification of non-water-suppressed abdominal images. Lancaster et al proposed a threshold method based on the image histogram and studied two adaptive procedures to seek a threshold signal intensity to separate fat and nonfat pixels (52). However, neither of the two procedures they studied, namely the center and valley methods, are accurate due to the fact that water and fat peaks are overlapping, and the estimations might be quite biased particularly for subjects with very low or high visceral fat volume compared with non-fat volume. Positano et al have recently proposed an unsupervised method for the assessment of abdominal fat volume (53). They performed Gaussian curve fitting for the fat signal distribution on the histogram using those pixels with signal intensity higher than the average fat signal. This method works well if there is no contamination from water pixel signal in the region of curve fitting, but is still inaccurate if there is very low visceral fat volume compared with nonfat volume. Furthermore, this method does not consider the influence of the partial-volume effect on fat volume quantification. Therefore, it is also subject to very high systematic error.

0	0.2	0.25	0.03
0.3	0.95	1.0	0.7
0.4	1.0	1.0	0.8
0.1	0.5	0.7	0.3
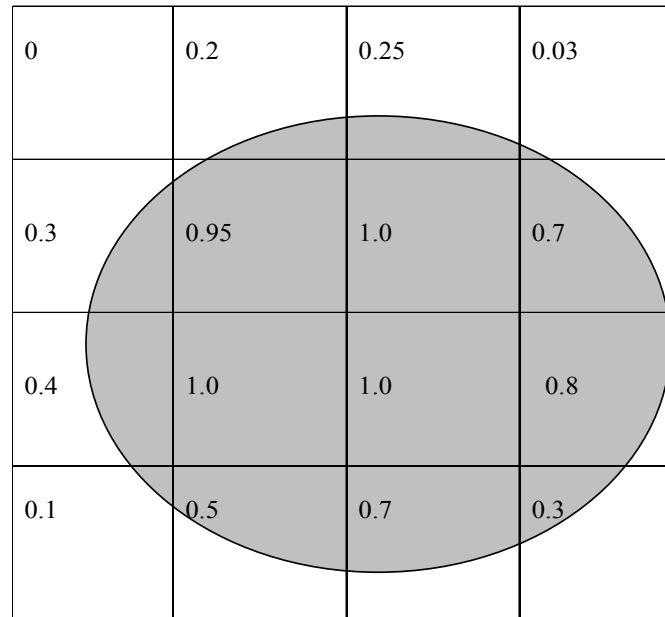
Figure 5.2 Partial-volume effects for a 2D object. An image voxel can be at the border of the object, leading to partial-volume effect. Partial-volume effect is more severe for 3D objects, and for objects with complex geometric shapes.

Due to the highly complicated anatomic components and the disseminated nature of intra-abdominal fat, partial-pixel fat volume may contribute a significant part to the total abdominal fat. The partial-volume effect is even compounded by the intestinal movement blurring or artifacts in human abdomen (54). It is particularly problematic for area/volume measurement using MRI, as MRI generally has much lower spatial resolution compared with CT. Therefore, a quantification method that can accurately evaluate partial volume fat will greatly improve the overall fat volume measurement accuracy, especially for normal or under-weight subjects (such as patients with lipodystrophy) (55).

The novel 3D WS b-SSFP sequence for rapid and accurate fat imaging has been described in Chapter 4. Using this method, high quality fat-only images which have significantly reduced motion artifacts, and suffer essentially from no blood flow artifacts, can be generated in very short scan duration. The contrast between fat and non-fat tissue is also greatly improved compared with traditional approaches such as T1W TSE, and WS T1W TSE. The histogram of a WS b-SSFP abdominal image is shown in Figure 5.3. It is clearly shown that fat signal peak is well separated from signal from background noise and artifacts,

as well as water signal peak (also close to zero). Fat quantification using a threshold approach based on the image histogram is therefore feasible to offer an accurate and rapid fat quantification. Furthermore, taking advantage of the high SNR and CNR obtained using this imaging technique, it might be feasible to achieve accurate partial-volume fat quantification using an automated approach, thus greatly improve the fat quantification speed and accuracy.
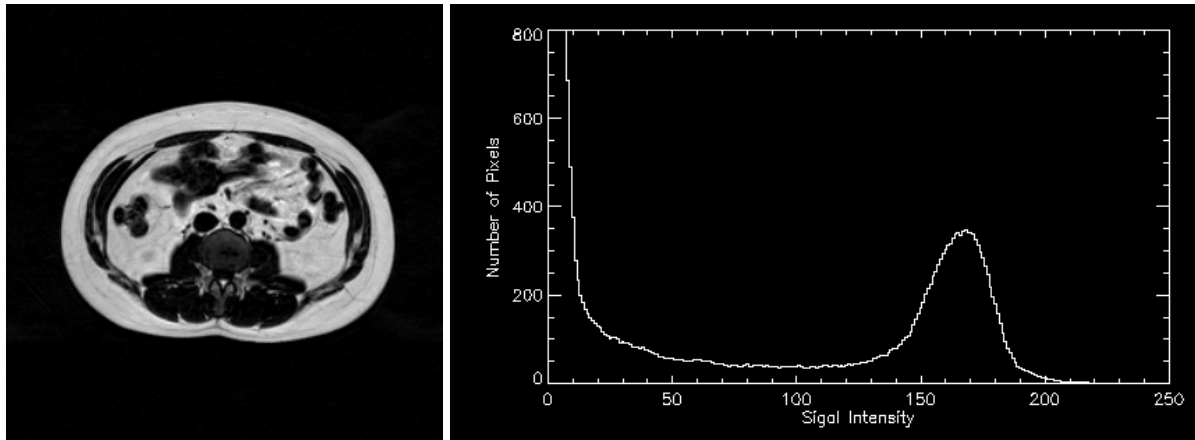
Figure 5.3 WS b-SSFP abdominal fat image and its histogram. Since water signal is effectively suppressed, fat signal peak is well separated from the peak close to zero, which includes both water, and air (noise) pixels. The pixels with intermediate signal between the two signal peaks are mainly pixels with partial-volume fat.

It is the goal of this chapter to discuss a novel automated fat quantification method for WS b-SSFP abdominal fat images. A simple fat distribution model is first discussed, which takes into account both full- and partial-volume fat pixels in an image. An automated method to evaluate fat volume using the proposed fat distribution model is tested and compared with a traditional full-voxel only quantification method in both phantom and human studies.

5.2 Fat Distribution Model

Due to the limited spatial resolution of any imaging modality, lipid tissue can be distributed in a full volume, and can co-live with water and/or air tissue for abdominal fat imaging. This is especially true for MRI, which is well-known to have much lower spatial

resolution compared with CT. The spatial resolution of MRI is mainly limited by SNR and imaging duration. The 3D WS b-SSFP imaging technique discussed earlier can improve the spatial resolution compared with other imaging methods. However, an acquired voxel on human abdomen can still be relative large due to the large FOV. In a ideal water-suppressed image (neglecting residual water signal, noise, and other imaging imperfections such as B_0 and B_1 inhomogeneities), signal intensity from a voxel full of lipid tissue would give a signal maximum of the image, and the signal intensity from a voxel partially filled with lipid tissue (the other part is filled with water and/or gas) would be proportional to the volume ratio of fat in that pixel. Thus, a simple fat distribution model is defined as follows:

Fat in an image can be distributed in either full-volume fat voxels, or partial-volume fat voxels. In voxels with full volume fat, they will ideally give a single signal maximum (S_{max}, with the number of pixels N_1). In partial-volume fat voxels, the signal is proportional to the volume ratio of fat ($0 \sim S_{max}$).

The voxels with full volume is mainly the static bulk fat, such as subcutaneous fat. Partial-volume fat pixels are located mainly at the fat tissue interface, and the lower signal can be due to partial volume fat filling, or due to intestine movement. Due to the complicated fat distribution and potential intestine movement, the distribution of the partial-volume fat signal on a histogram is not predictable. However, if the number of pixels in an image is large enough, the probability of any pixel to have a certain signal intensity less than S_{max} is equal. Thus, a uniform (or rectangular) distribution as shown in Figure 5.4(b) can be used to approximate the partial-volume fat signal distribution. The pixel density (N_2) in the histogram is image-specific, and should be derived from the image histogram. This assumption has to be validated experimentally.

Assumption: If number of pixels on an image is large, and fat volume is large, the partial-volume fat signal distribution is a uniform distribution, as shown in the following Figure 5.4(b).

(a) Histogram for full-volume voxels   (b) Histogram for partial-volume voxels
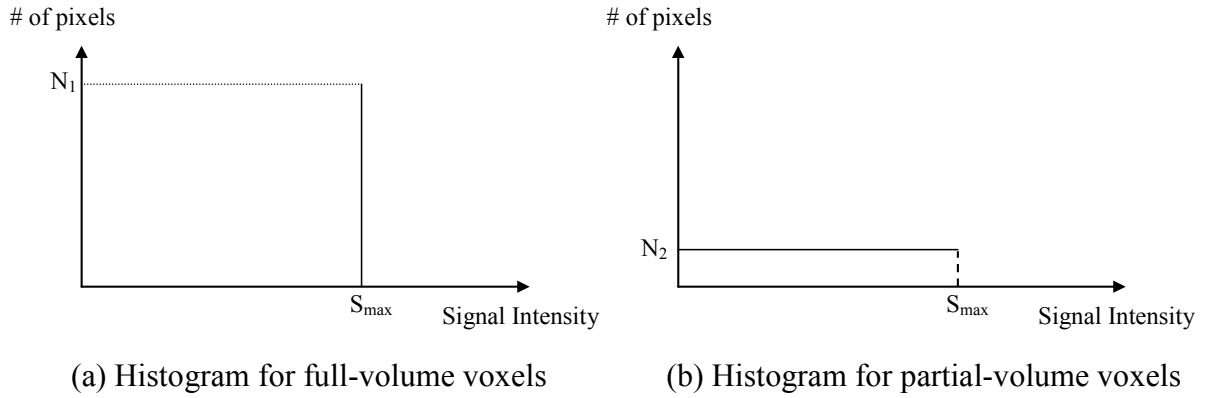
Figure 5.4 Histograms of full- and partial-volume voxels. (a) The ideal histogram of an image if only full-volume fat voxels are considered. (b) The histogram if only partial-volume fat voxels are considered. In both cases, imaging noise is neglected.

5.3 Quantification Method

Considering both full- and partial-volume fat, the image histogram is shown as the dashed lines in Figure 5.5(b) if an ideal imaging method is used, as predicted by the fat distribution model. With the imaging noise, and other system imperfections during imaging, the resultant histogram will be as shown in the solid curve in Figure 5.5(b), which is derived from the ideal histogram, convolved with a normalized Gaussian kernel representing Gaussian noise (standard deviation = σ) (Figure 5.5(a)). The background noise and suppressed water signal is also illustrated as the peak with signal intensity close to zero. Assuming a high SNR (defined as SNR = S_{max}/σ) is achieved, the histogram density (N_2) of partial-voxel pixels can be derived directly from the experimental histogram. Also, N_1, which represents the number of full-volume voxels, can be determined via curve fitting.

# of pixels

Gaussian kernel (normalized)

(a) Imaging noise

(b) Theoretical and expected histogram
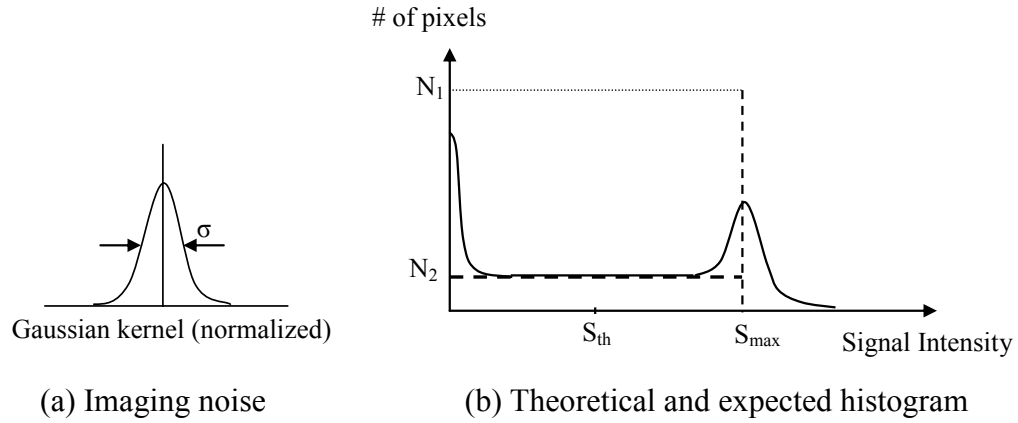
Figure 5.5 Theoretical and expected histogram of a fat image. Dashed lines show the theoretical histogram as predicted by the full- and partial-volume fat distribution model. Solid line shows the expected histogram of an MRI water-suppressed image, due to imaging noise, background artifacts, and residual water signal.

Because on average, partial-volume voxels are half filled, theoretically fat volume can be calculated as follows:

$$\text{Volume} = (N_1 + 0.5 \times N_2) \times \text{Full Voxel Size} \tag{5.1}$$

To provide further user flexibility, a corresponding signal threshold which best separates fat and non-fat can be determined as:

$$S_{th} = S_{max} /2 \tag{5.2}$$

Therefore, fat volume can also be determined as:

$$\text{Volume} = (N_1 + S_{th} \times N_2 / S_{max}) \times \text{Full Voxel Size} \tag{5.3}$$

Practically, the threshold (S_{th}) can be determined automatically by a computer program. Depending on the image quality, the threshold may or may not be adjusted by the observer before fat volume is automatically calculated. This method is implemented in a software algorithm (WAFTER) developed in IDL, which will be discussed in detail later in this chapter.

5.4 Phantom Study

5.4.1 Materials and Methods

The same human abdominal phantom and the 3D WS b-SSFP pulse sequence described earlier were used. Briefly, the phantom had dual-layered concentric cylinders with internal/external oil volumes of 3.16L/6.34L, simulating an intra-abdominal fat to subcutaneous fat ratio of 0.498. MR experiments were performed on three different days. On each day the scan was repeated with the phantom relocated, leading to six data sets. The internal, external, and total oil volumes were then measured using the semi-automated computer software (Wafter). In brief, a signal threshold was determined to generate a binary fat-only image. Two user-defined contours were then drawn to enclose the whole abdomen phantom, and to separate internal and external oil. The total oil volume and the internal oil volume were then calculated automatically by counting the number of fat voxels enclosed by each contour times the voxel size. External oil volume was calculated by subtracting internal volume from the total volume. Two different methods were used to determine the signal threshold. The first method used a threshold less than the minimum fat signal of the main fat peak in the histogram; therefore, only full-volume fat voxels were counted. The threshold determined using this method is referred to as Th_f, and the method is called Th_f method in the rest of this chapter. In the second method, the fat signal threshold was determined based on the model described earlier in the previous sections. Therefore, both full- and partial-volume fat voxels were included. The threshold determined using this method is referred to as Th_{fp}, and the method is called Th_{fp} method in the rest of this chapter. A single factor analysis of variance (Anova) was used to determine whether the two techniques predicted significantly different oil volumes and ratios. A *P* value of less than 0.05 was considered statistically significant.

5.4.2 Results

A representative phantom image obtained using the 3D WS b-SSFP sequence is demonstrated in Figure 5.6 (a). The corresponding histogram, and the curve fitting result based on the above fat distribution model are illustrated in Figure 5.6 (b). As has been validated earlier, water signal is effectively suppressed using WS b-SSFP, and the corresponding signal is close to the noise level centered at zero. Full-voxel fat signal distribution agrees well with a Gaussian-shape peak. Partial-voxel fat signal is between fat peak signal and zero, and a uniform distribution is obtained. This is consistent with the previous uniform distribution assumption for partial-volume fat voxels.

(a)   (b)
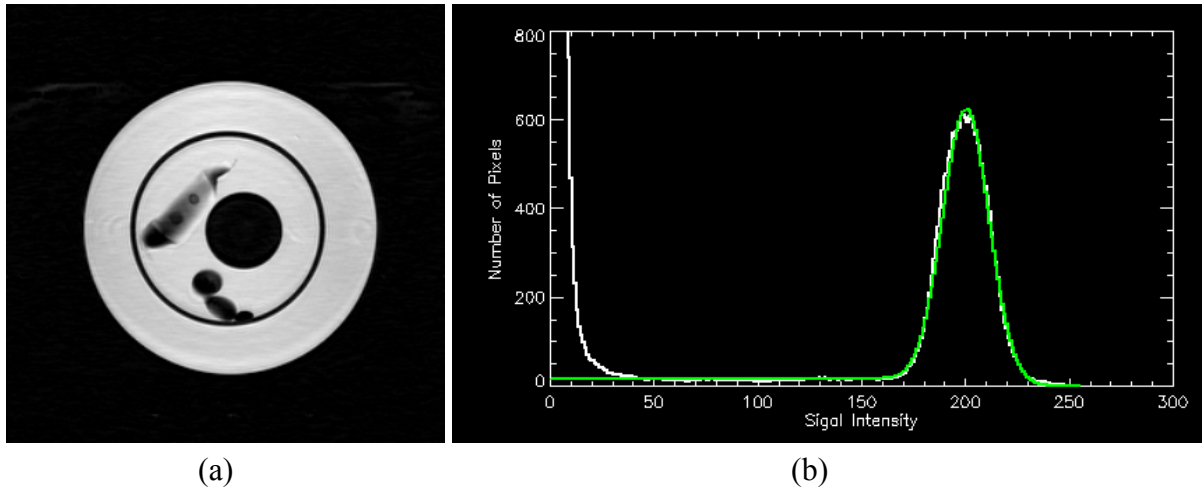
Figure 5.6 Representative phantom image and its histogram. The image in (a) was obtained using 3D WS b-SSFP sequence on the human abdomen phantom. In the histogram plot (b), the white curve represents the histogram of the image, and the green curve represents the result of curve fitting.

To demonstrate the distribution of fat pixels in relation to the signal intensities, intensity-segmented images were generated from the same phantom image in Figure 5.6 (a). These images, with the corresponding signal intensity regions, are shown in Figure 5.7. As expected, low signal voxels in Figure 5.7 (a) mainly correspond to air and suppressed water, high signal voxels in Figure 5.7 (c) correspond to bulk oil, and intermediate signal voxels in Figure 5.7 (b) are partial-volume fat voxels distributed at the interface of bulk oil.
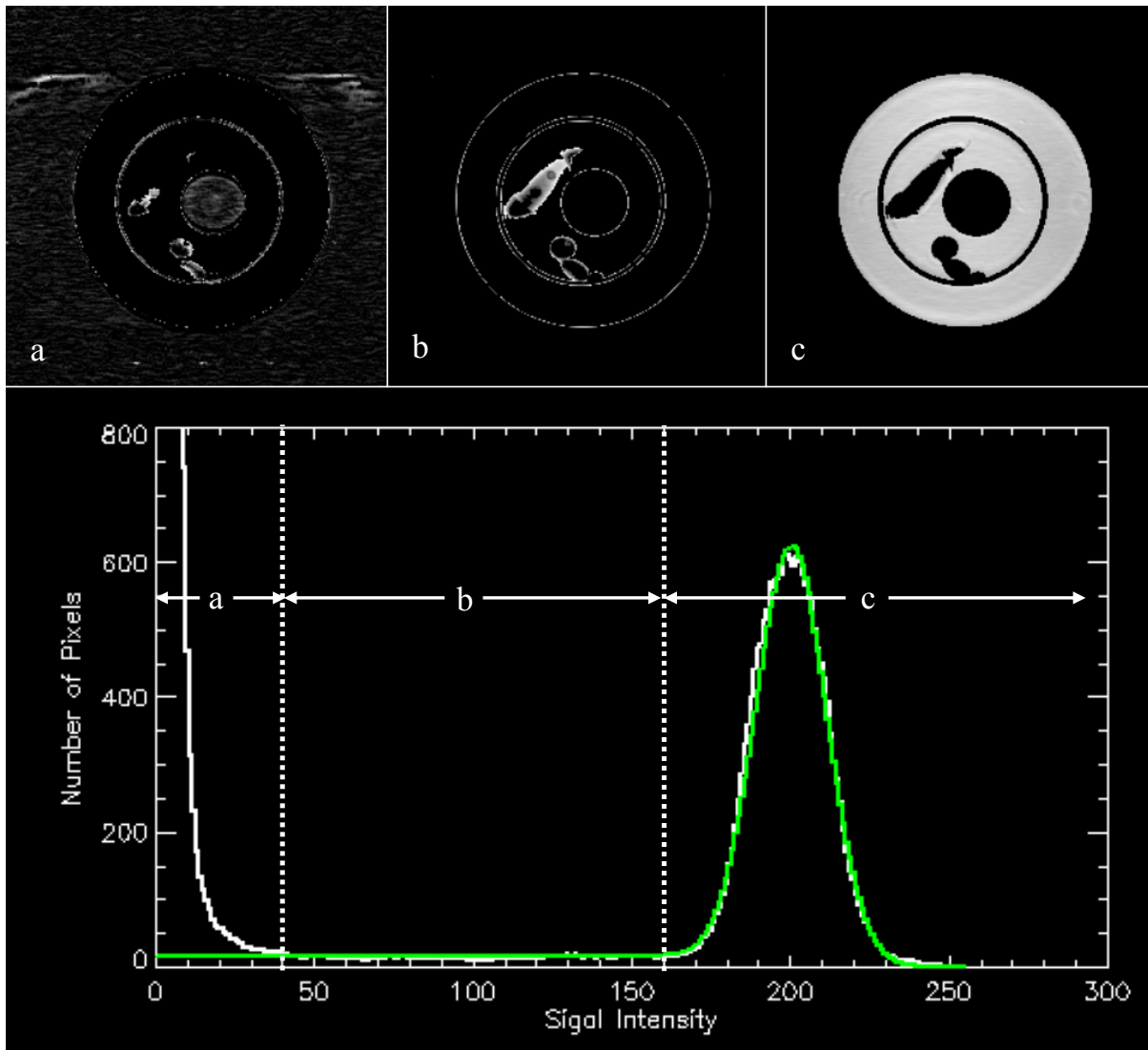
Figure 5.7 Segmented phantom fat (oil) images and the histogram. (a) The resultant image with signal intensity between 0 and 40, corresponding to noise, image artifacts, and voxels with small ratio of fat. (b) The resultant image with signal intensity between 41 and 160, mainly corresponding to moderate partial volume fat voxels. It is obvious that these voxels are mainly located at the boundary of tissue. (c) The resultant image with signal intensity between 161 and 255 (normalized maximum), corresponding mainly to full volume fat voxels, and voxels with large partial volume of fat. The lower chart shows the image histogram and the signal range corresponding to each image. The theoretical curve fit (green) is also shown. The signal threshold is thus determined to be 101 to best separate fat- and water- pixels.

The phantom oil volume measurement results using two different threshold methods are shown in Table 5-1. It is shown that the two processing methods resulted in significantly different accuracies on phantom oil volume estimation. The method using simple full-volume voxel number counting (Th_f) leads to a mean under-estimation of 10.8% for internal oil volume, and 4.8% for external oil volume measurement. The fat quantification method proposed herein which considered both full- and partial-volume fat (Th_{fp}) generated much closer estimation of oil volumes. The mean deviations of internal and external oil volumes are only 0.1% and 2.6%, respectively. The relatively higher over-estimation (2.6%) for external oil volume is most likely due to B_0 inhomogeneity and gradient nonlinearity, since a large 3D volume ($27 \times 27 \times 20$ cm^3) was included in the same scan without table motion.

Table 5-1 Phantom Oil Volume Measurement Results Using Two Methods

Repeat #	Internal		External		Total	
	Th_f	Th_{pf}	Th_f	Th_{pf}	Th_{full}	Th_{pf}
1	89.6	100.0	95.4	102.5	93.4	101.6
2	88.7	100.0	94.9	102.4	92.8	101.6
3	89.7	99.2	95.0	102.6	93.3	101.5
4	89.0	100.0	95.3	102.6	93.2	101.7
5	89.7	100.2	95.3	102.4	93.4	101.7
6	88.4	101.0	95.4	103.0	93.1	102.3
Mean	89.2	100.1	95.2	102.6	93.2	101.7
SD	0.5	0.6	0.2	0.2	0.2	0.3
P	<0.0001		<0.0001		<0.0001	

It is clearly demonstrated that partial-voxel oil volume comprises a significant portion to the total oil volume, and considerable volume under-estimation will be introduced if this effect is overlooked. For human abdominal fat quantification, it is obvious that this effect is even more significant due to the more complicated anatomic structure, much larger voxel size, and severe motion-induced signal averaging.

5.5 Human Study

5.5.1 Materials and Methods

In the human study, six healthy subjects (four males, and two females) were scanned at the L2-L3 level, using a similar WS b-SSFP fat imaging sequence as described early in Chapter 4. However, higher spatial resolution images were acquired instead to achieve more accurate fat quantification. The measured matrix size was 400×400 reconstructed to 512×512 for the resultant image, and slice thickness was 3 mm. Other parameters included: TR/TE/FA = 3.6 ms/1.36 ms/40°, TFE factor = 200. The scan duration was 17 seconds, and eight images were acquired with expired breath-hold. Only the middle four slices (referred to as slice 1 ~ 4) were used for data processing. To simulate partial volume effect, images with 6 mm-thick, and 12 mm-thick slice scan datasets were reconstructed from the original four slices. The two 6 mm-thick slices were generated by averaging slice 1, 2, and by averaging slice 3, 4. The 12 mm-thick slice scan dataset had only one image, which was generated by averaging all four 3 mm-thick slices. The reason to simulate partial volume slices instead of performing extra scans is to avoid possible motion (due to bulk, respiratory, and peristaltic motion) induced true fat volume variations between several different scans. Since water signal is effectively suppressed in WS b-SSFP (as shown in Chapter 4), no destructive fat-water signal addition effect is expected. The simple averaging method therefore should lead to images which are close to images generated by independent scans with thicker slices.

Fat quantification for each image (4 slices for 3 mm-thick, 2 for 6 mm-thick, and 1 for 12 mm-thick) was then performed using the same method as in the phantom study. The resultant total fat for the 12 mm-thick abdomen region in each data group was calculated by summing up the area of fat of each slice times the corresponding slice thickness. Fat quantification results on images of different slice thicknesses, and with different post-processing methods were compared to investigate the repeatability of the two fat quantification methods.

5.5.2 Results

To demonstrate the distribution of fat pixels in relation to the obtained signal intensities, intensity-segmented images were generated from a normal resolution ($256 \times 256 \times 10$ mm^3) image as shown in Figure 5.8. The lower histogram plot shows the corresponding signal intensity region for each separated image. As in the phantom results (see Figure 5.7), low signal voxels in Figure 5.8 (a) mainly correspond to air and suppressed water, high signal voxels in Figure 5.8 (c) correspond to bulk fat, and intermediate signal voxels Figure 5.8 (b) are partial-volume fat voxels distributed at the interface of bulk fat.

The representative original images with high spatial-resolution from a volunteer, and the reconstructed images with lower-resolution, are shown in Figure 5.9. It is obvious that the original images suffer much less from blurring and partial-volume effects compared with the reconstructed, thicker slices, although background noise is relatively higher.

The fat quantification results using the two methods on images with different resolution are shown in Table 5-2. As expected, the Th$_f$ method provided much lower mean fat volumes compared with Th$_{fp}$ method, for both IAF and SAF, and for images with different slice thicknesses. The under-estimation rises as slice thickness increases for both IAF and SAF. As expected, IAF quantification is more influenced by partial-volume effect, and the difference reaches -27.5% with slice thickness = 12 mm.

Figure 5.10 demonstrates the intra-subject IAF quantification variations on images with different slice thicknesses for the Th$_f$ and Th$_{fp}$ quantification methods. Generally, measured IAF volumes are lower if thicker slices are used for Th$_f$ method, but much more consistent fat quantification can be achieved using Th$_{fp}$ method. Therefore, the new processing method is robust even when spatial resolution of an image is somewhat reduced.
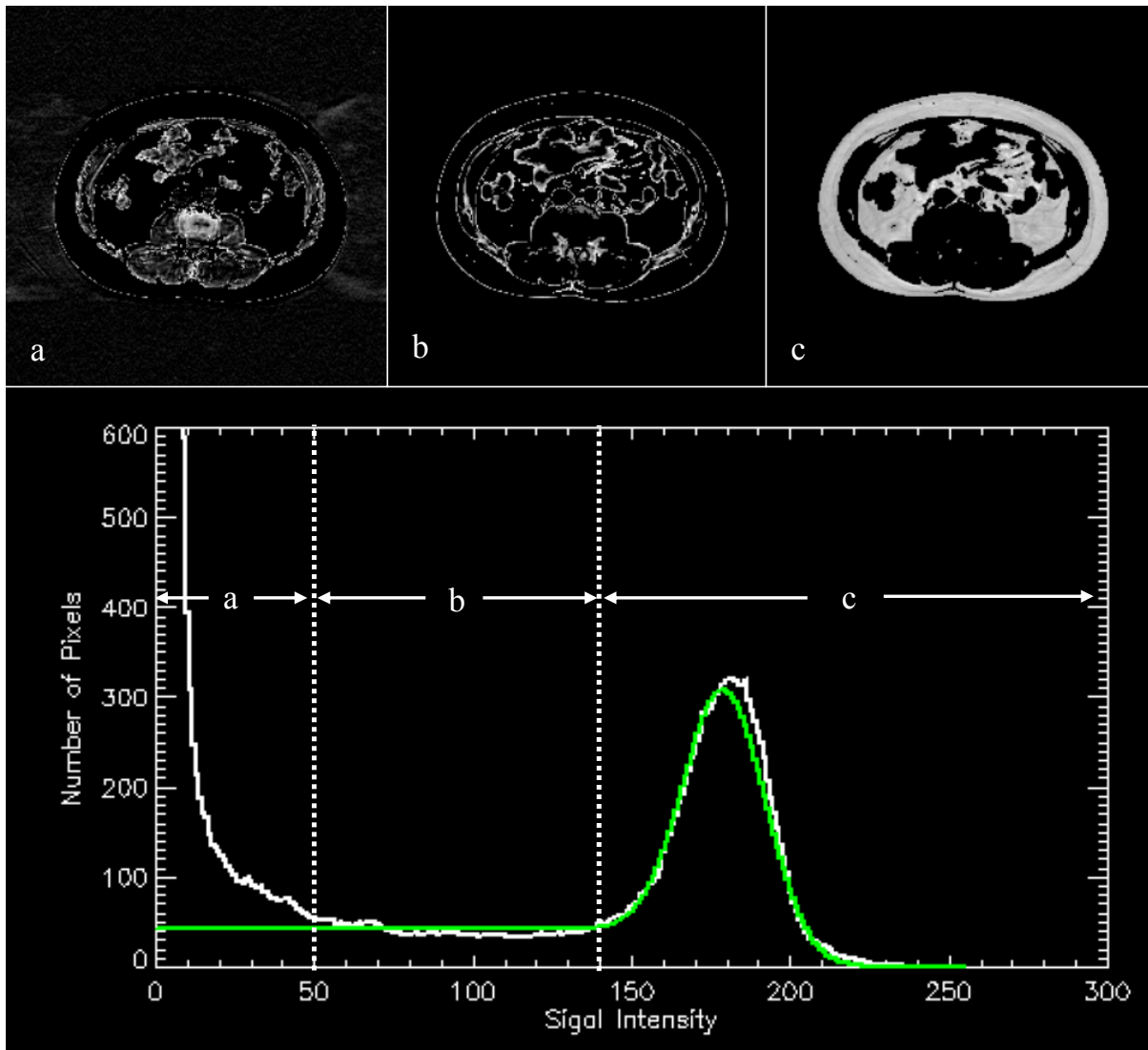
Figure 5.8 Representative human abdominal fat image histogram analysis results. (a) The resultant image with signal intensity between 0 and 50, corresponding to noise, image artifacts, and voxels with small ratio of fat. (b) The resultant image with signal intensity between 51 and 140, mainly corresponding to moderate partial volume fat voxels. It is obvious that those voxels are mainly located at the boundary of tissue. (c) The resultant image with signal intensity between 141 and 255 (normalized maximum), corresponding mainly to full volume fat voxels, and voxels with large partial volume of fat. The lower chart shows the image histogram and the signal range corresponding to each image. The theoretical curve fit (green, or gray on black/white paper) is also shown. The signal threshold is determined to be 90 to best quantify both full- and partial-fat volume.
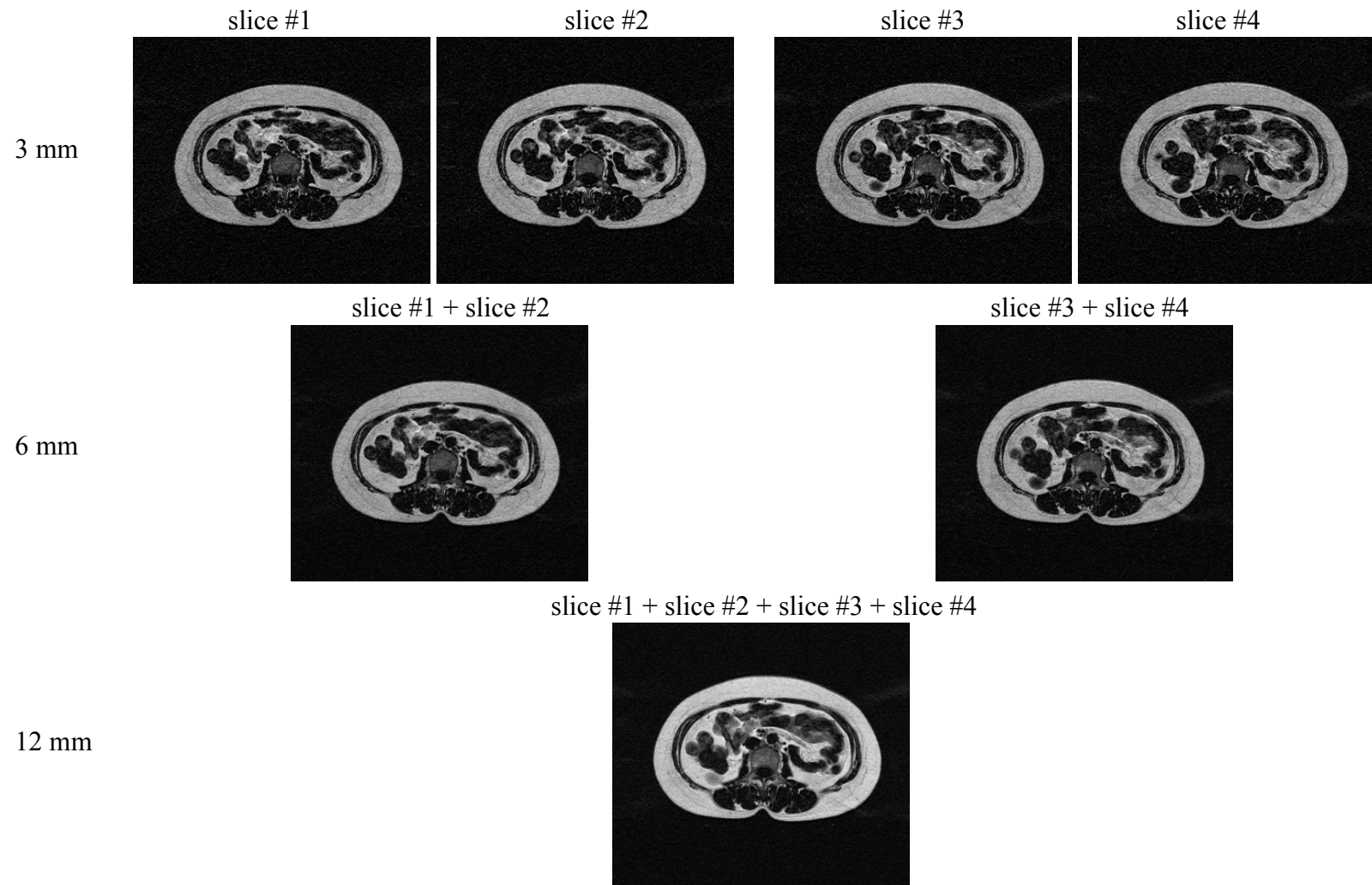
Figure 5.9 Original and reconstructed images for partial volume analyses. The four slices in the first row are the original high spatial resolution images, and the second and third row images are reconstructed from the four images to simulated lower resolution images with slice thicknesses of 6 mm and 12 mm.

Table 5-2 Human Abdominal Fat Quantification Results Using Two Threshold Methods (in cm^3)

Subject #	thickness = 3 mm				thickness = 6 mm				thickness = 12 mm			
	IAF		SAF		IAF		SAF		IAF		SAF	
	Th$_f$	Th$_{fp}$	Th$_f$	Th$_{fp}$	Th$_f$	Th$_{fp}$	Th$_f$	Th$_{fp}$	Th$_f$	Th$_{fp}$	Th$_f$	Th$_{fp}$
1	56	82.7	198.7	212.3	47.3	79.4	195	212.4	37.8	76	192.3	212.8
2	107.9	141.7	191.8	208.5	101.1	140.1	190.2	208	94.7	143.1	192.7	207.8
3	128.3	139.2	145	152.1	123.1	139.6	142	152.6	122.9	142.5	142.7	153.9
4	174.7	209	277.1	291.6	170.8	207.2	277.7	292	151.7	207.5	266.5	292.5
5	143.6	174.5	238.7	251	137.7	169.4	237.3	250.9	128.9	172.8	228.4	256.4
6	94.9	115.4	120.5	131.7	90.7	113.8	120.2	131.6	85.1	115	119.1	132.3
Mean	117.6	143.8	195.3	207.9	111.8	141.6	193.7	207.9	103.5	142.8	190.3	209.3
Diff* (%)	-18.2%		-6.0%		-21.0%		-6.8%		-27.5%		-9.1%	

*: The difference between the two mean results, using the corresponding Th$_{fp}$ result as the reference.
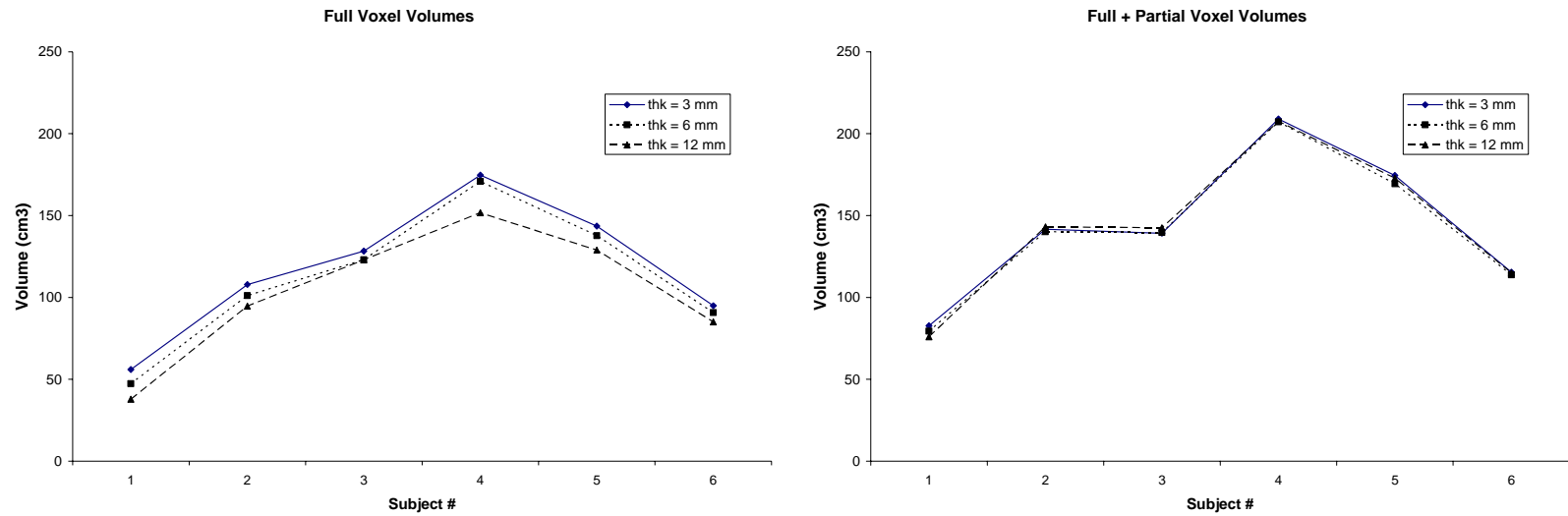
Figure 5.10 Intra-subject IAF variations of the two quantification methods. Only IAF results on different slice thickness images are shown. Full-voxel fat quantification (Th_f method) shows significant inconsistency for fat quantified from images with different slice thicknesses, while the results are more consistent if both full- and partial-fat-voxels are considered (Th_{fp} method).

5.6 Discussion

Due to the lower spatial resolution of MRI compared to CT (56), abdominal fat quantification using traditional full-volume fat voxel-only methods are subject to considerable systematic error. The simple fat distribution model includes fat from both full- and partial-volume fat voxels; therefore pixel signal distribution can be correlated with the fat volume based on an image histogram analysis. Fat quantification using this method can be much easier, and more accurate, compared with the traditional methods where only full-volume fat pixels are considered. The accuracy of this method is validated in a phantom study. In a human study, the traditional method shows much lower fat volume compared with the new method, particularly for IAF. In addition, fat quantification using the new method on images with different slice thicknesses is much more consistent compared with that obtained using the traditional method. These results are most easily explained by the insensitivity to partial-volume effects of the new method.

Although partial-volume fat contribution is considered in the new model, truncation artifact (Gibbs effect) due to the limited in-plane spatial resolution is not considered in the fat quantification (57). Truncation artifacts will generally introduce slight over-estimation of fat volume. However, in the human study, in-plane resolutions were kept the same for all three slice thicknesses. It therefore could not be the reason for differences of the quantification methods.

Another advantage of the new fat quantification method is that it is less sensitive to imaging noise. This is easily explained by the fact that fat quantification is not dependent on the standard deviation of the Gaussian kernel (σ) used in the curve fitting (see Figure 5.5b, and Equation 5.3), as long as the fat peak and the noise peak are separated.

In conclusion, the novel fat quantification method has been validated to offer the following benefits: 1) fat quantification is much more accurate compared with the traditional methods; 2) fat quantification is fast; 3) fat measurements suffer much less from variation due to spatial resolution changes. The improved fat quantification method can thus lead to a much easier and more accurate monitoring of human body fat distribution. The method is

also significant for clinical trial of new drugs to study the fat redistribution under pharmacological influence. Due to the greatly improved fat measurement accuracy and reduced measurement variation, much less subjects can be recruited and much less measurements can be performed to achieve a certain statistical significance. Therefore, clinical trial of a new drug can be finished with greatly reduced expenses and time.

5.7 Semi-automated Fat Quantification Software: Wafter

Traditional post-processing methods based on manual contour drawing on original MR images for fat quantification are laborious and subject to severe measurement deviations. However, rapid and reliable fat quantification using computer automatic or semi-automatic programs can be used on high quality images with high SNR_{fat} and $CNR_{fat-water}$ obtained using WS b-SSFP.

Computer software dedicated to fast fat quantification based on IDL (Interactive Data Language, Research Systems, Boulder, CO) was developed. The user interface of the software is shown in Figure 5.11. Upon loading the images to be processed, automated curve-fitting is performed based on the signal histogram for each slice, and an optimal lower threshold is determined based on the curve fitting. The histogram typically shows two peaks of gray values belonging to the resonances of water and fat. Since water signal is usually effectively suppressed on WS b-SSFP images, water peak locates close to zero. The optimal lower threshold estimated by Wafter is close to half of the value corresponding to fat peak. The operator will evaluate the adequateness of the curve fitting and the lower threshold for the separation of fat voxels. The fat- and water-only images will be updated interactively if lower threshold is changed by the operator. The fat-only image is generated by setting pixels with signal level less than the lower threshold to zero and only pixels with higher signal is shown in the resultant image. Once the lower threshold is set, the fat-only image can be exported to the ROI tool for regional fat quantification. The user interface for ROI contour drawing is shown in Figure 5.12 (left-hand). Rectangular, oval, free-hand, and polygon ROIs can be defined using this tool. The software will automatically calculate the number of fat

pixels (or number of non-zero pixels) and the corresponding fat volume enclosed in each defined ROI. Usually several ROIs have to be defined to obtain total, and intraabdominal fat volume. The calculated results for all defined ROIs are shown in Figure 5.12 (right-hand), and can be easily saved to a default or user-defined text file by clicking on the "Save" button. The time required for the processing of each image is typically $10 \sim 30$ seconds.

Interested readers are encouraged to turn to Wafter online help for details of how to use the software.
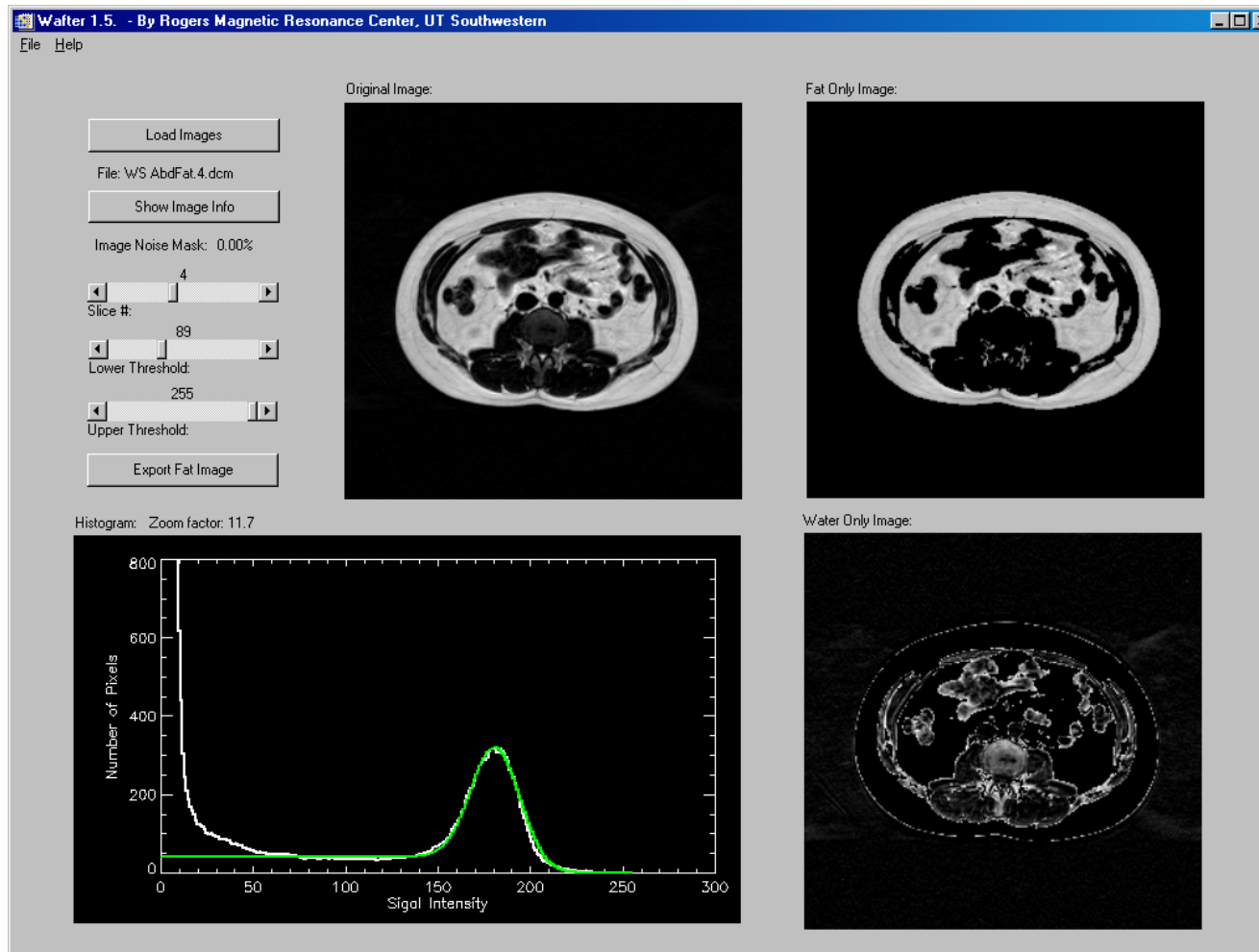
Figure 5.11 Main user-interface of Wafter. After loading the image, the image histogram is automatically calculated (lower-left chart). Curve-fitting is also performed to generate an estimated fat signal distribution (green curve). The lower threshold is therefore calculated based on the curve fitting, and a fat-only image is generated automatically (upper-right image). The operator can also adjust the lower threshold to best differentiate non-fat and fat pixels if needed. Corresponding fat- and water-only images will be updated if lower threshold is changed.

100
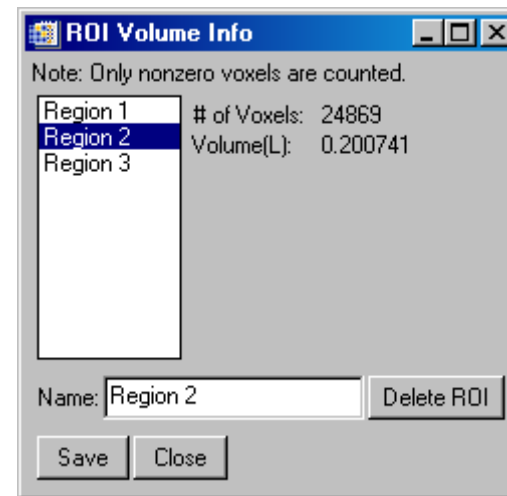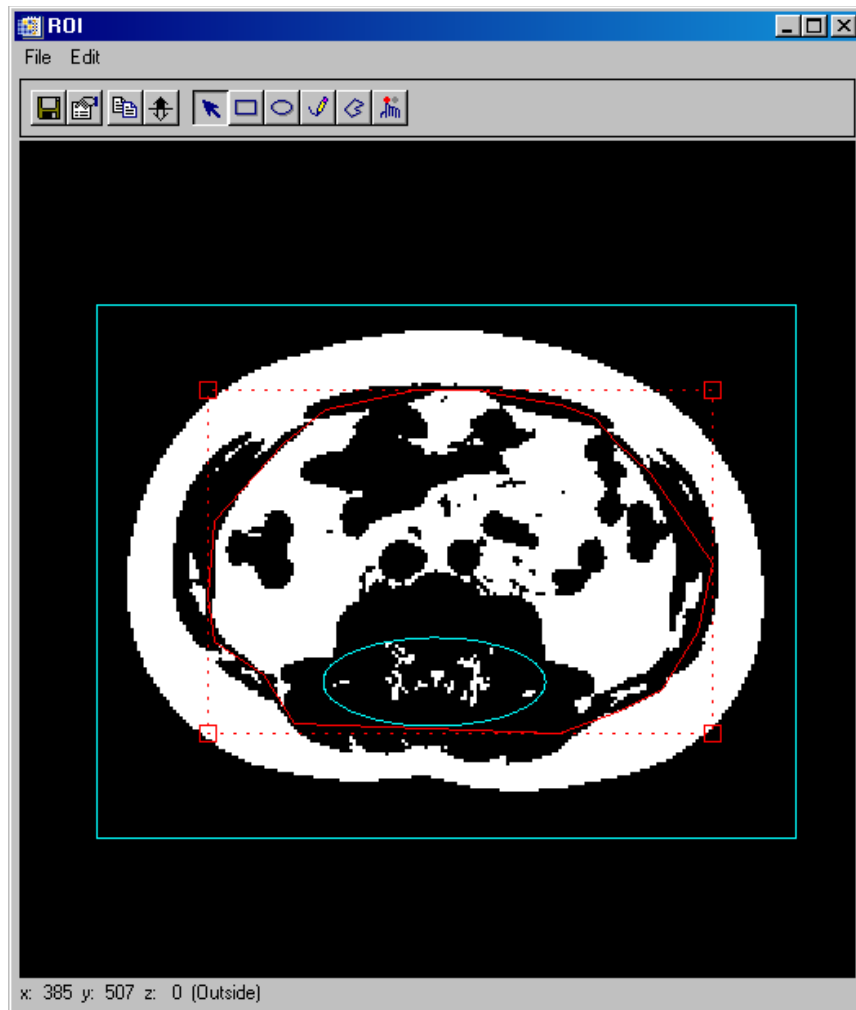
Figure 5.12 ROI tool user-interface and ROI volume information window. User-defined ROIs can be drawn on the binary fat-only image, and number of pixels, as well as the fat volume enclosed by each ROI can then be automatically calculated. Fat volumes for each ROI can be saved to a default or user-defined text file by click "Save" button on the "ROI volume info" window.

Chapter 6 Rapid Fat-Suppressed Imaging

6.1 Introduction

The generation of fat suppressed MR images with high spatial and temporal resolution is very important for many clinical applications, especially so for contrast-enhanced dynamic studies. In dynamic studies of the breast, for example, it is critical to obtain full breast coverage with fat suppressed, high temporal and spatial resolution images in order to differentiate benign from malignant lesions (58,59). Fat suppression reduces chemical shift artifacts, and improves lesion conspicuity. The enhanced contrast of lesion-to-parenchyma and lesion-to-fat can improve the evaluation of tumor extent and multiplicity.

With the development of modern MR technology, short TR, three-dimensional (3D) gradient echo imaging techniques have gained popularity due to their ability to obtain high quality images in short acquisition times. However, fast short TR gradient echo imaging with adequate fat suppression is still a subject of intensive investigation due to the limitations of current available techniques.

6.2 Traditional Fat-Suppressed Imaging Approaches

There are various approaches available to achieve fat-suppressed images (60,61). Most fat suppression techniques fall into two broad categories. In the first category, fat suppression is applied during data acquisition, whereas in the second category fat signal is not suppressed during imaging; instead, water-fat separation is accomplished as a post-processing step. The latter approach, examples of which include two- or multi-point Dixon's method (5,6), usually requires either a long repetition time or multiple excitations. It also suffers from the fact that dynamic range for water signal is not improved since the unsuppressed fat signal is usually high in most T_1-, T_2- and proton density-weighted images. Performing fat suppression during imaging, which can be regarded as "true" (or "active") fat suppression, is usually desirable,

especially for clinical dynamic contrast enhancement studies, since subtle changes in lean-tissue intensity can be readily detected.

It is well known that traditional inversion recovery approaches to fat suppression are slow, and usually offer poor SNR for lean-tissues. Furthermore, the use of an inversion recovery pulse suppresses all tissues with short T_1 and is therefore not robust for contrast-enhanced studies. With the wide availability of high field magnets ($\geq$ 1.5 T), spectral-selective approaches to fat suppression have gained in popularity. Since water and fat resonant frequency difference is proportional to the main magnetic field (B_0), spectral selective excitation gains in robustness with higher B_0 (61). Two widely used fast fat suppression techniques are fat pre-saturation using spectral partial inversion recovery (SPIR) (62), and spatial-spectral excitation (SSE) (10) for water-selective imaging (59). SPIR is a traditional approach, technically easy to implement and it is used in a variety of clinical applications. To obtain a fat suppressed signal, the frequency of the spectrally selective SPIR radiofrequency (RF) prepulse is adjusted to excite the lipid spins to the transverse plane, which are then dephased by a spoiling gradient, thus leaving only water spins available for imaging. Although fat suppression is usually quite effective, the SPIR prepulse and the spoiling gradient will generally increase TR substantially, by 10 ~ 20 ms in fast field echo (FFE, or SPGR, FLASH) pulse sequences (TR here is defined as excitation-to-excitation duration). Shorter TR can be achieved using SSE instead, which obviates the time-consuming spectral fat pre-saturation RF pulse and the spoiler in each TR. Spatial-spectral selective excitation can be implemented by employing a train of RF excitation sub-pulses in conjunction with slice- (2D) or volume- (3D) selective magnetic field gradients. A binomial SSE pulse train consisting of the combination of several conventional sinc-modulated RF pulses, and short train duration, can be achieved. The spectral-selective capability is highly dependent on the order of the binomial RF pulses (or the pulse train length). A higher-order binomial RF train excitation is more spectrally selective and gives better fat suppression, but the pulse train duration is long, which increases both TR and TE significantly. A third-order binomial (e.g., 1-3-3-1) composite excitation pulse may take more than 12 ms (63), thus

limiting the shortest achievable TR and TE. A first-order binomial excitation RF pulse (e.g., 1-1) is short, but fat suppression is much less effective.

A more time-efficient fat suppression technique utilizes fat pre-saturated turbo field echo (TFE, or fast SPGR, turboFLASH), wherein one SPIR pulse is followed by multiple excitations, and several phase encoding acquisitions (echo train) are obtained. This decreases the shortest achievable TR and scan duration, as the number of SPIR pulses can be considerably reduced if a long echo train length (ETL) is used. However, TFE shot duration is limited due to the short longitudinal relaxation of fat (200 ~ 280 ms) and images will be prone to contamination by fat signal as ETL increases. Thus, TFE shot duration must be typically less than half of fat T_1 to avoid severe artifacts, such as ghosting and blurring.

6.3 Novel Rapid Fat Suppression Strategy

6.3.1 Energy in K_y-f Joint Space

Short TR pulse sequences usually involve the acquisition of one phase-encoding profile in Cartesian coordinates in 2D or 3D k-space per excitation. Thus k-space is filled once all required phase-encoding gradient combinations are applied. The resultant images are obtained from the k-space acquired data via Fourier transform. As the order of performing different phase-encoding acquisitions can be arranged in multiple ways, different view-orders can be used, possibly leading to different tissue contrast in a fat suppressed sequence (64,65). On the other hand, fat suppression efficacy using spectrally selective methods is also greatly dependent on the spectral signal energy distribution of the imaged region. To examine the influence of both view-order and spectral energy distribution on the effectiveness of fat suppression for different sequences, it might be useful to study the energy distribution in a k_y-f joint space as shown in Figure 6.1. The k_y-axis represents k-space data acquisition position in the phase encoding direction, and the f-axis represents resonant frequencies within the hydrogen pool in the imaged region. In the f-axis, f_0 stands for the water on-

resonant frequency, and f_{fat} is that of fat ($f_0 - f_{fat}$ is about 220 Hz at 1.5T, the field strength of the MR scanner used in this work). To simplify the analysis, we assume the bandwidth of both water and fat off-resonances is limited to ($f_0 - f_{fat}$), so that water and fat spins can be spectrally separated.

Since the energy of the MRI signal is concentrated in the center of k-space (2,66), lower phase-encoding (e.g., k_y close to 0) profiles contain most MRI signal energy compared to that of higher k_y profiles. Since this is generally true for both fat and water signals, each of them can be depicted by a single peak energy curve along k_y direction with the center at $k_y = 0$. This signal distribution property is particularly true for high resolution acquisitions. Although it is difficult to find a general analytical expression of the spectral distribution for a 2D or 3D imaged region, the spectrum usually has two isolated resonance peaks corresponding to water and fat spins (signal from other chemical species are negligible), if a good shimming is achieved. Each peak has a line-spread width which is mostly influenced by B_0 homogeneity and tissue susceptibility in the imaged region. Therefore, the energy curve along f direction can be described by a two-peak curve shown along f direction. The overall energy distribution of either water or fat in k_y-f space can be estimated as the energy distribution along k_y weighted by the corresponding spectral intensity along f, as portrayed by the two dimensional surface plot in Figure 6.1. It is revealed that both water and fat signal energy is highly concentrated in k_y-f space with most of the energy gathering at (0, f_0) and (0, f_{fat}), respectively. Understanding of this unique signal energy distribution might be beneficial for the design of time-efficient fat suppression strategies.
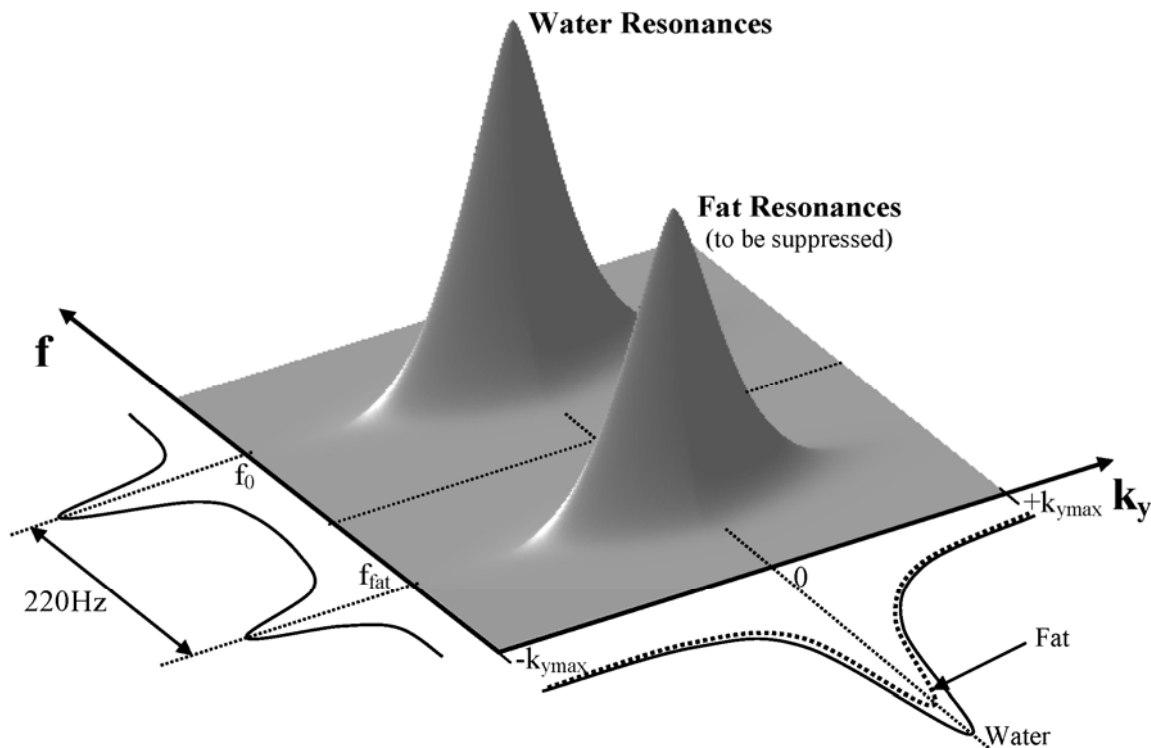
Figure 6.1 Typical MRI signal energy distribution in k_y-f space. It is shown in the joint k_y-f space that MRI signal energy concentrates only on two isolated peaks corresponding to water and fat resonances. The centers of both peaks have $k_y = 0$, and the distance between them along f is about 220 Hz for a 1.5T scanner.

6.3.2 Rapid Fat Suppression Strategies

Rapid fat suppression strategies using spectrally selective methods can be easily explained in k_y-f space. Ideally, to obtain a water-only image, signal of all lipid spins must be suppressed for every k-space profile, as shown in Figure 6.2a (Type A). Theoretically, this can achieve a complete fat suppression in the resultant image. SPIR FFE and high-order binomial SSE FFE sequences are examples of this approach. The drawback of this approach, however, is that it is time-consuming, as discussed earlier. It is well known that image contrast is mostly determined by central portion of k-space. Taking advantage of this observation, a more time-efficient approach to fat suppression is shown in Figure 6.2b (Type

B), wherein only the central k-space profiles are fat-suppressed for all lipid spins. Fat pre-saturated TFE sequences such as SPIR TFE are examples of this approach. This approach has a much improved fat suppression efficiency, however, the resultant image is easily contaminated by ghosting and blurring artifacts induced by fat longitudinal relaxation that occurs during the echo train. As fat T_1 is short, long ETL is not easily achievable without compromising image quality. A short-TR, low-order SSE FFE water-selective sequence (e. g. using 1-1 binomial RF excitations) is represented in Figure 6.2c (Type C), wherein narrowband fat suppression is performed for every acquisition. Since only on-resonant lipid spins are effectively suppressed, this approach is more sensitive to B_0 inhomogeneity. Although this type of fat suppression is also time-efficient, poor off-resonant fat suppression in the resulting images hinders wider clinical applications.

Neither of the two efficient suppression approaches (Type B, C) seems to be clinically satisfactory. It is postulated that the Type B strategy can be improved if higher k-space data are acquired with fat suppression, and that the Type C approach is not satisfactory mostly due to inadequate fat suppression in central parts of k-space. Based on this assumption, a novel fat suppression strategy can be proposed. This strategy combines the two traditional, rapid fat suppression approaches together as shown in Figure 6.2d (Type D). It therefore achieves fat suppression on all fat resonant frequencies for central k-space profiles, and achieves sustained fat suppression for on-resonant lipid spins at higher k-space profiles. This approach might greatly lengthen the ETL that can be used compared to that obtained using Type B, and also will be much less sensitive to B_0 inhomogeneity compared with that of Type C.
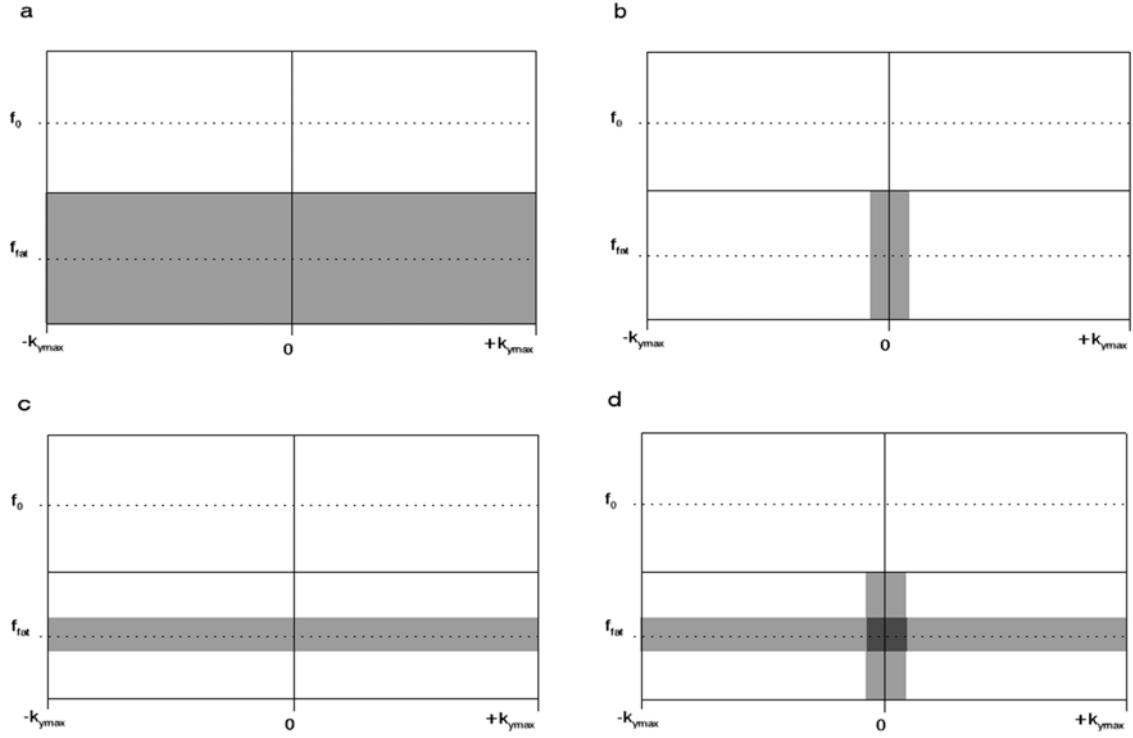
Figure 6.2 Schematic plots to illustrate several approaches to fat suppression. (a) Ideal fat suppression is achieved for both on- and off-resonant fat signals (vertical axis) for all phase encoding profiles (horizontal axis). (b) Efficient fat suppression can be reached by applying fat suppression for all fat spins, but only on the central k-space profiles that largely determine the image contrast (such as fat pre-saturated SPIR TFE sequences). (c) Efficient, but less effective, fat suppression is obtained through sustained suppression of on-resonant fat spins for all k-space profiles (such as low-order water-selective SSE). (d) The proposed fat suppression strategy combines fat suppression of all fat spins on central k-space profiles with sustained on-resonant fat signal suppression.

6.3.2 SPIR-SSE Pulse Sequence

The first pulse sequence implementation of this novel fat suppression strategy is shown in Figure 6.3. It is based on a traditional 3D RF spoiled TFE sequence with magnetization preparation (fat pre-saturation using SPIR). All RF excitations (α flip angles) are replaced by two $\alpha/2$ spatial-spectral excitation pulses, with an inter-pulse delay of 2.3 ms (SSE 1-1). This sequence is referred to as SPIR-SSE TFE in the rest of this chapter.
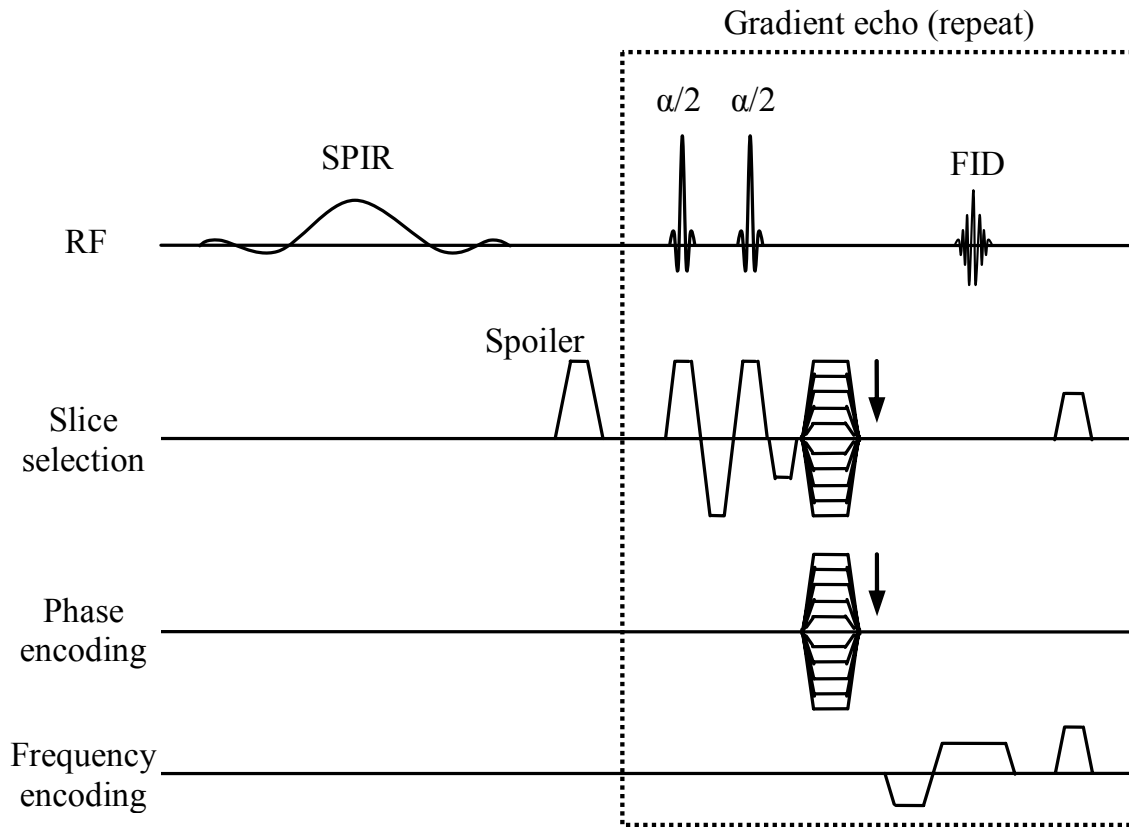
Figure 6.3 Schematic of the SPIR-SSE TFE pulse sequence. It is based on a traditional 3D RF spoiled TFE sequence. The fat selective SPIR pulse tips fat spins to the transverse plane, and the following spoiler gradient eliminates remaining coherent magnetization before the acquisition echo train. SSE binomial (1-1) RF pulses are employed for sustained water-selective excitation.

6.3.3 Phantom Study: Methods and Results

All imaging experiments were performed on a Philips Intera 1.5 T clinical MR scanner. A standard receive-only quadrature-head coil was employed for phantom studies. A tube (inner diameter: 21 mm, length: 150 mm) filled with vegetable oil was used as the phantom, and care was taken to ensure no air bubbles were introduced. The tube was placed with its longitudinal axis along that of the scanner to reduce susceptibility artifacts. A linear shim gradient (0.1 mT/m) was applied along the longitudinal axis (the readout direction) of the tube to generate a frequency variation along the readout direction so the fat suppression

efficacy could be demonstrated. 50 sagittal slices were imaged using SSE (1-1) FFE, SPIR TFE, and SPIR-SSE TFE sequences as described above. All three sequences were tested in the phantom with TR/TE/flip angle = 12.0 ms/6.0 ms/18°, NEX = 1, and readout bandwidth = 38.3 kHz. Other parameters included: FOV = 20 cm, slice thickness = 4 mm with 2 mm overlap, and matrix size = 256. For both SPIR TFE and SPIR-SSE TFE, a low-high (centric) phase profile ordering was employed. For TFE scans, ETL of 64 and 256 were both tested, resulting in TFE shot durations of 789 ms and 3102 ms, respectively. To minimize scan duration, there was no time delay after one TFE shot before the administration of the SPIR pulse of the next shot. The bandwidth of SPIR pulses was 340 Hz, and the angles were experimentally optimized to be 95°. SPIR central frequency was manually shifted to -280 Hz relative to f_0 so that SPIR would not affect resonances above $(f_0 + f_{fat})/2$ (or f_0 - 110 Hz) which was assumed to be in the water resonant range. To investigate the effect of fat suppression on different k-space profiles, another set of images were obtained after turning on "1DFT test mode" from the scanner user interface, wherein all phase encoding gradients were disabled in the sequences, and Fourier transform was only performed along readout direction. The resultant images obtained in this test mode show information similar to that portrayed in Figure 6.2.

Representative phantom images are shown in Figure 6.4 for each of the five sequences tested. In each case, the center slice from the 3D acquisition has been selected. Both the image obtained in 1DFT test mode (left) and the one in normal imaging mode (right) are shown for each subfigure of (a)-(e). For SSE (1-1) FFE (Figure 6.4a), only a narrow band of on-resonant fat signal is moderately suppressed, due to the poor spectral-selective capability of the first-order binomial (1-1) RF pulses. The two SPIR TFE sequences (Figures 6.4b, c) show strong fat suppression at the center of the tube but suffer from blurring artifacts at the edges for both on- and off-resonant fat spins. The test mode images of the two SPIR-SSE TFE sequences (Figures 6.4d, e, left-hand sub-images) show "cross"-like fat signal suppression which is desired. The fat suppression has been improved considerably (Figures 6.4d, e, right-hand sub-images) compared with that of SSE (1-1) FFE. In addition, fewer

blurring artifacts are seen at the edges of the tube in SPIR-SSE TFE images compared with the SPIR TFE images for both ETL = 64 and 256, especially for on-resonant fat spins.
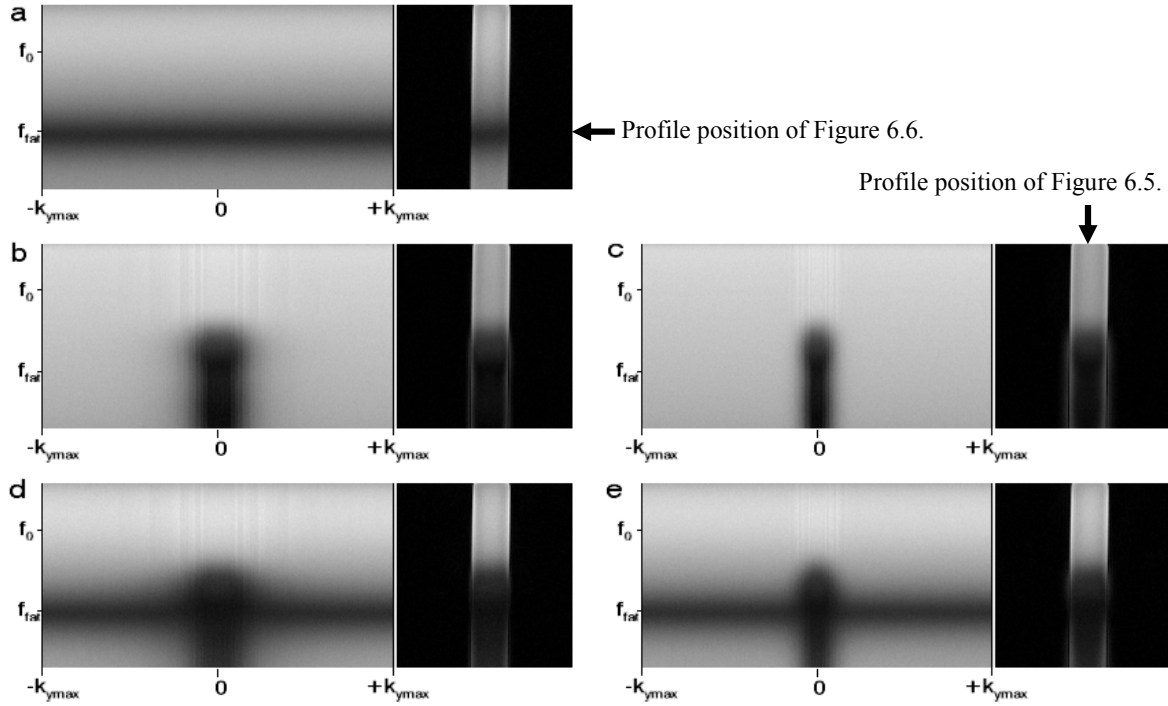
Figure 6.4 Phantom resultant images for different pulses sequences. (a) SSE (1-1) FFE; (b) SPIR TFE with ETL = 64; (c) SPIR TFE with ETL = 256; (d) SPIR-SSE TFE with ETL = 64; (e) SPIR-SSE TFE with ETL = 256. In (a)-(e), the left-hand image is obtained in 1DFT test mode which plots transverse plane magnetization evolution of spins with different resonant frequencies against k-space (obtained without phase-encoding (horizontal) gradients, and with only 1D FT along readout (vertical) direction), and the right-hand image shows the result using a traditional acquisition with all phase-encoding gradients and using 3D FT).

Figure 6.5 and Figure 6.6 show the intensity profiles of the five images through the central vertical line, and through the horizontal line of the phantom at fat resonant frequency, respectively. The line positions are also shown in Figure 6.4. On-resonant water (f_0) signal is normalized to 1 for each profile so the fat signal-to-water signal ratio is clearly revealed. SSE (1-1) FFE is confirmed to offer inferior fat suppression for both on- and off-resonant fat spins. All TFE sequences have strong fat suppression in the center of the tube, as shown in

Figure 6.5. However, the high spatial frequency performance varies significantly as demonstrated in Figure 6.6. Severe edge signal oscillations are obvious for SPIR TFE with both ETL = 64 and 256, and the maximal fat signal reaches 0.53 and 0.43, respectively. The signal oscillation is suppressed strongly in SPIR-SSE TFE (maximal fat signal is 0.13 and 0.16 for ETL = 64 and 256, respectively). The very close performance of SPIR-SSE TFE sequence with different ETL justifies the use of a long ETL such as 256. It is clear from these phantom studies that the new SPIR-SSE TFE sequence with long ETL can achieve significantly improved fat suppression over that obtained with SSE (1-1) -only or SPIR-only approaches.
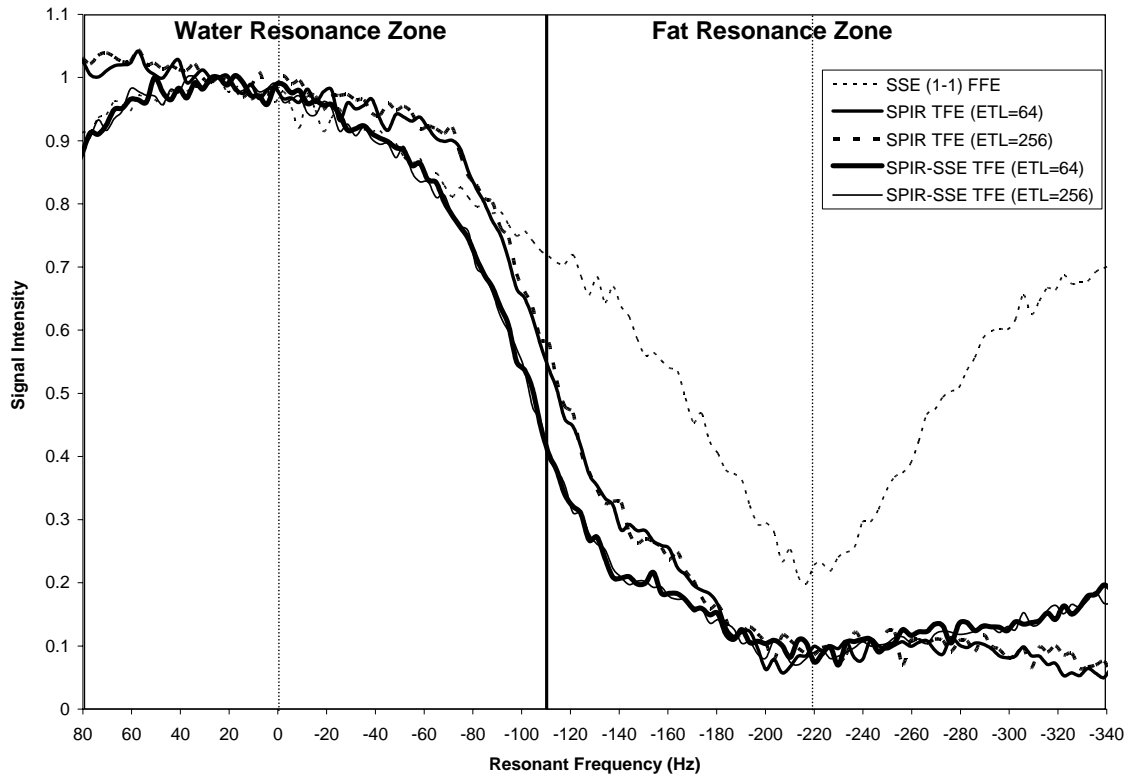
Figure 6.5 Line profile comparison of phantom results. The line position is as shown in Figure 6.4c. The profile demonstrates the fat suppression performance on low spatial frequency for both on- and off-resonant fat spins. Signal is normalized to the water resonance (0 Hz).
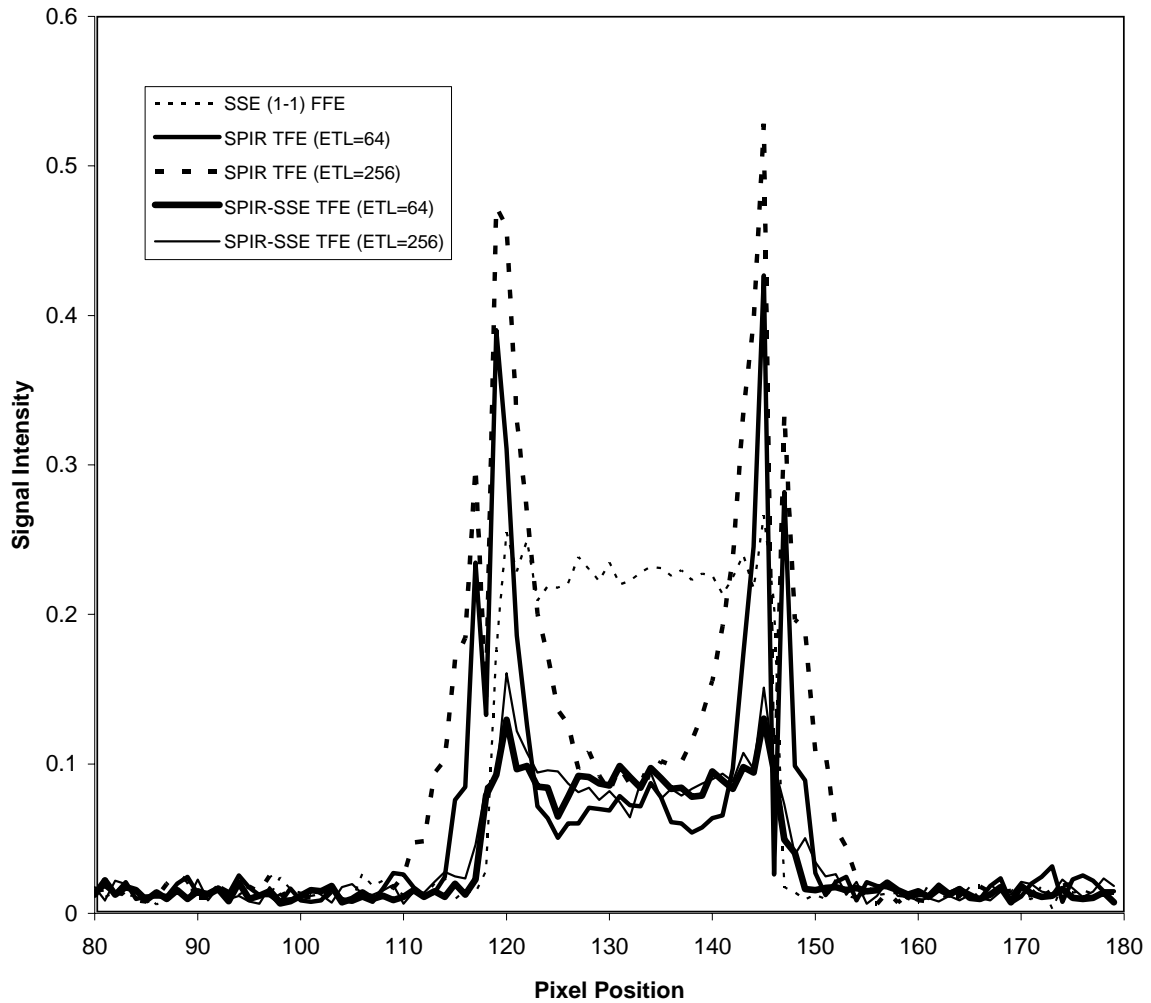
Figure 6.6 Line profile comparison of phantom results. The line position is as shown in Figure 6.4a. The profile demonstrates the fat suppression performance on the high spatial frequency of on-resonant fat spins. Severe edge signal oscillations are obvious for SPIR TFE with both ETL = 64 and 256 were significantly reduced in SPIR-SSE sequences.

6.3.4 Human Study: Methods and Results

To validate the proposed fat suppression methodology *in vivo*, pulse sequences including SPIR-SSE TFE were tested with T_1-weighted breast imaging on a 28-year-old healthy volunteer. Informed consent was obtained from the volunteer prior to scanning. A 4-channel dedicated breast coil was employed. In each sequence tested, the corresponding

113

Ernest angle for fat was used to reduce the influence of differing TR on fat suppression efficacy (2). 75 axial images were obtained on the right breast with free breathing, and the measured slice-thickness was 3 mm with 1.5 mm overlap. All other parameters were the same as in phantom studies. Volume shimming on the interested breast was applied before data acquisition. The 3D SPIR-SSE TFE sequence had an ETL of 256. For comparison, fat suppression using traditional fat saturated FFE with SPIR (TR/TE/FA = 32.0 ms/4.7 ms/28°, referred to as SPIR FFE below), spatial-spectral water selective FFE using third-order (1-3-3-1, referred to as SSE (1-3-3-1) FFE) and first-order (1-1, referred to as SSE (1-1) FFE) binomial RF pulses excitation (TR/TE/FA = 17.0 ms/8.3 ms/21°, and TR/TE/FA = 12.0 ms/6.2 ms/18°, respectively), and fat presaturated with SPIR TFE (9.7 ms/4.8 ms/16°, referred to as SPIR TFE) were also tested. For all sequences with SPIR, experimentally optimized flip angles were employed. In each sequence, the shortest achievable TR and TE were employed to minimize scan duration, and to obtain more T_1 weighting.

Figure 6.7 shows six images, obtained at the same location from the volunteer, acquired with different fat suppression techniques. The images obtained with SSE (1-3-3-1) FFE (Figure 6.7a) have the most effective fat suppression, consistent with the results of previous reports (59,67). However, the resultant images suffer slightly more from motion artifacts along the phase-encoding direction (left-right) compared with other images, most likely due to the longer excitation RF train, and longer TE used. SPIR FFE images also have adequate fat suppression, although the residual background fat signal is slightly higher (Figure 6.7b). Homogeneous fat suppression is achieved over the whole breast without obvious artifacts by SPIR-SSE TFE with ETL = 256 (Figure 6.7c), even though the scan duration is much shorter. Since the TFE shot duration in this sequence is 3203 ms, much longer than fat T_1, this high quality fat suppression demonstrates the effectiveness of sustained fat suppression obtained from the short binomial 1-1 pulses.

Representative results from traditional rapid fat suppression sequences are shown in Figures 6.7d, e, f. Figure 6.7d shows the image obtained with SSE (1-1) FFE. The overall fat suppression is less effective compared with that of SPIR-SSE TFE. Figures 6.7e, f demonstrate the images obtained with SPIR TFE without sustained SSE (1-1). Satisfactory

fat suppression is obtained with ETL = 8 and TFE shot duration of 95 ms, which is less than half of fat T_1. The image, however, suffers from moderate fat signal blurring, which smears the fine structural details of breast parenchyma. This is easily explained by the fact that data acquisition is frequently interrupted by the SPIR pulses, as the ETL is short, and almost all data are acquired in transient periods. The use of a longer ETL is not acceptable either, because most of the k-space profiles are not fat suppressed, and the resultant image is contaminated by the overwhelming fat signal (Figure 6.7f, with ETL = 64, and TFE shot duration = 636 ms).

In consideration of the fat suppression time penalty for each sequence tested, the scan duration of a non-fat-suppressed FFE sequence was used as a reference. The scan durations of all other fat-suppressed sequences relative to the reference scan were calculated and compared. In addition, a fat suppression efficacy factor ζ_{fse} was calculated for each sequence to study fat suppression performance quantitatively. ζ_{fse} is defined as $\zeta_{fse} = S_{fat}/SNR_{fat}$, wherein SNR_{fat} is the SNR of fat, and S_{fat} is the theoretical fat signal *if fat suppression is not performed*, calculated from the Bloch equations using the TR, TE, and flip angle in each sequence. SNR_{fat} was calculated as the mean signal intensity of an ROI on fat, divided by the standard deviation of the background noise measured in an air region. ζ_{fse} analyses indicate that fat suppression using traditional slower fat suppression sequences achieve the highest ζ_{fse} values (1.0 for SSE (1-3-3-1) FFE, and 0.98 for SPIR FFE, respectively. All ζ_{fse} values are normalized to that of SSE (1-3-3-1) FFE). Among the rapid fat suppression sequences, SPIR-SSE TFE with ETL = 256 has a much higher ζ_{fse} = 0.92, compared with those of SSE (1-1) FFE (ζ_{fse} = 0.40), SPIR TFE with ETL = 8 (ζ_{fse} = 0.26) and ETL = 64 (ζ_{fse} = 0.23). The ζ_{fse} results of all sequences tested, together with the scan durations and qualitative descriptions of image artifacts, are summarized in Table 6-1.

a. SSE (1-3-3-1) FFE, 3:30
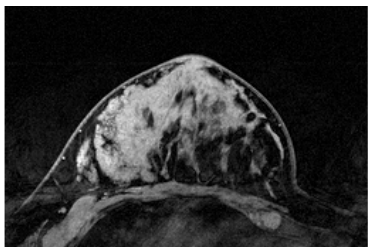
b. SPIR FFE, 6:30
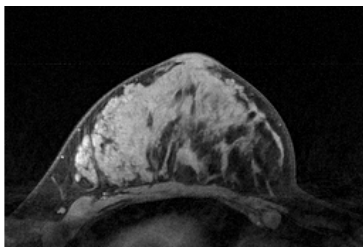
c. SPIR-SSE TFE (ETL=256), 2:34
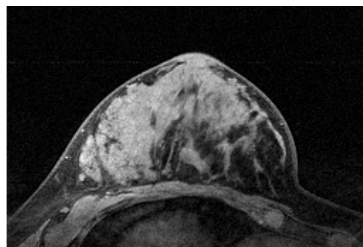
d. SSE (1-1) FFE, 2:33
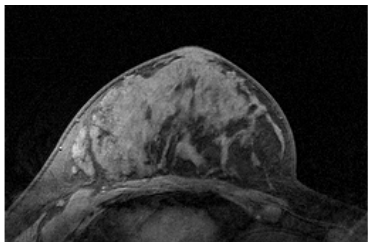
e. SPIR TFE (ETL=8), 2:27
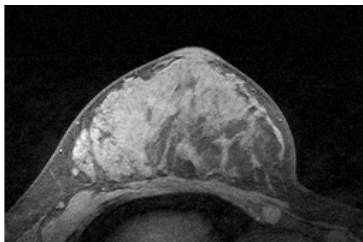
f. SPIR TFE (ETL=64), 2:03
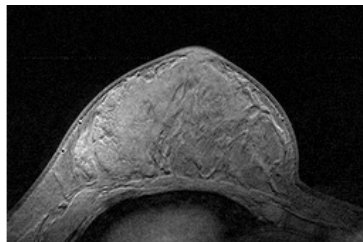
Figure 6.7 In vivo breast images using different pulse sequences. The corresponding sequence and scan duration (in min:sec) are shown above each image. See text or Table 6-1 for TR, TE, and flip angle for each sequence.

Table 6-1 Comparison of Fat Suppression Results of Different Pulse Sequences for Breast Imaging

Sequence	Minimum TR/TE (ms)	Scan duration (min:sec)	Longer than reference (%)	ζ_{fse}[+]	Fat blurring?
FFE*	9.7/4.8	1:59	-	-	-
SSE (1-3-3-1) FFE	17.0/8.5	3:30	76	1.00	No
SPIR FFE	32.0/4.8	6:30	228	0.98	No
SPIR-SSE TFE (ETL=256)	12.0/6.2	2:34	29	0.92	No
SSE (1-1) FFE	12.0/6.2	2:33	29	0.40	No
SPIR TFE (ETL=8)	9.7/4.8	2:27	24	0.26	Moderate
SPIR TFE (ETL=64)	9.7/4.8	2:03	3	0.23	Severe

*: No fat suppression was performed, and it is used here as the reference.

[+]: All ζ_{fse} calculated are normalized to ζ_{fse} of SSE (1-3-3-1) FFE, which gives the best fat suppression efficacy.

6.4 Discussion

As lipids in the human body are usually not involved in pathology or disease, fat suppression during acquisition can minimize chemical shift artifacts and partial volume effects and reduce the possibility of pathology being obscured by the surrounding strong lipid signal. Consistent and reliable fat suppression with minimal acquisition time penalty is strongly desirable in the clinical environment. At high field strengths, spectral-selective techniques, such as SPIR and SSE, can achieve much faster fat suppression compared to the traditional inversion recovery approaches.

However, fat-suppressed scans are still time-consuming compared with non-fat-suppressed scans. By including a fat-selective SPIR prepulse and the following spoiler in each TR, the minimum achievable TR increases from 9.7 ms to 32.0 ms, and the total scan duration increases by 228% (shown in Table 6-1) compared with a non-fat-suppressed scan. Using a high-order binomial SSE (1-3-3-1) for water-selective excitation, shorter TR is achieved and scan duration increases only by 76%, but TE has to be significantly increased. Traditional, more time-efficient approaches such as SPIR TFE or low-order binomial SSE (1-1) FFE, which either suppresses lipid signal for central k-space data only, or suppresses on-resonant lipid signal effectively (Figures 6.2b, c), have also been demonstrated to be unsuccessful in providing both adequate fat suppression and high image quality in our experiments.

The new fast fat suppression strategy described in this chapter, which combines fat pre-saturation with sustained fat suppression (Figure 6.2d), is demonstrated to be a more effective approach to achieving fat suppression for short TR gradient echo scans, and it is also time-efficient. By acquiring k-space profiles with a centric order, the lipid signal of central profiles is suppressed twice (by both SPIR and SSE). This is desirable, since the fat suppression in central k-space is of greater importance than that of the peripheral regions. Effective fat suppression in central k-space also decreases the transient effects of fat signal which otherwise leads to image blurring and ghosting. Short, low-order 1-1 binomial RF pulses, generally believed to offer poor spectral selective capability, are shown to be suitable

for efficient sustained fat suppression. These pulses tip most of the water spins, but only a small ratio of lipid spins, to the transverse plane, even when most lipid spins have almost recovered to the longitudinal direction. Due to this mechanism, very long ETL is achievable without severe fat artifacts being introduced (ETL = 256 in Figure 6.4e, Figure 6.7c). The long ETL used decreases the number of SPIR pulses that have to be administered, which reduces the total scan duration. Decreasing the number of SPIR pulses, and the use of SSE, also decreases total RF power deposition and specific absorption rate (SAR) (68,69).

The results obtained from both phantom and human experiments suggest that a long ETL SPIR-SSE TFE sequence outperforms short ETL SPIR TFE for fat suppression. More importantly, SPIR-SSE TFE performs very closely to SPIR FFE and high-order binomial SSE (e.g., 1-3-3-1) FFE sequences as indicated in Figures 6.7a-c. For SPIR FFE sequences, the system default SPIR flip angles may not necessarily be optimal for fat suppression with the specific TR and flip angle used, especially in the clinical environment. However, it has also been reported that a complete fat suppression is not possible using SPIR once TR drops below a certain value for FFE scans (approximately 100 ms at 1.5 T for flip angle = 30º, for example) (70). This is due partly to the fact that, since TR is much shorter than lipid T_1 and T_2, lipid spins will have reached a steady state in the transverse plane when the central k-space profiles are acquired. This leads to a high lipid signal background on the resultant images (71). The same is true for SSE FFE as a perfect 1-3-3-1 SSE pulse train for water-only excitation is not possible. The long ETL used in SPIR-SSE TFE, however, ensures most of the lipid magnetizations return to the longitudinal direction before the administration of the following SPIR. The water-selective excitation further reduces lipid signal from residual fat spin coherences when central k-space data are acquired soon after SPIR fat pre-saturation, even when a large flip angle and a short TR are used. Furthermore, the long ETL used in SPIR-SSE TFE sequences results in high spatial-frequency profiles being acquired during rarely-interrupted steady-state, leading to the visualization of fine lean-tissue structure (less blurring). Thus, superior fat suppression is achieved without the introduction of severe transient artifacts using SPIR-SSE TFE, even though no flip angle sweep techniques are used (72).

As with SPIR and SSE, SPIR-SSE uses spectral-selective excitations and is therefore sensitive to B_0 inhomogeneities. Reliable shimming therefore is mandatory to improve the fat suppression efficacy for the region of interest. The non-spatial-selective SPIR pulses used in our experiment can be replaced by 2D or 3D spatial-selective pulses for fat pre-saturation to avoid water signal suppression in the presence of B_0 inhomogeneities (73,74). An advantage of SPIR-SSE TFE compared with SSE (1-3-3-1) FFE sequence is that SPIR has a much wider stop band (340 Hz in the scanner used), which will suppress lipid spins with much larger off-resonances (for example, resonant frequencies less than $f_{fat} - 110$ Hz, as shown in Figure 6.2) (8). The low-order 1-1 water-selective excitation used in SPIR-SSE TFE also has a wider water pass band than that of a1-3-3-1 SSE. This decreases the chance for unwanted water signal suppression when applied in the presence of B_0 field inhomogeneities. Shorter TE is achieved using SPIR-SSE TFE compared with SSE (1-3-3-1) FFE, thus the resultant image suffers less from T_2^* relaxation. This makes this technique especially suitable for imaging species with short T_2. Currently, by employing low-order binomial 1-1 SSE pulses for sustained fat suppression, the minimum achievable TR and TE are slightly increased over those of SPIR FFE due to the duration of the SSE pulses. In our SPIR-SSE TFE sequences, the system default 1-1 SSE pulse was employed, which had an inter-pulse delay of 2.3 ms. By employing phase modulation of the RF pulses, shorter TR and TE are possible without substantially altering the contrast of the resultant images, which will further decrease the minimum TR and TE, and therefore the total scan duration (63,75).

It is known that rapid fat-suppressed imaging in the breast is technically challenging due to the abundance of fat, possible cardiac/respiratory motion artifacts, and the need for high temporal and spatial resolution with full breast coverage (58). Another challenge is that breast imaging is usually not performed at isocenter, thus B_0 homogeneity is adversely affected. SPIR-SSE TFE sequences, however, offer adequate fat suppression with only slightly increased scan duration. Further scan duration reduction can be achieved by using partial k-space acquisition, and TR/TE can also be decreased by employing partial-echo acquisition. It is also possible to employ this technique in 3D spiral acquisition for ultra-fast whole breast imaging (76,77). Spiral acquisition has the advantages of fast k-space traversal,

insensitivity to bulk- and flow-motion, and less demand for high performance gradients. As with Cartesian acquisition, the low-high (centric) phase encoding (z direction) profile ordering can be acquired first for optimal fat suppression.

As SSE (1-1) offers poor spectral-selective power, the fat suppression efficacy of SPIR-SSE is largely dependent on the effectiveness of SPIR. Overall fat suppression can be further improved by combining fat pre-saturation with higher-order binomial (e.g., 1-2-1) water-selective excitations, at the expense of a longer TR and TE. Although the fat suppression efficacy using the system default SPIR and SSE (1-1) pulses has been validated, more rigorous theoretical analysis has to be performed to understand the behaviors of both water and fat magnetizations, so that scan parameters can be set for optimal lean-tissue imaging and fat suppression. Integrating variable RF flip angle excitation into this technique will greatly improve overall image quality. Following such a systematic analysis, SPIR pulse angle, and SSE pulses (including sub-pulse angles, inter-pulse delay) can be adjusted for optimized fat suppression and image quality when longer SSE pulses are to be used. This is especially important in the presence of B_0 and B_1 inhomogeneities, where longer RF excitation trains may lead to the evolution of complicated magnetization behaviors.

The strategy of combining fat pre-saturation with sustained fat suppression can be employed on any short TR sequences for improved rapid fat suppression. For balanced steady-state free precession (b-SSFP) (31), however, the use of 1-1 binomial RF pulses for water-selective excitation is not preferable. RF (amplitude and/or phase) cycling techniques (78,79) take advantage of the coherent imaging property of b-SSFP, and sustained fat suppression is achievable without increasing TR. This can be combined with magnetization preparation techniques such as that described by Scheffler et al. (32) for fat pre-saturation. This ultra-fast b-SSFP sequence with improved fat suppression is especially suitable for cardiac imaging and angiography.

6.5 Other Sequence Implementations

The fat suppression strategy described herein combines a fat presaturation pulse with sustained fat suppressed excitations in a short-TR TFE sequence. Therefore, fat presaturation methods other than a SPIR pulse, and sustained fat suppressed excitation methods other than SSE can also be used in a pulse sequence to implement this fat suppression strategy.

In SPIR-SSE TFE, SPIR achieves a strong fat presaturation for a wide range of fat off-resonances. However, it has a long pulse duration (15ms) before the following TFE readout train. This will introduce a strong signal steady-state interruption, and change of signal contrast. A much shorter implementation of fat presaturation can be used, such as a binomial fat-selective excitation as shown in Figure 6.8. The pulse sequence employs a user-defined Research PrePulse (REPP) on a Philips MR scanner for the binomial fat presaturation, and is therefore referred to as REPP-SSE sequence in the rest of the chapter. The presaturation duration (about 5 ms) is much shorter compared with that of a SPIR pulse, but the fat suppression bandwidth is narrower. Therefore, it is suitable for fat suppressed imaging on small FOV where B_0 inhomogeneity is not severe. A similar sequence (Figure 6.9) uses SSE, so that fat suppression is only achieved on the imaged region. This might be important for MR angiography to avoid suppressing blood signal out of the field of view.

For a region with severe B_0 inhomogeneities, a double inversion-recovery (DIR) preparation might be beneficial to achieve strong fat saturation on central k-space data (Figure 6.10). This method makes use of the T_1 relaxation time difference between water and fat to achieve fat presaturation, independent of the B_0 inhomogeneities. The delay between the two 180° (TI) is the time is about 170 ms at 1.5 T, so that fat longitudinal magnetization crosses zero when the second 180° RF is applied. The second 180° RF tips mostly water spins to generate positive longitudinal water magnetization so that a long ETL can be used in the following readout train. The drawback of this sequence is that, it is not suitable for contrast-enhanced MR angiography, because the blood signal might also be suppressed due to the short T_1. In addition, an accurate f_0 determination has to be achieved to guarantee that majority of fat signal can be suppressed by the sustained SSE (1-1).
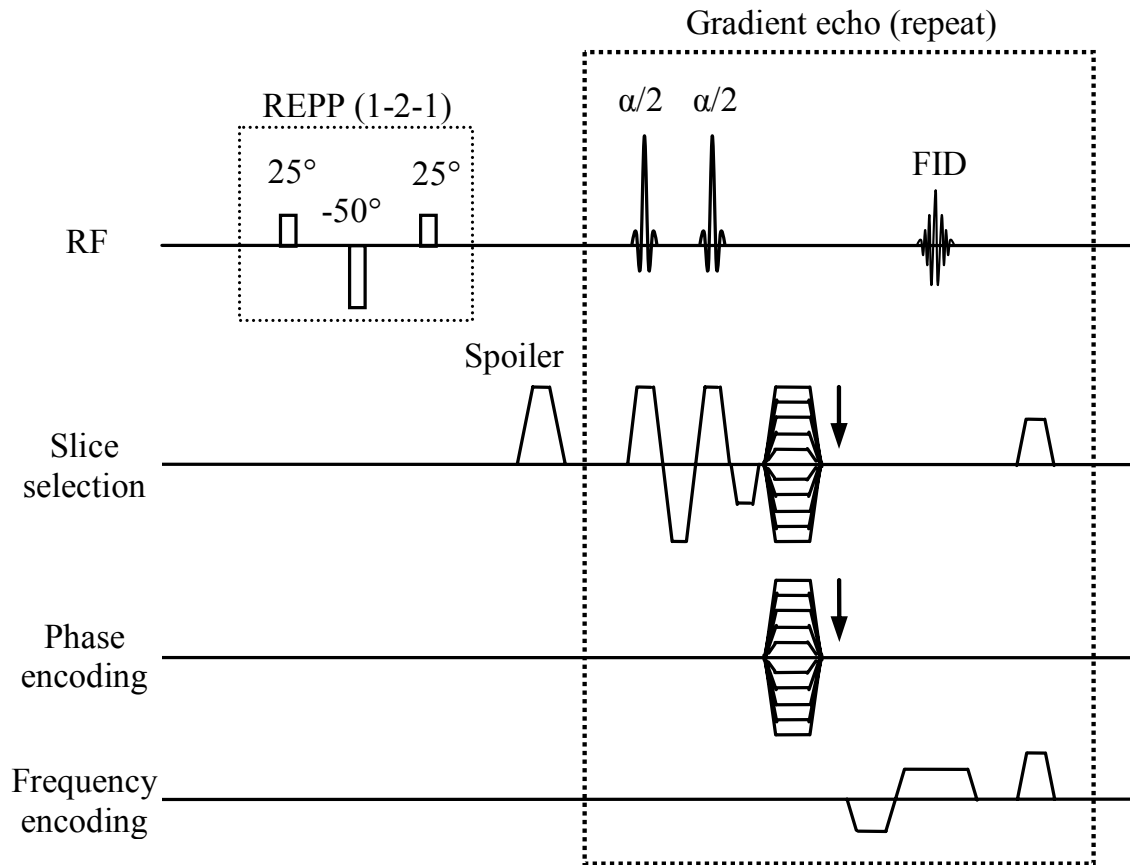
Figure 6.8 Schematic of the REPP-SSE TFE pulse sequence. Fast fat presaturation can be achieved using non-spatially-selective, binomial fat selective excitation, instead of the continuous and time-consuming SPIR pulse. The inter-pulse interval for REPP is 2.3 ms, and the phases of binomial components are (0°, 180°, 0°) to achieve fat-selective excitation. In the second-order binomial REPP pulse-train as shown, the effective excitation is 0° for water, and 100° for fat.
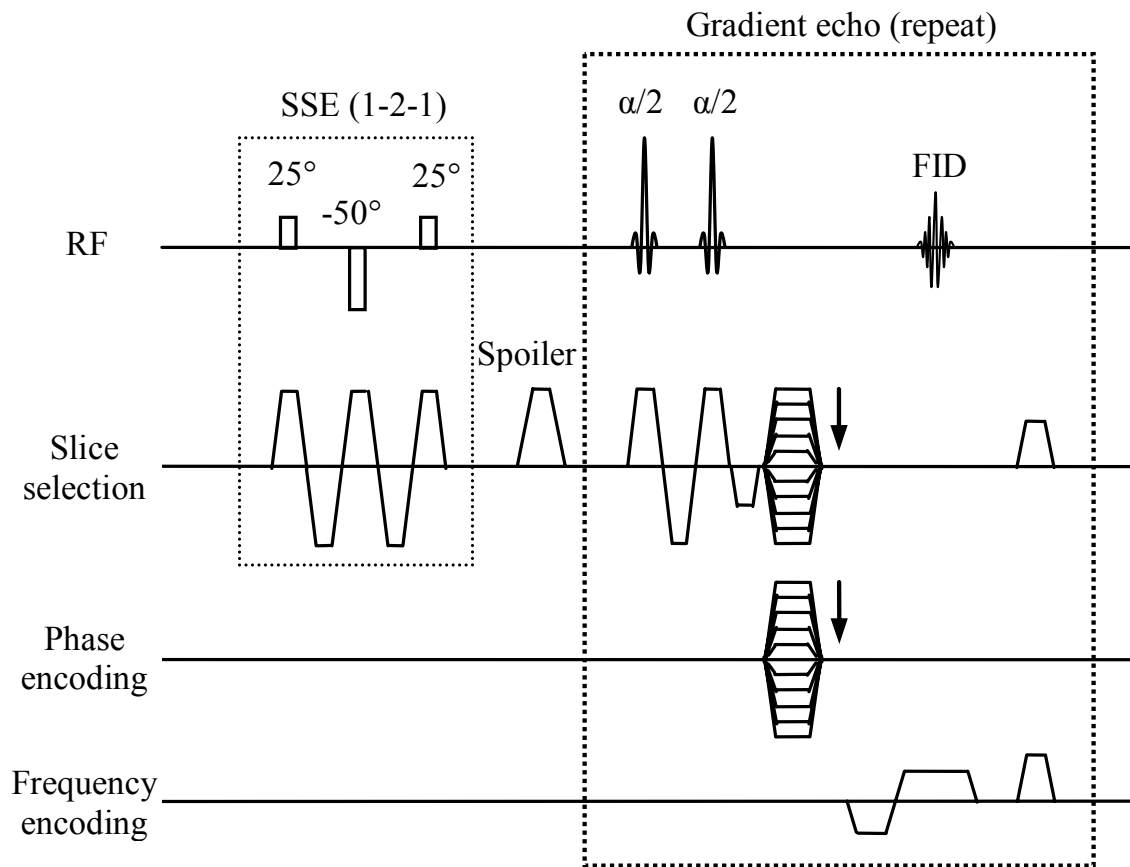
Figure 6.9 Schematic of the SSE-SSE TFE pulse sequence. Fast fat presaturation can be achieved using spectral-spatial selective binomial pulses. The inter-pulse interval for REPP is 2.3 ms, and the phases of binomial components are (0°, 180°, 0°) to achieve fat-selective excitation. In the second-order binomial REPP pulse-train as shown, the effective excitation is 0° for water, and 100° for fat.
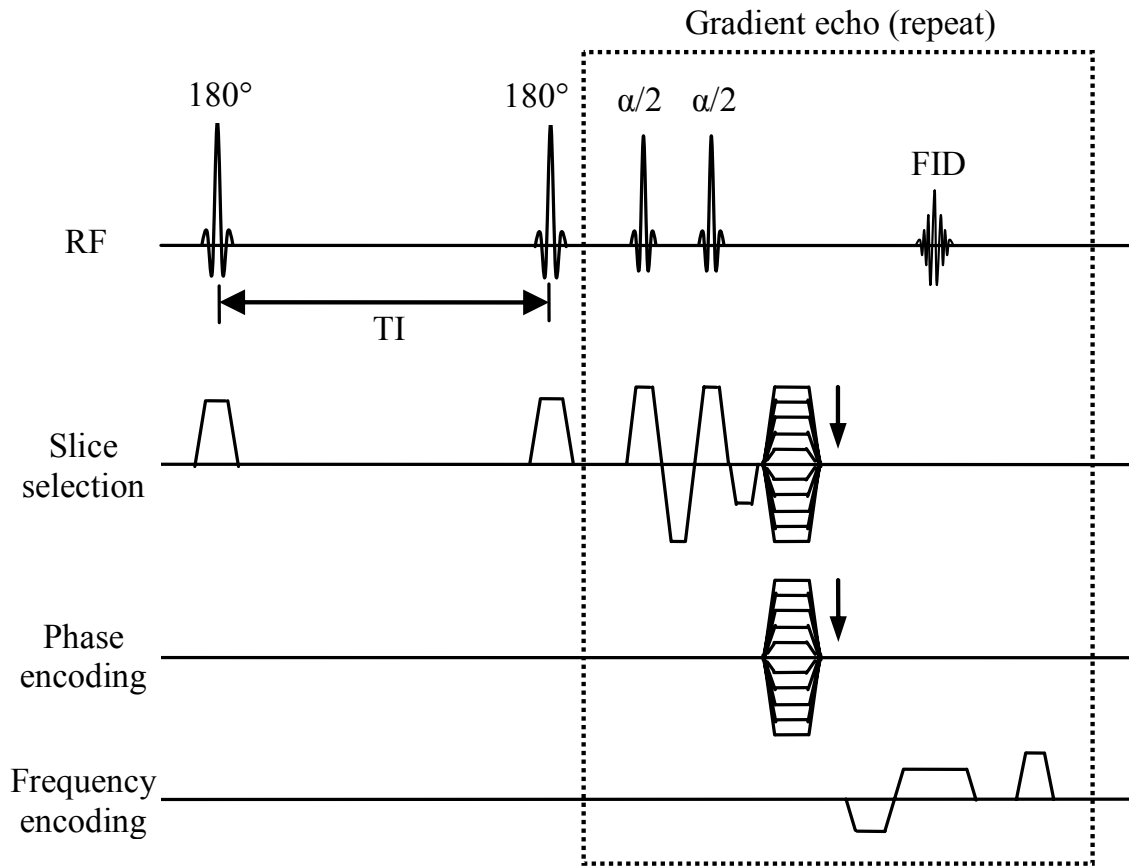
Figure 6.10 Schematic of the DIR-SSE TFE pulse sequence. The double inversion-recovery preparation can be employed for fat presaturation when B_0 is very inhomogeneous. TI is defined as the time delay from the 180° RF excitation to the next 180° RF excitation. The center of k-space data is acquired first to achieve maximum fat suppression.

6.6 Summary

In this chapter, a novel rapid fat suppression strategy for short TR gradient echo sequences has been discussed. This concept is validated with phantom and human experiments using a three-dimensional, RF spoiled TFE sequence, which combines fat pre-saturation using SPIR with sustained water-selective low-order binomial SSE. This sequence offers very close fat suppression performance, in much shorter scan duration, than the traditional SPIR FFE, and SSE FFE sequences. It also generates images suffer much reduced

from blurring and ghosting artifacts compared with fat presaturated SPIR TFE sequences. The experimental results demonstrate that the combination of fat pre-saturation with sustained fat suppression (or water selective excitation) is both an effective and time-efficient strategy. Examples of other possible implementations of this fat suppression strategy are also briefly discussed. The improved fat suppression within reduced scan duration can therefore lead to high image quality, high spatial and temporal resolution, thus improve the diagnosis of breast tumor and other diseases using MRI.

Chapter 7 Rapid Fat-Suppression Applications

7.1 Introduction

Fat suppression can decrease the influence of chemical shift artifacts, improve dynamic range of non-fatty tissue, and enhance lesion conspicuity. Therefore, fat suppression is widely used in clinical MR imaging. In this chapter, clinical applications of the rapid fat suppression strategy will be discussed to demonstrate the usefulness of the novel fat-suppressed imaging technique as described in Chapter 6.

Two clinical examples will be discussed in detail in this chapter: rapid bilateral breast imaging for breast tumor characterization, and articular cartilage imaging.

7.2 Rapid Bilateral Breast Imaging

7.2.1 Introduction

Bilateral breast imaging, or imaging two breasts simultaneously, has many advantages compared with unilateral breast imaging. For the patients, it reduces the number of MRI examinations since two breasts are examined in one visit. Bilateral imaging is also helpful to improve diagnosis. It is easier to evaluate symmetry, and to have a single radiologist evaluate both breasts to generate a more concise report. Bilateral breast imaging also improves SNR in a 3D contrast-enhanced dynamic imaging sequence compared with unilateral breast imaging since the volume of excitation is doubled. This makes bilateral breast imaging suitable to be combined with Sensitivity encoding (SENSE) technique, which sacrifices SNR for a gain in imaging speed (80-82).

However, bilateral breast imaging has been a technical challenge for a number of reasons. First, fat suppression is more challenging since the imaging region is much larger, and a homogeneous magnetic field is more difficult to achieve even after careful volume

shimming. Also, cardiac and respiratory motion is more of a problem for bilateral breast imaging. To reduce motion-induced artifacts, frequency encoding direction is usually chosen to be along anterior-posterior (AP) direction. Therefore, cardiac and respiratory motion will generally introduce ghosting and blurring along left-right (LR) direction, which may contaminate signal from axillae. In addition, the temporal resolution is generally reduced since a larger FOV has to be covered without sacrificing spatial resolution. Therefore, diagnostic specificity may be decreased due to a loss of contrast-enhanced signal sampling speed in dynamic contrast-enhanced studies.

The novel fat suppression strategy discussed in Chapter 6 has been proven to be effective on fat suppression and is also time efficient. The goal of this study is to investigate (a) fat suppression efficacy, and (b) the possibilities to enhance imaging speed for bilateral breast imaging, using the rapid fat suppressed imaging technique discussed earlier.

7.2.2 Fat Suppression Efficacy: Methods

The effectiveness of SPIR-SSE sequence on rapid fat suppressed unilateral breast imaging has been demonstrated in Chapter 6. However, imaging both breasts simultaneously would of great clinical importance since only one contrast agent injection has to be administrated, and one MR exam needs to be performed on the patient to study lesions of either breast. The REPP-SSE sequence as shown in Figure 6.8 was used to test the performance of the proposed fat suppression methodology for rapid fat suppressed bilateral breast imaging.

The same MR scanner and the synergy-array breast coil were employed as described in Chapter 6. Two normal volunteers were scanned (28, and 52 years old, respectively). Careful volume shimming on both breasts was applied before data acquisition. Both transverse and sagittal plane images were acquired and compared between new and traditional sequences. Geometric plan for the axial scans are shown in Figure 7.1a. In the transverse scans, 60 axial images were obtained on the right breast with free breathing, and the measured slice-thickness was 4 mm with 2 mm overlap. Imaging FOV was 33 cm, and matrix size was 512

× 512, leading to measured voxel size to be $0.64 \times 0.64 \times 4.0$ mm^3. The frequency encoding direction was along anterior-posterior (AP) direction to minimize respiratory motion artifacts. The REPP-SSE TFE sequence had TR/TE/FA = 11.0 ms/3.8 ms/15°, NSA = 1. Partial Fourier readout (62.5%) was used to achieve short TR and TE. Sensitivity encoding (SENSE) technique was also employed with SENSE factor = 2 along LR direction (first phase encoding direction). TFE factor was 128, and the first two data acquisitions were discarded to achieve better image quality. The resultant TFE acquisition duration was 1.37 second. Readout bandwidth was 63.2 kHz. The scan duration was 1:50.1 (min:sec). For comparison, fat suppression using traditional fat saturated FFE with SPIR (TR/TE/FA = 32.0 ms/5.4 ms/24°, referred to as SPIR FFE below), spatial-spectral water selective FFE using third-order SSE (1-3-3-1, referred to as SSE (1-3-3-1) FFE) (TR/TE/FA = 18.0 ms/9.2 ms/19° were also tested using the same geometric settings, bandwidth, and SENSE settings. The latter two sequences also used full FID readout along frequency encoding direction, but with 62.5% half scan (partial Fourier acquisition along phase encoding direction), so that scan duration can be decreased. The scan duration for SPIR FFE and SSE (1-3-3-1) FFE were 3:21.9 and 1:56.8 (min:sec), respectively.

The sagittal plane scans had the following TR/TE/FA: REPP-SSE: 10.0 ms/3.7 ms/14°; SPIR FFE: 32.0 ms/5.0 ms/24°; SSE (1-3-3-1) FFE: 18.0 ms/8.8 ms/19°. The sequences also had FOV = 140 mm, and matrix size = 256 × 256. 130 slices were imaged for each sequence to cover both breasts along slice-selection direction. All other parameters were the same as the sequences acquired in transverse plane. Geometric plan for the sagittal scans are shown in Figure 7.1b.
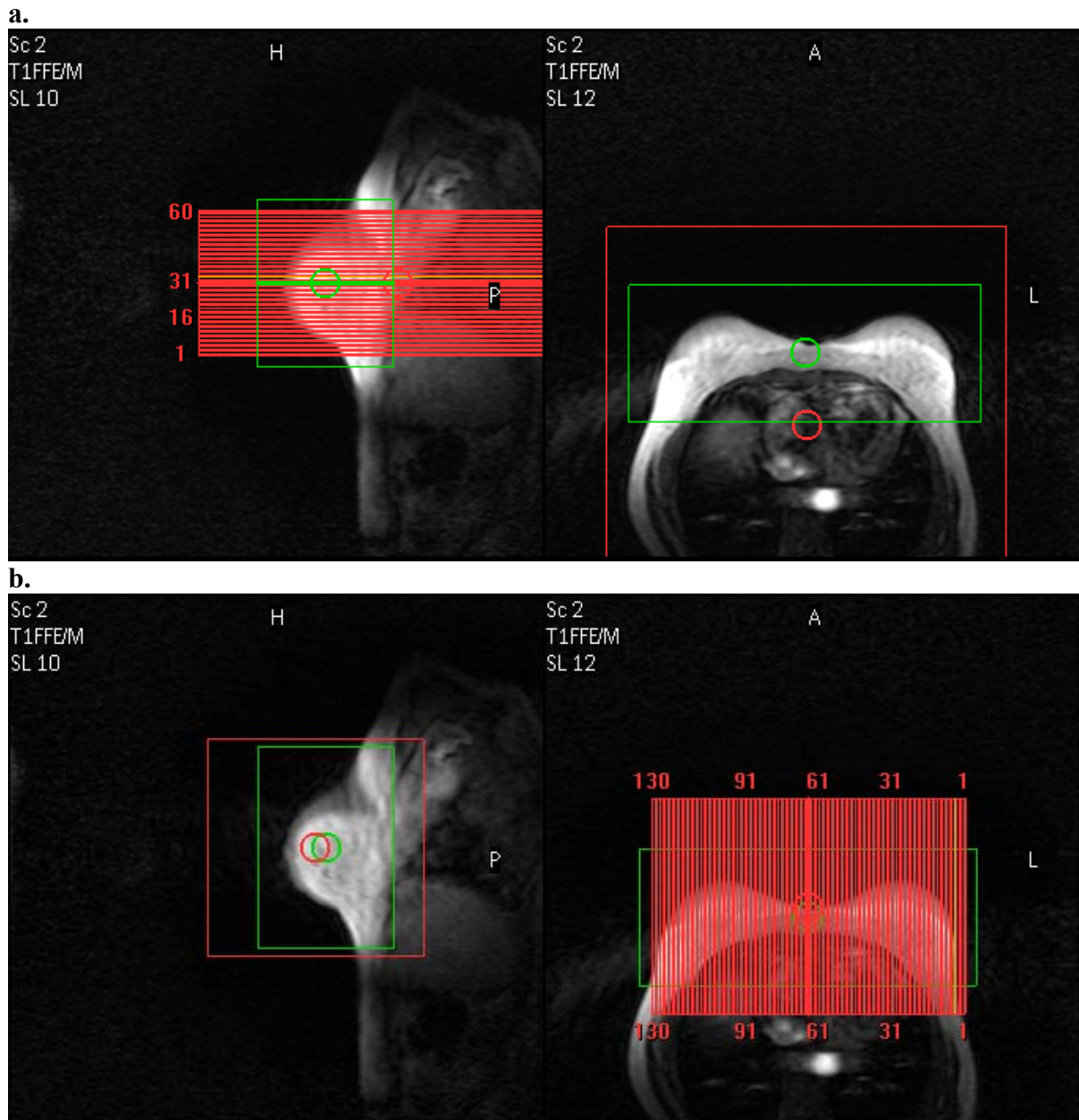
Figure 7.1 Geometric positioning for bilateral breast imaging. Green box represents volume shimming region, and red box or slices represent imaging region or slices. (a) Bilateral transverse plane imaging; (b) Bilateral sagittal plane imaging. Frequency encoding direction is AP, and SENSE direction is LR for both situations.

7.2.3 Fat Suppression Efficacy: Results

Figure 7.2 shows representative images, obtained at the same locations, acquired with three different fat suppression techniques. Homogeneous fat suppression over both breasts was achieved for all three scans. REPP-SSE TFE has the best lean tissue to fat contrast among all three scans. Most importantly, REPP-SSE shows much fewer motion artifacts inside the chest wall, compared with SPIR FFE, and SSE (1-3-3-1) FFE. The motion artifacts were induced by the motion of diaphragm due to breathing, and by the beating of the heart. Motion artifacts are mainly along phase-encoding direction (left-right). Motion artifacts in SSE (1-3-3-1) FFE are the worst since a much longer TE was used in the sequences. The long TE in SSE (1-3-3-1) FFE also makes it sensitive to T_2^* effects, and the signal in voxels with both water and fat is nulled. SPIR FFE has shorter TE, but the relatively long TR (32 ms) makes this sequence sensitive to respiratory motion on the breast, obscuring the fine structure of potential cancer. In addition, the scan duration of SPIR FFE is much longer.

a. REPP-SSE TFE (1:50)   **b.** SPIR FFE (3:22)   **c.** SSE (1-3-3-1) FFE (1:57)
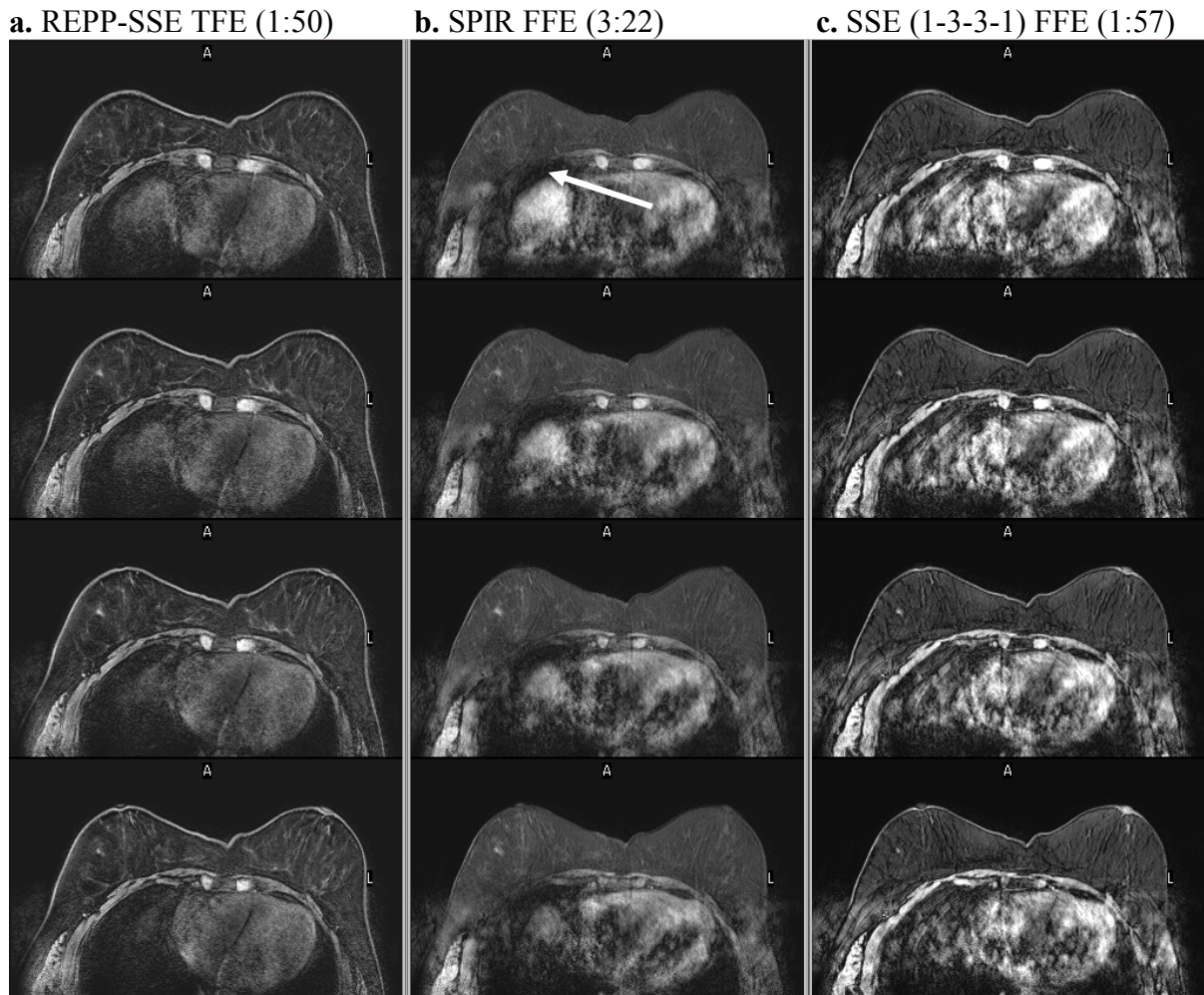
Figure 7.2 Bilateral breast imaging using different pulse sequences (axial). The corresponding sequence and scan duration (in min:sec) are shown above each image. It is obvious that REPP-SSE TFE provides strong fat suppression in shorter scan duration, and suffers much less from motion artifacts along phase encoding direction (LR). In SPIR FFE, a water (muscle) region was also suppressed due to B_0 inhomogeneities as indicated by a white arrow.

Figure 7.3 shows the results obtained along sagittal plane. The image quality of the three tested sequences is comparable as that of transverse plane. The REPP-SSE TFE also shows strong and homogeneous fat suppression, high contrast, and minimum blurring. In SPIR FFE, an artifact on muscle is shown, due to the local B_0 inhomogeneities, and the un-optimized SPIR central frequency.
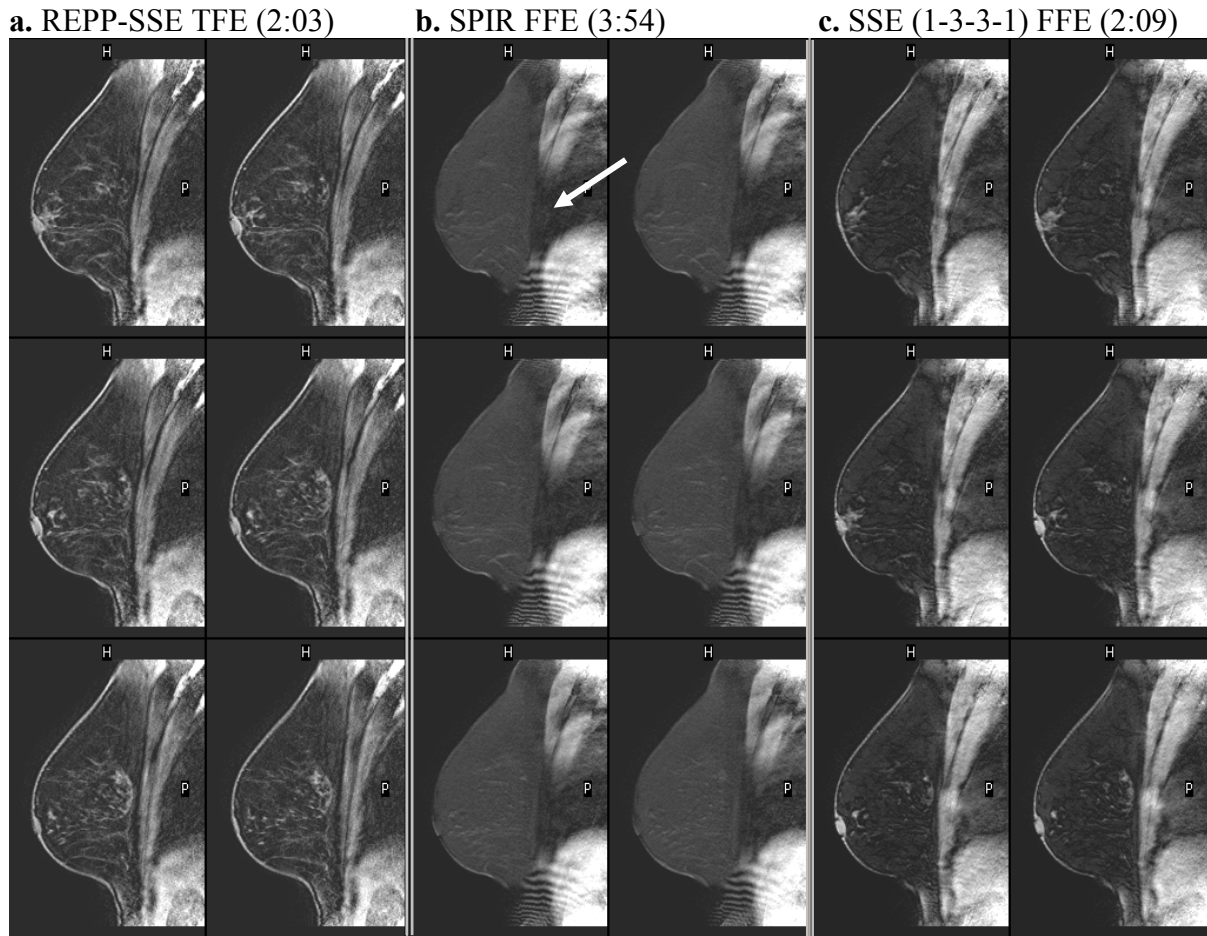
Figure 7.3 Bilateral breast imaging using different pulse sequences (sagittal). The corresponding sequences and scan durations (in min:sec) are shown above the images. In the SPIR FFE images, a portion of chest wall is suppressed due to regional B_0 inhomogeneity and the un-optimized SPIR central frequency (white arrow), which is also shown in the axial images.

7.2.4 Enhancing Imaging Speed: Methods

It is shown in the earlier axial bilateral experiments that REPP-SSE TFE sequence is much less sensitive to motion artifacts, due to reduced TR and TE. Cardiac motion artifacts along the phase-encoding direction are confined, and do not contaminate anatomical structures outside of the chest wall. In contrast, SPIR FFE and SSE (1-3-3-1) FFE are sensitive to cardiac and respiratory motion as shown in Figure 7.2. The axillae in images

obtained from both sequences are contaminated, which hampers the diagnosis of possible malignancy in this region.

The insensitivity to motion of the REPP-SSE sequence tested might offer more for improved bilateral breast imaging. Since bilateral breasts have a longer dimension along RL, it might be possible to employ frequency encoding direction along LR with a reduced number of phase encoding steps along AP direction. This can be achieved by a reduced rectangular FOV (rFOV) for breasts and axillae only imaging. The reduction of phase-encoding steps and reduced scan duration will not compromise spatial resolution.

Two experiments were performed on a 28-year-old subject to validate this concept. The first approach used the same synergy-array breast coil as in the previous experiments. However, this coil is not compatible with the SENSE technique along AP direction. Therefore, in the second experiment, SENSE-body coil was used to test the performance of the new approach in combination with SENSE technique for a significant imaging speed enhancement.

The pulse sequence used in the first experiment was similar to the REPP-SSE sequence used earlier in Section 7.2.1, except rFOV was set to 50%, and no SENSE technique was used. The scan duration was therefore the same. Geometric plan for this scan is demonstrated in Figure 7.4. The scan duration of this sequence was 1:52.4 (min:sec).

In the second experiment, eighty slices instead of sixty were acquired in all sequences tested. All experiments had SENSE factor = 2 along the first phase-encoding direction. For comparison, the REPP-SSE sequence with the first phase-encoding direction along LR was tested. The scan duration was 2:25 (min:sec). The phase-encoding direction was then set to AP, and rFOV = 50% in the second scan. Finally, a scan similar to the second one was tested by setting scan percentage to 50%. Although this would lead to a reduction of spatial resolution along AP direction, it increased SNR and reduced scan duration by 50%.

7.2.5 Enhancing Imaging Speed: Results

The lower eight images in Figure 7.4 are the representative images of the sequences tested in the first experiment. It is validated that it is feasible to use phase encoding direction along AP direction without introducing motion contamination into the breasts. There are some slight fold-over artifacts in the anterior air region (close to the image upper-border), but they are outside of the breasts.
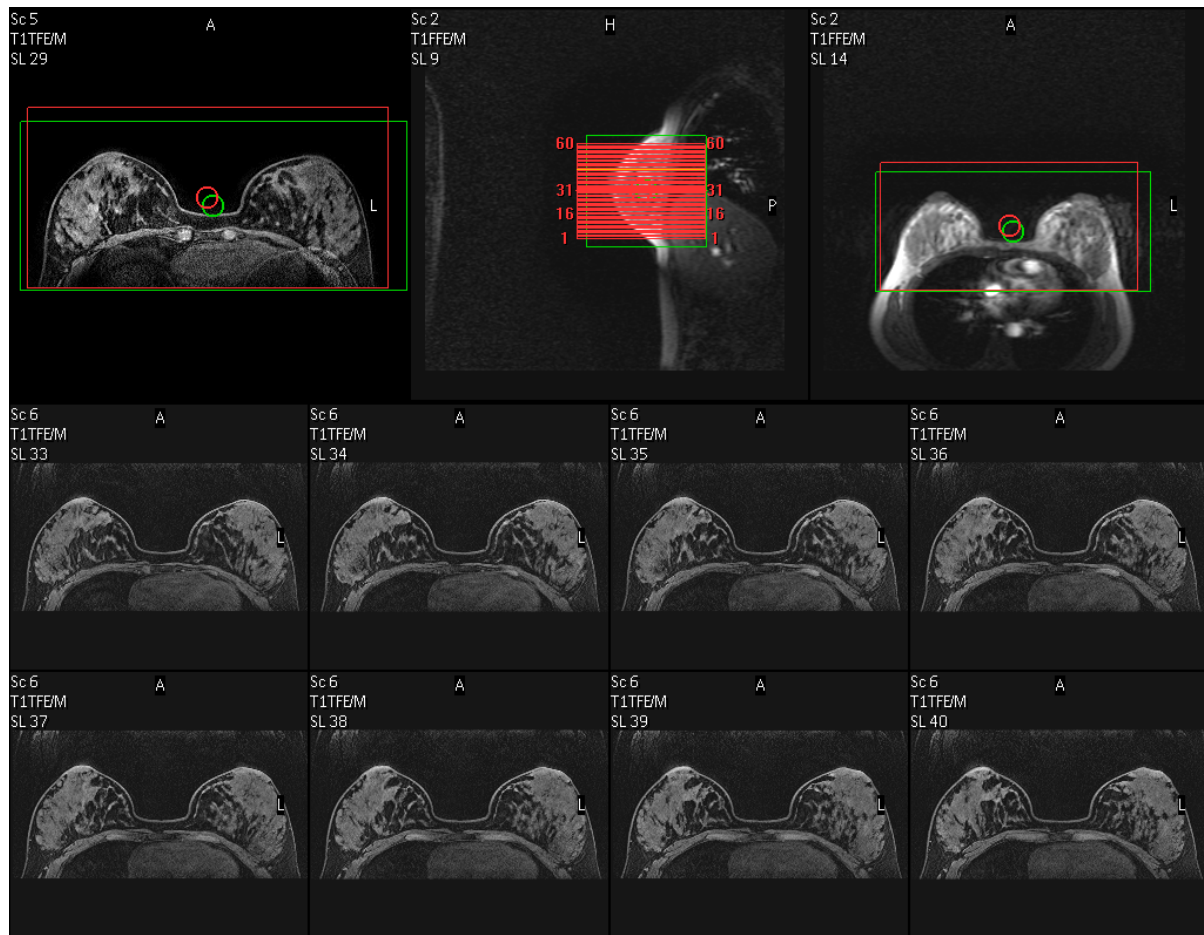
Figure 7.4 Geometric plan and resultant images of fast bilateral breast imaging. The first phase-encoding direction was set to AP, and rFOV was set to 50% to achieve a 50% scan duration reduction. No SENSE technique was employed in this experiment. There are some slight foldover artifacts in the anterior air region, which does not contaminate the breast signal.
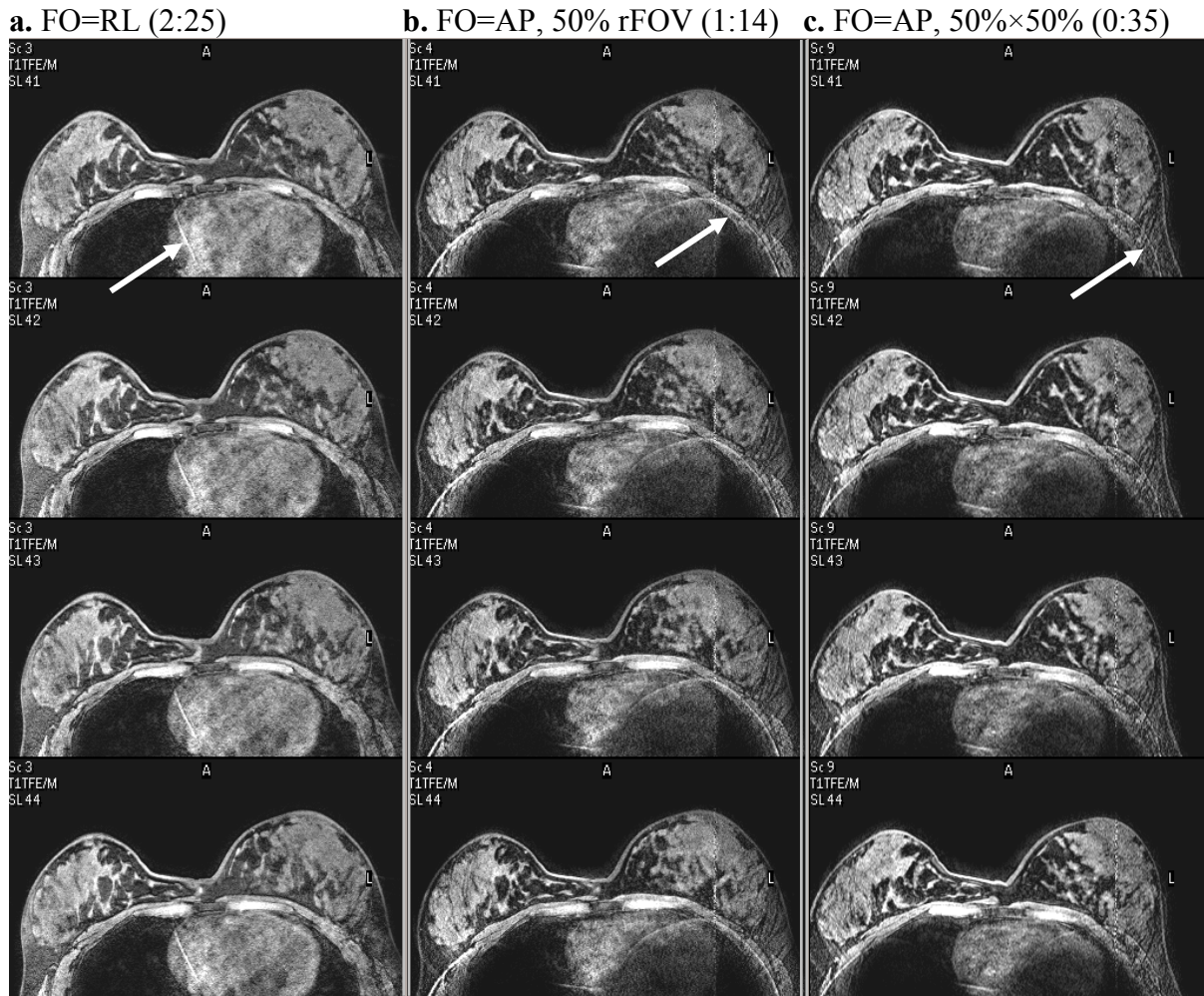
Figure 7.5 Comparison of fast bilateral breast imaging sequences. The corresponding scan durations (in min:sec) are shown above the images. All sequences used REPP-SSE fat suppression, and a SENSE factor of two along the first phase encoding direction. Slight SENSE artifacts are shown with white arrows. (a) Fold over direction is along LR, and rFOV = 100%. (b) Fold over direction is along AP, and rFOV = 50%. (c) Same as in (b) except scan percentage was set to 50%.

Figure 7.5 shows the representative images of the three sequences tested in the second experiment, using the SENSE-body coil. All images demonstrate slight SENSE artifacts indicated by the white arrows. The SENSE artifacts can be minimized by a better coil design, and reduced patient bulk motion after the SENSE reference scan. Consistent with the results in the first experiment, artifacts due to cardiac motion are slight and localized, without

contaminating breast signal. High image quality is obtained in the second and third scans, even though scan duration is much shorter.

7.2.6 Summary

It is shown in these experiments that the REPP-SSE sequence has high quality fat suppression, high lean tissue to fat contrast, good motion insensitivey, and short scan duration. The high quality fat suppression is achieved by employing a short 100°, fat selective, REPP (1-2-1) prepulse train for fat-only presaturation, combined with a long TFE readout train with SSE (1-1) water-selective excitation. Partial-Fourier readout also helps to reduce the sequence minimum achievable TE and TR without sacrificing spatial resolution. The centric (low-high) view order guarantees strong fat presaturation in central k-space, and also helps to reduce motion artifacts. The experimental results agree well with the theoretical predictions.

It has been demonstrated that the motion insensitivity of this sequence can be used to achieve even higher imaging speed without the introduction of motion artifacts. This is achieved by choosing a phase encoding direction along AP in bilateral breast imaging. In comparison to SENSE, the gain in imaging speed does not sacrifice SNR. Therefore, this improvement in temporal resolution without compromising image quality may have an impact on breast tumor characterization for improved bilateral breast imaging. Therefore, it warrants further clinical contrast-enhanced studies.

7.3 Articular Cartilage Imaging

7.3.1 Introduction

Osteoarthritis (OA) is one of the most common chronic diseases which is related to the structural damage of articular cartilage. Assessment of the degree of damage is important for

monitoring the progression of OA and evaluating possible therapeutic response. MRI has been widely used for the diagnosis and for the monitoring of this disease. Articular cartilage may be evaluated with fat-suppressed T2-weighted 2D fast spin-echo or fat suppressed proton density fast spin-echo. However, T1-weighted fat suppressed spoiled gradient echo sequences (or T1W SPIR FFE for Philips scanners) have been most widely accepted for cartilage quantification. The drawback of this sequence is the lengthy scan times. T1W FFE with SSE for water selective articular cartilage has also been validated to be effective with shorter scan durations compared with that of fat presaturated FFE (63). However, the highest spatial resolution achievable using traditional spoiled gradient echo sequences is fundamentally limited by the image SNR. Therefore, a sequence with high SNR efficiency would be desirable for articular cartilage imaging. B-SSFP which discussed in Chapter 3 is known to have an optimal SNR efficiency, and is also strongly T2-weighted, and the usefulness of this approach has also been studies (83).

In this section, REPP-SSE sequence will be tested on articular cartilage and compared with traditional sequences. In addition, a REPP-SSE (1-1) b-SSFP sequence will also be tested to achieve T2-weighted images.

7.3.2 Methods

In T1W FFE (or TFE), SNR and CNR are determined by TR, TE and flip angle used in the pulse sequence. Therefore, an optimal flip angle has to be determined to obtain a compromise between SNR of articular cartilage and CNR between cartilage and synovial fluid. The T_1 and T_2 values are listed in Table 7-1 and signal of each tissue is calculated from Bloch Equation simulation. TR = 14 ms and TE = 5.1 ms were used in the simulation. The results of the simulation are portrayed in Figure 7.6. An optimal flip angle was found to be about 15° to obtain a compromise between SNR and CNR for articular cartilage imaging.

Table 7-1 T_1 and T_2 values of knee tissue used in the signal simulation

	Cartilage	Synovial fluid	Fat	Bone marrow	Meniscus	Muscle
T_1 (ms)	770	1470	310	290	500	980
T_2 (ms)	39	535	47	47	7	31
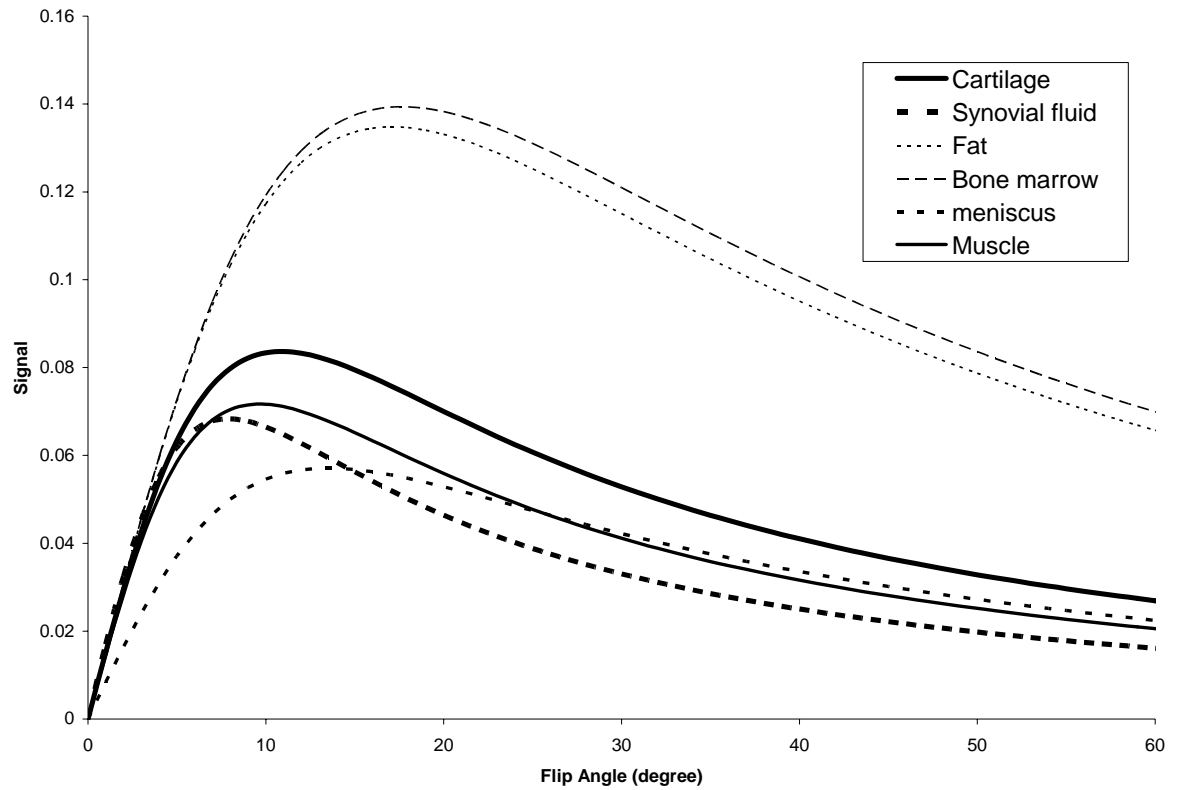
Figure 7.6 Simulation of tissue signal for articular cartilage imaging. Experimental TR/TE = 14 ms/5.1 ms was used in the simulation. A flip angle at about 15º will offer a compromise to reach a high SNR of cartilage, and a high contrast of cartilage to synovial fluid.

The same 1.5 T Philips Intera MR scanner and a knee coil were employed for articular cartilage imaging on the knee. The same two normal volunteers as in the breast studies were scanned on the left knee. Volume shimming was applied before data acquisition. 75 axial images were obtained in the axial plane, and the measured slice-thickness was 2 mm with 1 mm overlap. Imaging FOV was 15 cm, and matrix size was 352 × 352, leading to measured voxel size to be 0.43 × 0.43 × 2.0 mm³. The REPP-SSE TFE sequence had TR/TE/FA = 14.0

ms/5.1 ms/15°, NSA = 1, and partial Fourier readout (62.5%) was use to achieve the short TE. TFE factor was 64, and the first two data acquisitions were discarded to achieve better image quality. Readout bandwidth was 49 kHz. For comparison, fat suppression using traditional SSE (1-1) FFE with the same TR/TE/FA as in REPP-SSE TFE, SSE (1-3-3-1) FFE with TR/TE/FA = 28.0 ms/16 ms/30° were also tested using the same geometric settings and readout bandwidth. The SPIR FFE sequence was not tested due to its long scan duration. The SSE (1-3-3-1) FFE sequence also used full FID readout along frequency encoding direction, but with 62.5% half scan (partial Fourier acquisition along phase encoding direction), so that scan duration can be decreased without reducing spatial resolution. In addition, all three scans were flow compensated.

To obtain strongly T2-weighted images, a fat-saturated 3D segmented b-SSFP (or b-TFE) sequence was tested on another subject. The sequence employed a REPP (1-2-1) fat presaturation in combination with SSE (1-1) continuous water-selective excitations. The sequence also had 70 axial slices, FOV = 200 mm, MS = 400 × 400, TR/TE/FA = 7.8 ms/3.3 ms/30°, TFE factor = 64, number of dummy echoes = 5. Partial Fourier echo readout was also used to achieve a decreased TR. The readout bandwidth was 228.9 kHz. For comparison, a T1-weighted REPP-SSE TFE sequence with the same geometric parameters was also tested.

7.3.3 Results

Figure 7.7 shows representative images in transverse plane, obtained at the same location, acquired with the three pulse sequences. Homogeneous fat suppression was achieved for both REPP-SSE TFE and SSE (1-3-3-1) FFE. REPP-SSE TFE also has high lean-tissue to fat contrast. Fat suppression of SSE (1-1) TFE is incomplete, and the contrast between articular cartilage and fat/bone marrow is low. As in the breast studies, the long TE in SSE (1-3-3-1) FFE also makes it sensitive to T_2^* effects, and the signal in voxels with both water and fat is nullified. The SSE (1-3-3-1) FFE images also have severe flow artifacts.

a. REPP-SSE TFE (4:15)   **b.** SSE (1-1) FFE (4:04)   **c.** SSE (1-3-3-1) FFE (4:55)
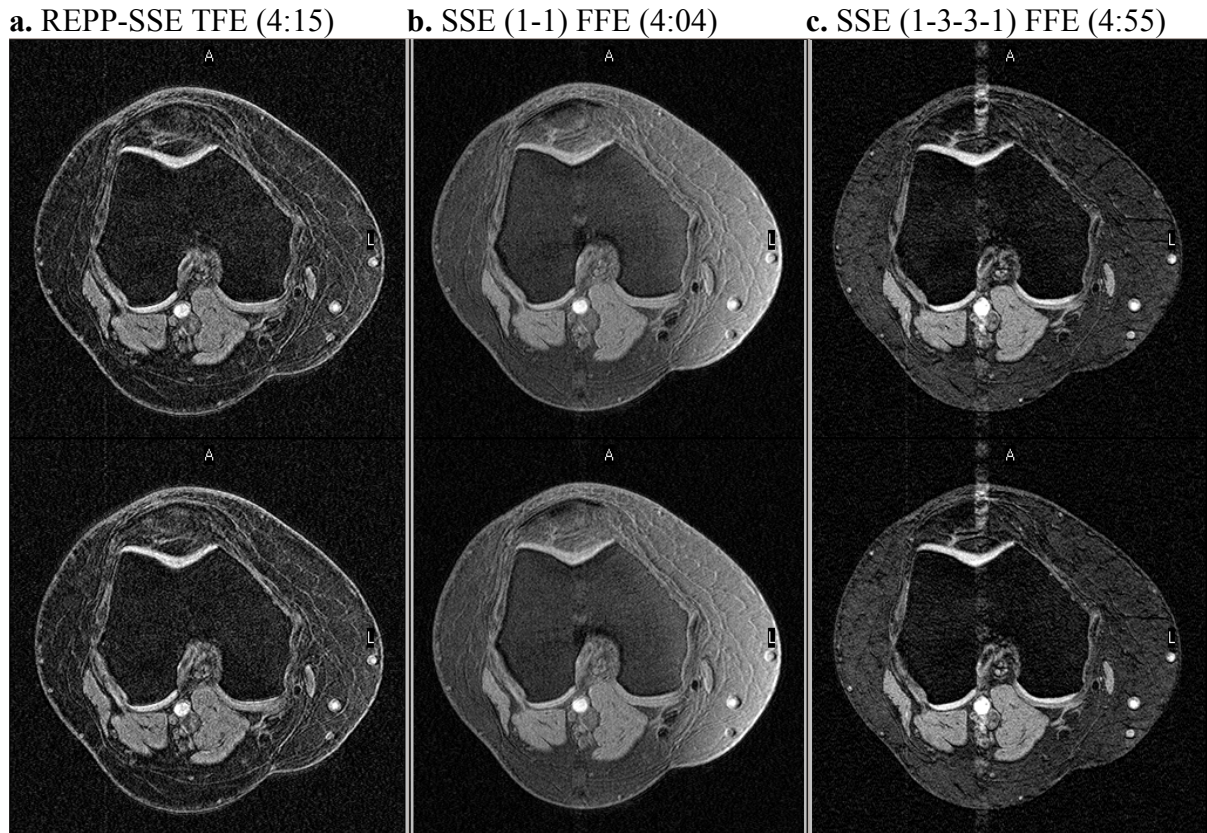
Figure 7.7 Fat suppressed axial knee imaging using different pulse sequences. The corresponding sequences and scan durations (in min:sec) are shown above the images. SSE (1-1) FFE shows incomplete fat suppression, and SSE (1-3-3-1) FFE shows severe flow artifacts, compared with REPP-SSE TFE.

Figure 7.8 shows images obtained with REPP-SSE TFE and the WS b-SSFP sequence in another experiment. Both sequences achieved strong and homogeneous fat suppression by using the novel fat suppression strategy. Since b-SSFP is T_2/T_1 weighted, synovial fluid has bright signal and is evident in the shown images in column (b). In addition, SNR of cartilage in b-SSFP is higher compared with that of REPP-SSE, since it is a coherent imaging technique. The high contrast between synovial fluid and articular cartilage improves the conspicuity of any potential cartilage lesions. The synovial fluid signal in REPP-SSE TFE images indicated with white arrows is relatively dark compared with bright cartilage. Therefore, the REPP-SSE TFE is validated to offer a strong T_1-weighting for cartilage imaging.

a. REPP-SSE (1-1) TFE (4:03)   **b.** REPP-SSE (1-1) b-SSFP (2:38)
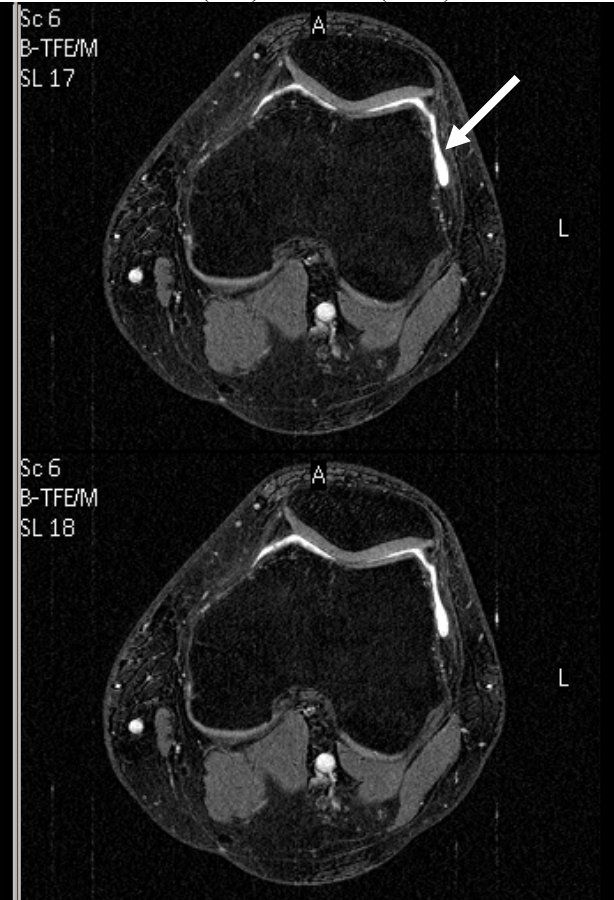
Figure 7.8 Comparison of T1- and T2- weighted knee imaging. (a) Synoid fluid signal is suppressed in REPP-SSE TFE images compared with cartilage signal. (b) High contrast between articular cartilage and synoid fluid (white arrows) can be obtained using a rapid fat-suppressed b-SSFP sequence which is strongly T_2-weighted.

7.3.4 Summary

Fat suppressed, strongly T_1-weighted, or T_2-wighted pulse sequences are the methods of choice for the study of articular cartilage lesions. The drawback of the traditional T_1-weighted RF spoiled gradient echo (or field echo) sequence using SPIR for fat suppression is its long scan duration. The REPP-SSE pulse sequence has been validated to offer robust fat suppression, strong T_1-weighting, and high imaging quality in much shorter scan duration. Traditionally, long-TR TSE sequences are usually used to generate T_2-weighted images. These sequences are usually slow and quite motion sensitive. The WS b-SSFP sequence which employs the novel fat suppression strategy has also been demonstrated to provide strong T_2-weighting and high SNR of cartilage in very short scan duration. Therefore, both the T_1-, and T_2- weighted pulse sequences tested with the novel fat suppression strategy warrant further study of the clinical potential for improved diagnosis of articular cartilage damage.

Chapter 8 Summary and Future Directions

8.1 Summary

Magnetic resonance imaging is becoming a widely accepted diagnostic imaging modality for many disorders in different parts of human body. The major limitations of MRI have been the relative slow imaging speed (or high expense), and the imaging quality (including resolution and contrast). In many applications, MRI is also complicated by the chemical shift between water and fat. The work in this dissertation concentrates on novel rapid chemically selective imaging methods to generate high quality fat-only or water-only images.

Three major technical innovations described in this dissertation are: (a) a rapid fat imaging method; (b) a rapid fat quantification method; (c) a rapid fat suppression strategy. All these methods or concepts have been validated by phantom and human experiments. These contributions are summarized here:

- The theoretical background of a rapid fat imaging technique based on a 3D magnetization prepared b-SSFP has been examined. Signal simulations show that the new method can provide superior SNR and CNR compared with traditional fat imaging methods within much shorter scan duration.

- A WS b-SSFP pulse sequence has been optimized for evaluation of this method. Experiments on a human abdomen phantom show this method can provide significantly more close fat volume estimation compared with traditional WS TSE method in shorter scan duration. The performance of this method has also been found to be close to CT on the same phantom.

- The same WS b-SSFP method has also been tested for human abdominal fat distribution imaging. Image quality (SNR and CNR), and IAF, SAF and TAF

volumes using this method have been compared with using traditional methods. WS b-SSFP has been found to provide superior image quality, and close fat quantification results compared with traditional methods.

- A novel, automated fat quantification method for WS b-SSFP images has been proposed. This method is more accurate compared with tradition contour-drawing methods and other computer-aided methods, since fat from both full-volume and partial-volume fat voxels are considered. The phantom and human experimental results agree well with the theoretical model.

- A novel rapid fat suppression strategy in short-TR pulse sequences has been proposed. Both phantom and human results demonstrate that this strategy can achieve high fat suppression efficacy in short scan duration. Several possible pulse sequence implementations have also been illustrated.

- Rapid fat suppressed bilateral breast imaging and rapid articular cartilage imaging on human knee have been demonstrated as clinical examples of the novel rapid fat suppression strategy. The results show that the novel fat suppression method has great potential in clinical MR examinations.

8.2 Future Directions

Although all the new methods have been validated in this dissertation, there is still room for further technical improvements, and for wider clinical and research applications. The possible future directions are summarized in the following sections.

8.2.1 Rapid Fat Imaging

- Improve spectral signal pass-band width of the WS b-SSFP sequence so that a larger 3D volume can be imaged without banding artifacts. As b-SSFP is sensitive to B_0 inhomogeneities, banding artifacts are readily shown in subcutaneous fat regions on large patients. Therefore, a sequence with the benefit of the high imaging speed and high SNR of b-SSFP, while having a wider spectral response bandwidth, is greatly desired (84).

- Improve the fat imaging speed by using even shorter TR, and by combining WS b-SSFP with parallel imaging techniques (such as SENSE).

- Improve the current WS b-SSFP sequence by reducing SAR and acoustic noise without reducing imaging speed or sacrificing image quality.

- Develop a method for the correction of image distortion induced by B_0 inhomogeneities. Much more accurate fat quantification can be achieved if geometric distortion is reduced or corrected, particularly for subcutaneous fat on large size subjects.

- Develop rapid whole-body fat imaging techniques for whole-body fat distribution monitoring for patients with obesity-related disease such as type II diabetes.

- Test the feasibility for fat imaging at higher magnetic fields, such as at 3 T. Fat imaging using b-SSFP at 3 T would be more challenging than at 1.5 T due to SAR restrictions, and significantly increased B_0 and B_1 inhomogeneities.

8.2.2 Rapid Fat Quantification

- Develop a fully-automated method for rapid IAF, SAF, TAF quantification. This can be achieved by using an automatic segmentation program to generate a contour between IAF and SAF. Therefore, fat quantification for each slice can be automatically performed in a faster and more accurate manner without human intervention.

- Study the influence of the truncation effect (or Gibbs effect) on the estimation of fat quantification on typical abdominal fat images. This effect will generally lead to an overestimation of fat volume. But the significance on fat quantification in humans has not been studied quantitatively.

- If a rapid whole-body fat imaging method can be developed, a rapid, fully automated fat quantification method would benefit many projects. The method is preferably able to provide fat volume information for different regions of human body, and provide inter- and intra- subject comparisons for longitudinal studies.

8.2.3 Rapid Fat Suppressed Imaging

- Test the new fat suppression strategy at higher magnetic fields, such as at 3 T. At higher fields, B_0 and B_1 inhomogeneities will be more severe compared with 1.5 T. Therefore, the efficacy has to be re-evaluated at 3 T.

- Improve the imaging speed and fat suppression performance of the new strategy with the employment of higher order shimming, and longer ETL.

- Further improve fat suppression by customizing the view-order based on the imaged FOV. To obtain an optimized view order, a fat-only prescan can be performed prior to the real fat suppressed scan, and k-space profiles can be reordered according the fat

energy distribution. Therefore, superb fat suppression can be achieved with minimum time penalty (85).

- Test the efficacy of the new fat suppression method when combined with spiral and radial readout trajectories in 3D imaging. Those non-Cartesian readout trajectories have the potential to generate images less sensitive to motion, and T_2^* in shorter scan duration. In those trajectories, a low-high profile order can be used along slice-encoding direction to achieve an effective and efficient fat suppression.

REFERENCES

1. Lauterbur PC. Image formation by induced local interactions: Examples employing nuclear magnetic resonance. Nature 1973;242:190.

2. Haacke EM, Brown RW, Thompson MR, Venkatesan R. Magnetic resonance imaging - physical principles and sequence design. New York: John Wiley & Sons; 1999.

3. Bydder GM, Young IR. MR imaging: clinical use of the inversion recovery sequence. J Comput Assist Tomogr 1985;9(4):659-675.

4. Bydder GM, Pennock JM, Steiner RE, Khenia S, Payne JA, Young IR. The short TI inversion recovery sequence--an approach to MR imaging of the abdomen. Magn Reson Imaging 1985;3(3):251-254.

5. Dixon WT. Simple proton spectroscopic imaging. Radiology 1984;153(1):189-194.

6. Glover GH, Schneider E. Three-point Dixon technique for true water/fat decomposition with B0 inhomogeneity correction. Magn Reson Med 1991;18(2):371-383.

7. Hardy PA, Hinks RS, Tkach JA. Separation of fat and water in fast spin-echo MR imaging with the three-point Dixon technique. J Magn Reson Imaging 1995;5(2):181-185.

8. Mao JT, Bidgood WD, Jr., Ang PG, Mancuso A, Yan H. A clinically viable technique of fat suppression for abdomen and pelvis. Magn Reson Med 1991;21(2):320-326.

9. Keller PJ, Hunter WW, Jr., Schmalbrock P. Multisection fat-water imaging with chemical shift selective presaturation. Radiology 1987;164(2):539-541.

10. Meyer CH, Pauly JM, Macovski A, Nishimura DG. Simultaneous spatial and spectral selective excitation. Magn Reson Med 1990;15(2):287-304.

11. Schick F. Simultaneous highly selective MR water and fat imaging using a simple new type of spectral-spatial excitation. Magn Reson Med 1998;40(2):194-202.

12. Abate N. Insulin resistance and obesity. The role of fat distribution pattern. Diabetes Care 1996;19(3):292-294.

13. Kenchaiah S, Evans JC, Levy D, Wilson PW, Benjamin EJ, Larson MG, Kannel WB, Vasan RS. Obesity and the risk of heart failure. N Engl J Med 2002;347(5):305-313.

14. Blair D, Habicht JP, Sims EA, Sylwester D, Abraham S. Evidence for an increased risk for hypertension with centrally located body fat and the effect of race and sex on this risk. Am J Epidemiol 1984;119(4):526-540.

15. Stoll BA. Obesity and breast cancer. Int J Obes Relat Metab Disord 1996;20(5):389-392.

16. Foster MA, Hutchison JM, Mallard JR, Fuller M. Nuclear magnetic resonance pulse sequence and discrimination of high- and low-fat tissues. Magn Reson Imaging 1984;2(3):187-192.

17. Seidell JC, Bakker CJ, van der Kooy K. Imaging techniques for measuring adipose-tissue distribution--a comparison between computed tomography and 1.5-T magnetic resonance. Am J Clin Nutr 1990;51(6):953-957.

18. Fowler PA, Fuller MF, Glasbey CA, Cameron GG, Foster MA. Validation of the in vivo measurement of adipose tissue by magnetic resonance imaging of lean and obese pigs. Am J Clin Nutr 1992;56(1):7-13.

19. Abate N, Burns D, Peshock RM, Garg A, Grundy SM. Estimation of adipose tissue mass by magnetic resonance imaging: validation against dissection in human cadavers. J Lipid Res 1994;35(8):1490-1496.

20. Tintera J, Harantova P, Suchanek P, Dvorakova A, Adamova M, Hajek M, Poledne R. Quantification of intra-abdominal fat during controlled weight reduction: assessment using the water-suppressed breath-hold MRI technique. Physiol Res 2004;53(2):229-234.

21. Stehling MK, Turner R, Mansfield P. Echo-planar imaging: magnetic resonance imaging in a fraction of a second. Science 1991;254(5028):43-50.

22. Sekihara K. Steady-State Magnetizations in Rapid Nmr Imaging Using Small Flip Angles and Short Repetition Intervals. Ieee Transactions on Medical Imaging 1987;6(2):157-164.

23. Carr H. Steady-state free precession in nuclear magnetic resonance. Phys Rev 1958;112:1693-1701.

24. Jung BA, Hennig J, Scheffler K. Single-breathhold 3D-trueFISP cine cardiac imaging. Magn Reson Med 2002;48(5):921-925.

25. Foo TK, Ho VB, Marcos HB, Hood MN, Choyke PL. MR angiography using steady-state free precession. Magn Reson Med 2002;48(4):699-706.

26. Jeong EK, Kim SE, Parker DL. High-resolution diffusion-weighted 3D MRI, using diffusion-weighted driven-equilibrium (DW-DE) and multishot segmented 3D-SSFP without navigator echoes. Magn Reson Med 2003;50(4):821-829.

27. Zur Y, Bosak E, Kaplan N. A new diffusion SSFP imaging technique. Magn Reson Med 1997;37(5):716-722.

28. Paliwal V, El-Sharkawy AM, Du X, Yang X, Atalar E. SSFP-based MR thermometry. Magn Reson Med 2004;52(4):704-708.

29. Scheffler K. Fast frequency mapping with balanced SSFP: theory and application to proton-resonance frequency shift thermometry. Magn Reson Med 2004;51(6):1205-1211.

30. Scheffler K, Seifritz E, Bilecen D, Venkatesan R, Hennig J, Deimling M, Haacke EM. Detection of BOLD changes by means of a frequency-sensitive trueFISP technique: preliminary results. NMR Biomed 2001;14(7-8):490-496.

31. Scheffler K, Lehnhardt S. Principles and applications of balanced SSFP techniques. Eur Radiol 2003;13(11):2409-2418.

32. Scheffler K, Heid O, Hennig J. Magnetization preparation during the steady state: fat-saturated 3D TrueFISP. Magn Reson Med 2001;45(6):1075-1080.

33. Deshpande VS, Shea SM, Laub G, Simonetti OP, Finn JP, Li D. 3D magnetization-prepared true-FISP: a new technique for imaging coronary arteries. Magn Reson Med 2001;46(3):494-502.

34. Deshpande VS, Shea SM, Chung YC, McCarthy RM, Finn JP, Li D. Breath-hold three-dimensional true-FISP imaging of coronary arteries using asymmetric sampling. J Magn Reson Imaging 2002;15(4):473-478.

35. Hargreaves BA, Vasanawala SS, Pauly JM, Nishimura DG. Characterization and reduction of the transient response in steady-state MR imaging. Magn Reson Med 2001;46(1):149-158.

36. Staten MA, Totty WG, Kohrt WM. Measurement of fat distribution by magnetic resonance imaging. Invest Radiol 1989;24(5):345-349.

37. Gerard EL, Snow RC, Kennedy DN, Frisch RE, Guimaraes AR, Barbieri RL, Sorensen AG, Egglin TK, Rosen BR. Overall body fat and regional fat distribution in young women: quantification with MR imaging. AJR Am J Roentgenol 1991;157(1):99-104.

38. Donnelly LF, O'Brien KJ, Dardzinski BJ, Poe SA, Bean JA, Holland SK, Daniels SR. Using a phantom to compare MR techniques for determining the ratio of intraabdominal to subcutaneous adipose tissue. AJR Am J Roentgenol 2003;180(4):993-998.

39. Markl M, Alley MT, Elkins CJ, Pelc NJ. Flow effects in balanced steady state free precession imaging. Magn Reson Med 2003;50(5):892-903.

40. Hargreaves BA, Vasanawala SS, Nayak KS, Hu BS, Nishimura DG. Fat-suppressed steady-state free precession imaging using phase detection. Magn Reson Med 2003;50(1):210-213.

41. Reeder SB, Pelc NJ, Alley MT, Gold GE. Rapid MR imaging of articular cartilage with steady-state free precession and multipoint fat-water separation. AJR Am J Roentgenol 2003;180(2):357-362.

42. Huang TY, Chung HW, Wang FN, Ko CW, Chen CY. Fat and water separation in balanced steady-state free precession using the Dixon method. Magn Reson Med 2004;51(2):243-247.

43. Glover GH. Multipoint Dixon technique for water and fat proton and susceptibility imaging. J Magn Reson Imaging 1991;1(5):521-530.

44. Skinner TE, Glover GH. An extended two-point Dixon algorithm for calculating separate water, fat, and B0 images. Magn Reson Med 1997;37(4):628-630.

45. Barnard ML, Schwieso JE, Thomas EL, Bell JD, Saeed N, Frost G, Bloom SR, Hajnal JV. Development of a rapid and efficient magnetic resonance imaging technique for analysis of body fat distribution. NMR Biomed 1996;9(4):156-164.

46. Thomas EL, Saeed N, Hajnal JV, Brynes A, Goldstone AP, Frost G, Bell JD. Magnetic resonance imaging of total body fat. J Appl Physiol 1998;85(5):1778-1785.

47. Sohlstrom A, Wahlund LO, Forsum E. Adipose tissue distribution as assessed by magnetic resonance imaging and total body fat by magnetic resonance imaging,

underwater weighing, and body-water dilution in healthy women. Am J Clin Nutr 1993;58(6):830-838.

48. De Kerviler E, Leroy-Willig A, Duboc D, Eymard B, Syrota A. MR quantification of muscle fatty replacement in McArdle's disease. Magn Reson Imaging 1996;14(10):1137-1141.

49. Schick F, Machann J, Brechtel K, Strempfer A, Klumpp B, Stein DT, Jacob S. MRI of muscular fat. Magn Reson Med 2002;47(4):720-727.

50. Iacobellis G, Leonetti F, Di Mario U. Images in cardiology: Massive epicardial adipose tissue indicating severe visceral obesity. Clin Cardiol 2003;26(5):237.

51. Kriegshauser JS, Julsrud PR, Lund JT. MR imaging of fat in and around the heart. AJR Am J Roentgenol 1990;155(2):271-274.

52. Lancaster JL, Ghiatas AA, Alyassin A, Kilcoyne RF, Bonora E, DeFronzo RA. Measurement of abdominal fat with T1-weighted MR images. J Magn Reson Imaging 1991;1(3):363-369.

53. Positano V, Gastaldelli A, Sironi AM, Santarelli MF, Lombardi M, Landini L. An accurate and robust method for unsupervised assessment of abdominal fat by MRI. J Magn Reson Imaging 2004;20(4):684-689.

54. Fuller MF, Fowler PA, McNeill G, Foster MA. Imaging techniques for the assessment of body composition. J Nutr 1994;124(8 Suppl):1546S-1550S.

55. Elbers JM, Haumann G, Asscheman H, Seidell JC, Gooren LJ. Reproducibility of fat area measurements in young, non-obese subjects by computerized analysis of magnetic resonance images. Int J Obes Relat Metab Disord 1997;21(12):1121-1129.

56. Zhu XP, Checkley DR, Hickey DS, Isherwood I. Accuracy of Area Measurements Made from Mr Images Compared with Computed-Tomography. J Comput Assist Tomo 1986;10(1):96-102.

57. Wood ML, Henkelman RM. Truncation artifacts in magnetic resonance imaging. Magn Reson Med 1985;2(6):517-526.

58. Hylton NM, Frankel SD. Imaging techniques for breast MR imaging. Magn Reson Imaging Clin N Am 1994;2(4):511-525.

59. Niitsu M, Tohno E, Itai Y. Fat suppression strategies in enhanced MR imaging of the breast: comparison of SPIR and water excitation sequences. J Magn Reson Imaging 2003;18(3):310-314.

60. de Kerviler E, Leroy-Willig A, Clement O, Frija J. Fat suppression techniques in MRI: an update. Biomed Pharmacother 1998;52(2):69-75.

61. Delfaut EM, Beltran J, Johnson G, Rousseau J, Marchandise X, Cotten A. Fat suppression in MR imaging: techniques and pitfalls. Radiographics 1999;19(2):373-382.

62. Zee CS, Segall HD, Terk MR, Destian S, Ahmadi J, Gober JR, Colletti PM. SPIR MRI in spinal diseases. J Comput Assist Tomogr 1992;16(3):356-360.

63. Hardy PA, Recht MP, Piraino DW. Fat suppressed MRI of articular cartilage with a spatial-spectral excitation pulse. J Magn Reson Imaging 1998;8(6):1279-1287.

64. Holsinger AE, Riederer SJ. The importance of phase-encoding order in ultra-short TR snapshot MR imaging. Magn Reson Med 1990;16(3):481-488.

65. Amano Y, Takahama K, Matsuda T, Amano M, Kumazaki T. Centrally fat-saturated three-dimensional magnetic resonance angiography of the abdomen using selective central fat-saturation of k-space. J Magn Reson Imaging 2003;18(5):567-574.

66. Fuderer M. The Information-Content of Mr Images. Ieee T Med Imaging 1988;7(4):368-380.

67. Yoshioka H, Alley M, Steines D, Stevens K, Rubesova E, Genovese M, Dillingham MF, Lang P. Imaging of the articular cartilage in osteoarthritis of the knee joint: 3D spatial-spectral spoiled gradient-echo vs. fat-suppressed 3D spoiled gradient-echo MR imaging. J Magn Reson Imaging 2003;18(1):66-71.

68. Roschmann P. Radiofrequency penetration and absorption in the human body: limitations to high-field whole-body nuclear magnetic resonance imaging. Med Phys 1987;14(6):922-931.

69. Prost JE, Wehrli FW, Drayer B, Froelich J, Hearshen D, Plewes D. SAR reduced pulse sequences. Magn Reson Imaging 1988;6(2):125-130.

70. Kuroda K, Oshio K, Mulkern RV, Jolesz FA. Optimization of chemical shift selective suppression of fat. Magn Reson Med 1998;40(4):505-510.

71. Chan TW, Listerud J, Kressel HY. Combined chemical-shift and phase-selective imaging for fat suppression: theory and initial clinical experience. Radiology 1991;181(1):41-47.

72. Mugler JP, 3rd, Epstein FH, Brookeman JR. Shaping the signal response during the approach to steady state in three-dimensional magnetization-prepared rapid gradient-echo imaging using variable flip angles. Magn Reson Med 1992;28(2):165-185.

73. Forster J, Schick F, Breuer J, Sieverding L, Lutz O. Slice-selective fat saturation in MR angiography using spatial-spectral selective prepulses. J Magn Reson Imaging 1998;8(3):583-589.

74. Zur Y. Design of improved spectral-spatial pulses for routine clinical use. Magn Reson Med 2000;43(3):410-420.

75. Thomasson D, Purdy D, Finn JP. Phase-modulated binomial RF pulses for fast spectrally-selective musculoskeletal imaging. Magn Reson Med 1996;35(4):563-568.

76. Yen YF, Han KF, Daniel BL, Heiss S, Birdwell RL, Herfkens RJ, Sawyer-Glover AM, Glover GH. Dynamic breast MRI with spiral trajectories: 3D versus 2D. J Magn Reson Imaging 2000;11(4):351-359.

77. Daniel BL, Yen YF, Glover GH, Ikeda DM, Birdwell RL, Sawyer-Glover AM, Black JW, Plevritis SK, Jeffrey SS, Herfkens RJ. Breast disease: dynamic spiral MR imaging. Radiology 1998;209(2):499-509.

78. Overall WR, Conolly SM, Nishimura DG, Hu BS. Oscillating dual-equilibrium steady-state angiography. Magn Reson Med 2002;47(3):513-522.

79. Hardy CJ, Dixon WT. Steady-state free precession imaging with inherent fat suppression. In: Proceedings of the 10th Annual Meeting of ISMRM, Honolulu; 2002:p 473.

80. Pruessmann KP, Weiger M, Scheidegger MB, Boesiger P. SENSE: sensitivity encoding for fast MRI. Magn Reson Med 1999;42(5):952-962.

81. Larkman DJ, deSouza NM, Bydder M, Hajnal JV. An investigation into the use of sensitivity-encoded techniques to increase temporal resolution in dynamic contrast-enhanced breast imaging. J Magn Reson Imaging 2001;14(3):329-335.

82. Friedman PD, Swaminathan SV, Smith R. SENSE imaging of the breast. AJR Am J Roentgenol 2005;184(2):448-451.

83. Vasanawala SS, Hargreaves BA, Pauly JM, Nishimura DG, Beaulieu CF, Gold GE. Rapid musculoskeletal MRI with phase-sensitive steady-state free precession: comparison with routine knee MRI. AJR Am J Roentgenol 2005;184(5):1450-1455.

84. Nayak KS, Hu BS, Hargreaves BA. Wideband SSFP: SSFP with imaging bandwidth greater than 1/TR. Proc Intl Soc Mag Reson Med 2005;13:2387.

85. Desmond K, Ramsay E, Plewes D. K-Space Ranking for Optimal Fat Suppression in Dynamic Breast MRI. Proc Intl Soc Mag Reson Med 2005;13:1850.

VITAE

Qi Peng was born in Huarong, Hunan Province, People's Republic of China, on December 14, 1975, the son of Hexiu Chen and Zhizheng Peng. After completing his work at the First High-school at Huarong, Hunan Province in 1993, he entered Tsinghua University, Beijing. He received the degree of Bachelor of Science with a major in Electrical Engineering in June 1998, and the degree of Master of Science with a major in Physics in June, 2000, both from Tsinghua University. In August, 2000, he entered the Biomedical Engineering Program, joint Program of the University of Texas Southwestern Medical Center at Dallas, and the University of Texas at Arlington. In 2000, he married Fan Zhang from Yueyang, Hunan. Their first son, Gregory William Peng was born in April 2005.

Permanent Address: YingShan ShiHua, TuiXiu Ban
                     Yueyang, Hunan Province, PR China, 414000